School of Chemical and Petroleum Engineering
Fuels and Energy Technology Institute

Significance of Surface-Generated Radicals in the Gas-Solid Catalytic Reactions

Syed Shatir Asghrar Syed Hassan

This thesis is presented for the Degree of
Doctor of Philosophy
of
Curtin University of Technology

December 2010

Declaration

To the best of my knowledge and belief this thesis contains no material previously published by any other person except where due acknowledgment has been made.

This thesis contains no material which has been accepted for the award of any other degree or diploma in any university.

Signature : **Syed Shatir Asghrar Syed Hassan**

Date : **13/05/2011**

Abstract

The conversion of light hydrocarbons with solid catalysts is an important class of reactions in the chemical and energy industries. Our knowledge on the exceedingly complex reaction kinetics of these catalytic reactions, especially the inter-influence between the reactions on catalyst and those in the gas phase, lags behind the requirement of technology development to improve efficiency and reduce emissions.

The purpose of this study was to investigate the significance of surface-generated radicals in influencing the kinetics and mechanisms of gas-solid catalytic reactions. The results indicate that desorption is an important fate of the surface-generated radicals. The presence/absence of significant mass transfer resistance for radicals, which is different from that for the mass transfer of molecular species, determines the successful desorption/diffusion of radicals into the bulk gas phase.

When a non-porous nickel mesh was used to catalyse the reactions between ethane and oxygen, it was found that the desorption/diffusion of radicals into the bulk gas phase could be facilitated by decreasing the mass transfer of radicals across the gas film around the nickel wires through increasing the gas flow rate traversing the mesh. The desorption of radicals increases the rate of chain reactions in the gas phase, resulting in the positive catalytic effects of nickel mesh. The nickel mesh can also have negative catalytic effects by quenching the gas-phase radicals by providing a surface to catalyse radical termination reactions.

Many Ni-catalysed hydrocarbon oxidation reactions involve the reduction and oxidation (redox) of nickel catalyst itself. Results of this study show that the migration/diffusion of radicals on the surface, from the surface into the NiO bulk and from the surface into the gas phase can all have significant effects on the reduction kinetics. These in turn depend on the size of NiO crystallite, the presence/absence of rigid pore structure and the type of radicals formed on the catalyst surface.

The use of fluidised nanoparticles as catalysts can lead to drastic reduction of reactor size for improved efficiency and reduced capital/operating costs. The catalytic oxidation of ethane with oxygen inside a fluidised bed of unsupported NiO nanoparticles in this study shows very different behaviour from the same reaction catalysed with silica-supported NiO catalysts. These differences can be explained by considering the difference in the resistance for the desorption of radicals into the bulk gas phase between the two catalytic systems.

Overall, this study highlights the importance of considering the fates of surface-generated radicals in elucidating the kinetics and mechanism of gas-solid catalytic reactions. The original findings of this study are valuable for the development of innovative heterogeneous catalytic processes, especially the partial oxidation of light hydrocarbons, with high efficiency, low emission and low capital/operating costs.

Acknowledgement

This thesis would not have been accomplished without the kind support and assistance of many individuals, departments and organisations. I am particularly grateful to the excellent supervision and support I received from Professor Chun-Zhu Li during the course of my PhD study. I really appreciate the help given by Professor Hongwei Wu especially in ensuring my smooth transfer from Monash University to Curtin University of Technology. I am immensely indebted to Dr Woo Jin Lee for the advice, help and discussions during the first year of my study. To all postdoctoral research fellows and postgraduate cohorts (Curtin and Monash), whom I spent most of my time with for the past several years, I would like to thank all of you very much for your friendship, cooperation and assistance.

My appreciation should also go to all the staffs of Fuels and Energy Technology Institute and Chemical Engineering Department of Monash University for the numerous helps and supports. I am very thankful to my scholarship provider, the Malaysian Ministry of Higher Education (MOHE) and the Universiti Teknologi MARA (UiTM) as well as to my top-up scholarship provider, the Western Australian Energy Research Alliance (WA:ERA). The financial support for the research project by (1) the Australian Research Council (ARC) and (2) the Western Australian State Government via the Centre for Research into Energy for Sustainable Transport (CREST) are also greatly appreciated. Last but not least, many thanks to my family, relatives and friends for the continuous understanding, encouragement and prayers.

No one who achieves success does so without the help of others.
The wise and confident acknowledge this help with gratitude.
~ Alfred North Whitehead (1861 – 1947)

Table of contents

List of tables

List of figures

Chapter 1

Chapter 2

Chapter 3

Chapter 4

Chapter 5

Chapter 6

Significance of surface-generated radicals in the gas-solid catalytic reactions

Syed Shatir Asghrar Syed Hassan

Fuels and Energy Technology Institute
Curtin University of Technology

A thesis presented for the Degree of
Doctor of Philosophy
of
Curtin University of Technology

CHAPTER 1

Introduction

1.1 Background and research impetus

Heterogeneous catalysis has played and continues to play pivotal roles in the world's industrial development. The use of heterogeneous catalysts is crucial in the mass production of fuels and chemicals as well as in the environmental protection measures such as in the cleanup of industrial and power plant off-gases.

Traditional catalysts employed in the gas-solid catalytic reactions are in the form of supported catalysts, in which catalytically active species are loaded inside porous particles. The overall process by which catalytic reactions proceed inside a porous supported catalyst, as is depicted in Fig. 1.1, follows seven sequential steps as follows [1]:

1. mass transfer of the reactant(s) across a film resistance from the bulk gas phase towards the catalyst pores,
2. internal diffusion of the reactant(s) inside the catalyst pores from the pore mouth to the vicinity of catalyst surface,
3. adsorption of the reactant(s) onto the catalyst surface,
4. chemical reaction on the catalyst surface,
5. desorption of the product(s) from the catalyst surface,
6. diffusion of the product(s) towards the pore mouth of the catalyst particle, and
7. mass transfer of the product(s) across a film resistance away from the catalyst and into the bulk gas phase.

Step 3 of the catalytic reaction process, i.e. the adsorption of reactant(s) on the catalyst surface, would normally result in the formation of reactive species called radicals. Radicals are chemical species which have one or more unpaired electrons. They are often formed as intermediates in many important chemical processes ranging from atmospheric chemistry to hydrocarbon combustion and polymerisation. The formation of radicals on a solid surface is a phenomenon important not only in the area of heterogeneous catalysis but also in other science and engineering fields such as metallurgical reduction, corrosion science, photochemistry and micro- and

opto-electronics. Among the main mechanisms leading to the formation of surface-adsorbed radicals are [2]:

i. surface-induced homolytic splitting

$AB = A^{\bullet}(s) + B^{\bullet}(s)$

and

ii. atom transfer

$A–H + O^{-}(s) = A^{\bullet}(s) + OH^{-}(s)$

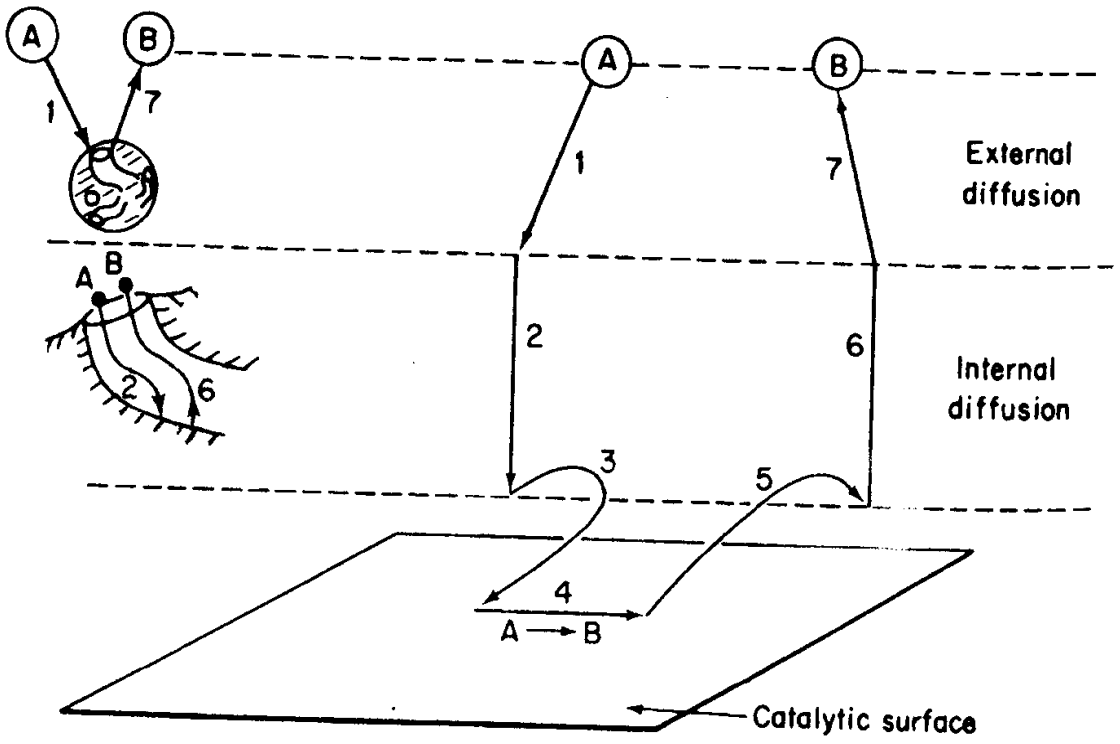

Fig. 1.1 Steps in a heterogeneous catalytic reaction (Fogler, H., Elements of Chemical Reaction Engineering, 4th Ed., © 2006. Reprinted by permission of Pearson Education, Inc., Upper Saddle River, NJ).

Generally, it is perceived that the surface-formed radicals will remain on the surface to further undergo surface reactions (i.e. step 4) to form final products before desorption (i.e. step 5). However, substantial amount of studies have suggested that the surface radicals are mobile [3] and their fates can also include the desorption from the surface [4-24].

The theory of radical desorption, as can be traced, was first proposed about a century ago by Irving Langmuir, the 1932 Noble Prize winner in chemistry. In his paper [4] on the hydrogen removal from a tungsten wire of a lamp bulb, Langmuir explained that within the range of his experimental conditions, hydrogen would dissociate into hydrogen atoms on the tungsten wire. Parts of those hydrogen atoms diffused out of the tungsten metal in the form of atoms and remained as atoms even after leaving the metal surface. Some of the desorbed hydrogen atoms (radicals), according to Langmuir, recombined to form hydrogen molecules in the gas phase and some of them adsorbed onto the glass surface to form unstable compounds by reactions with some of the glass constituents or combined on the surface with another hydrogen atom to form ordinary molecular hydrogen [4].

In the field of heterogeneous catalysis, Daniel and Keulks [5], Hart and Friedli [6] and Dolejsek and Novakova [7] have suggested the surface-initiated gas-phase reaction mechanisms in the catalytic oxidation of propylene. Their studies indicated that the surface-generated allyl radicals desorbed from the catalyst surface to initiate homogeneous reactions in the gas phase. In the study on the formic acid decomposition at 145 – 457 °C, Tevault et al. [8] suggested that the OCOH radicals which were generated by H-atom abstraction on the Pt surface desorbed to take part in the homogeneous gas-phase reactions. Talley et al. [9] studied the reaction between H_2 and O_2 on the Pt surface. They found that OH radicals did escape from the surface of the Pt metal during this reaction. Dulcey and Lin [10], on the other hand, observed the desorption of phosphorous monoxide (PO) radicals in their study on the catalytic decomposition of dimethyl methyl phosphate (DMMP) and trimethyl phosphate (TMP) on the polycrystalline Pt surfaces. The desorption of alkyl and alkenyl radicals in the catalytic decomposition of hexane over tungsten (827 – 1527 °C) and platinum (577 – 1127 °C) were studied by Amorebleta and Colussi [11]. The

authors suggested that the free radicals, once formed on the surface, could either desorb from the surface or decompose on the metal surface to form smaller hydrocarbon fragments including the olefin products.

Substantial studies on the desorption of surface-generated radicals, (for example, see Refs [12-18]), were carried out in Texas A&M University by Professor Lunsford and his students/co-workers. In one of the studies, Driscoll and Lunsford [13] investigated the reactions of methane, ethane, ethylene and propylene over various metal oxide catalysts. The results of this study led to the conclusions that the ability of a surface to supply gas-phase hydrocarbon radicals depends on (i) the bond strength of the weakest C-H bond, (ii) the presence of particular radical-forming sites on the surface and (iii) the propensity of the radicals to either desorb or to undergo subsequent reactions on the surface. In another study by the same group [14-16], it was proposed that the gas-phase methyl radicals produced from CH_4 on the catalyst surface coupled in the gas-phase to form C_2H_6. This proposal was in contrast to the original mechanism of oxidative coupling of methane proposed by Keller and Bhasin [25] where the formation of C_2H_6 was believed to be the result of the combination of adsorbed CH_3 radicals on the catalyst surface.

Despite the vast amount of studies proposing the desorption of radicals, a heterogeneous catalytic reaction remains to be popularly seen as a purely surface reaction. This is not very surprising, considering that the majority of studies on catalytic reactions were carried out using porous supported catalysts. With porous catalysts, the mass transport limitations for the molecular species (reactants and products) can easily be minimised by carefully determining the critical size of catalyst particles, the flow rate, the temperature and the pressure. However, the same principle to eliminate mass transfer resistance does not apply to the radical species. This is because radicals are very reactive and their lifetimes are extremely short. The pellet size required for the internal concentration gradients to be negligible is far smaller than the minimum pellet size requirement imposed by the pressure drop consideration for a fixed-bed reactor operation [26, 27]. This means, with the use of a traditional porous catalyst, the mass transfer limitations for the radicals are “irreducible” and, hence, the desorbed radicals would not have a chance to escape

into the bulk gas phase. Instead, they would be easily consumed inside the catalyst pores (in the "gas phase" or on the surface), giving the perception that the reaction products are generated exclusively on the catalyst surface.

Recently, a renewed interest on the understanding of the fates of surface-generated radicals was sparked by the works carried out by this research group (where the present work was carried out), led by Professor Li (initially in Monash University) [19-24]. In view of the existence of "irreducible" mass transfer limitation for the radicals with the use of conventional porous catalyst fixed-bed systems, Quah and Li [22] explored a new approach by using the non-porous nickel and Monel meshes as catalyst to eliminate the effects of internal mass transfer in the catalytic oxidation of methane with air. In other words, they simplified the catalytic reaction steps from seven to five by eliminating steps 2 and 6 of the catalytic reaction process (see Fig. 1.1).

Two reactor systems were employed in their first study [22]. The first reactor was a novel wire-mesh reactor and the second one was a quartz tubular reactor. In the wire-mesh reactor, except for the mesh itself, temperature at all other parts of the reactor remained close to the room temperature to allow the understanding of surface reactions without the complications of the thermally-induced gas-phase reactions. In the quartz tube reactor which was heated inside a furnace, the overall reactions were contributed by both the heterogeneous and the homogeneous reactions. Comparison of the results from the two reactors allowed them to understand the inter-influence between the reactions on the catalyst surface and those in the gas phase. They concluded that the gas-phase coupling of the desorbed CH_3 radicals was an important route for the observed C_2H_6 formation and that the homogeneous reactions between CH_4 and O_2 in the gas phase could somehow inhibit the reactions on the catalyst surface.

Without the complications of internal porous structure with the use of mesh catalyst, Quah and Li [19-21] and Lee and Li [23, 24] found that that the free radicals formed on the catalyst surface could desorb into the gas phase when the thickness of gas film around the nickel wires was reduced by increasing the gas flow rate passing

through the mesh. Their studies demonstrated that the surface-generated radicals which desorbed from the mesh surface could initiate/enhance the homogeneous chain radical reactions in the gas phase and increase the rate of overall reactions.

The desorption of radicals has also been found to greatly limit the successive dehydrogenation of C_xH_y species on the catalyst surface and thus eliminated the formation of coke on the surface of nickel mesh during the catalytic pyrolysis of light alkane (methane, ethane and LPG) [19, 21, 23]. Without severe coke formation, Ni mesh activity remained unchanged even after long periods of reaction time under the conditions where the supported Ni-based catalysts would have easily been completely deactivated by the coke build-up.

In a more recent study, Lee and Li [24] found that the desorption of radicals from the catalyst surface could even be manipulated to control/enhance the catalytic growth of carbon nanomaterials. In studying the pyrolysis of ethane and acetylene at 750 °C, Lee and Li [24] observed the opposite effects of gas flow rate on the amount, type and structure of carbon formed on the nickel mesh surface. The results of their study were explained by considering the relative ease (based on the bonding strength with Ni) with which C-containing radicals and H radicals desorb from Ni surface with increasing gas flow rate. Lee and Li [24] believed that, while the preferential desorption of C_2H_5 radicals in ethane pyrolysis would create an H-rich surface to discourage the formation of carbon, the preferential desorption of H radicals in acetylene pyrolysis, on the contrary, would create an H-deficient surface that would promote the formation of carbon.

From the above review, it is apparent that the understanding of the fates and roles of surface-generated radicals in the gas-solid catalytic reactions, particularly of light hydrocarbons, is significantly important, especially in view of the increasing interest shown worldwide towards the valorisation of light alkanes [28, 29] to manufacture more valuable products via an environmentally sound and an efficient technology. Poor understanding of the reaction kinetics and mechanisms due to the failure to deeply understand the actual process taking place with the radicals upon their formation on the catalyst surface may partly be the reasons why many proposed

processes relating to the catalytic conversion of natural gas and light alkanes still remain uncommercialised.

The use of the traditional porous supported catalysts in the fundamental catalysis study clearly has some limitations. In addition to the existence of "irreducible" mass transfer resistance for radicals inside the pores which have been explained above, the catalyst particles formed on the porous support can be of variable sizes. The different size of catalyst particles would present different effects on the radical activities and their fates on the surface, thus, contributing further complications to the kinetics and mechanism studies.

Although the work by Li et al. [19-24] has shed some light on our understanding of the influence of surface-generated radicals during the catalytic reactions, the current knowledge based on their studies is still very limited. Firstly, the past studies by Quah and Li and [19-22] and Lee and Li [23, 24] with nickel mesh catalyst were mainly focused on the pyrolysis of alkanes and the partial oxidation of methane with air. The catalytic reaction of ethane in the presence of significant amount of oxygen which is expected to produce more types of radicals and is more complicated has never been studied using these simple catalytic systems that can give unequivocal results on reaction mechanism. Secondly, the catalytic reactions on the surface of a nickel mesh catalyst are still far away from representing the actual situations inside the traditional porous catalysts. This is because the proportion of atoms on the nickel mesh surface is far too low to compare with the proportion of atoms on the surface of fine particles (normally in nano-size) loaded inside the traditional porous catalysts. Finally, there is still a lack of understanding on the influence of surface-generated radicals in the redox-type catalytic reactions, in which, parts of the catalyst (lattice oxygen) are continuously consumed and re-generated during the reactions [30].

Considering the limitations of the present understanding, the work presented in this thesis (see details below) was inspired and aimed to extend the existing fundamental knowledge on the fates and roles of surface-generated radicals in the catalytic reactions, especially in the hydrocarbon partial oxidation system (a process by which a mixture of vapourised hydrocarbon and an oxygen-containing gas are

reacted over catalyst) that is of highly importance from the industrial perspective. Catalytic partial oxidation (CPO) of light alkanes (using oxygen as oxidant) has previously been reported to yield important products such as olefin (e.g. ethylene) [31], syngas [32], acetic acid [33] and other oxygenates [34]. The considerable ambiguity and confusion as to the main reaction mechanism taking place, especially on the roles of heterogeneous and homogeneous chemistry involving numerous radicals, have largely suppressed the progress in the development of commercially viable CPO processes.

1.2 Thesis organisation

The ultimate purpose of the present study was to gain a comprehensive understanding on the roles of radicals species formed as intermediates on the catalyst surface in influencing the overall kinetics and mechanisms of catalytic reactions, with particular attention given to the attractive process of light hydrocarbon partial oxidation [28, 29] with nickel-based catalyst (one of the most commonly used group of catalyst in industry).

This thesis is divided into seven chapters. The current chapter **(*Chapter 1*)** provides an overview on the importance of surface-generated radicals in the catalytic reaction processes and explains the motivation and the aims of the research work presented in this thesis.

Chapter 2 **(Experimental design and approach)** gives a description of the reactor systems used in this study and introduces the analytical instruments employed. Details on experimental procedures of every individual studies, however, will only be given in the specific chapter related to a particular study ***(Chapter 3 to 6)***.

Chapter 3 to 6 are the main body of this thesis which will detail the efforts made and the significant findings obtained in this doctoral project. At the beginning of

these chapters, a short overview is provided to guide the reader on the aim and the main findings of the study.

As an extension to the past studies by this research group [19-24], the first part of this study **(*Chapter 3*)** deals with the study on the catalytic partial oxidation of ethane with nickel mesh catalyst which is more complicated than the pyrolysis reactions (the major focus of previous studies [19-24]). ***Chapter 3*** presents the experimental procedures, the results and discussions of the study on the catalytic partial oxidation of ethane in a tubular reactor with Ni mesh catalyst at 625 °C and atmospheric pressure. The dual roles of catalyst surface in promoting and inhibiting reactions in the gas phase by supplying (via radical desorption) and quenching the radicals is discussed.

The catalytic partial oxidation of light alkanes over Ni-based catalysts has been proposed to take place via a series of oxidation/reduction of Ni/NiO [35-38]. During reduction, where radicals are formed as a result of molecular activation on the catalyst surface, the fates and activities of surface-generated radicals could be important factors influencing the overall kinetics and mechanism. Realising this fact, the work in this thesis **(*Chapter 4* and *Chapter 5*)** was partially dedicated on studying the reduction of nickel oxide. Understanding the reduction of nickel oxide will form part of the understanding of the redox catalytic reaction mechanism, and hence, is an important element of this thesis.

As the size of catalyst may have significant effects on the activities of surface-generated radicals, ***Chapter 4*** of this thesis is devoted to the study of the effects of NiO crystallite size on radical activities and its influences on the kinetics and mechanism of NiO reduction with H_2. The focus of ***Chapter 4*** is on the reduction with H_2, a simple system to provide a good basis for the understanding of the reduction mechanism. Extending the work presented in ***Chapter 4***, the study on the fates and activities of different surface radicals (formed from different gaseous reductants) in the reduction of nickel oxide and the significance of the presence/absence of mass transfer resistance of radicals are discussed in **Chapter 5**.

Since it is important that the fundamental catalytic reaction study has to represent as closely as possible to the real situations inside the actual catalytic system, a new reactor concept based on the knowledge gained from the findings of Li et al. with the non-porous nickel mesh catalyst [19-24] was developed and tested. In this study, the use of fluidised bed nanoparticle reactor (details will be discussed in ***Chapter 2 and 6***), which not only features the elimination of the internal mass transfer complications, but also represents similar scale (in term of the size of catalyst particle and thus the surface atom proportion) to the porous supported catalyst system, was explored. **Chapter 6** will discuss in great details the use of fluidised nanoparticle NiO catalyst for the catalytic oxidative conversion of ethane and its comparison with the traditional silica-supported NiO catalyst.

Finally, **Chapter 7** will draw the conclusions arising from this doctoral study and provides a future outlook and recommendations for further work in the current field of study.

1.3 References

[1] H.S. Fogler, Elements of Chemical Reaction Engineering, 4th ed., Prentice Hall PTR, Upper Saddle River, NJ, 2006.

[2] M. Chiesa, E. Giamello, M. Che, EPR characterization and reactivity of surface-localized inorganic radicals and radical ions, Chem. Rev. 110 (2009) 1320-1347.

[3] B. Jackson, H. Metiu, The dynamics of H_2 dissociation on Ni(100): A quantum mechanical study of a restricted two-dimensional model, J. Chem. Phys. 86 (1987) 1026-1035.

[4] I. Langmuir, A chemically active modification of hydrogen, J. Am. Chem. Soc. 34 (1912) 1310-1325.

[5] C. Daniel, G.W. Keulks, The catalytic oxidation of propylene : I. Evidence for surface initiated homogeneous reactions, J. Catal. 24 (1972) 529-535.

[6] P.J. Hart, H.R. Friedli, Desorption of allyl radicals in the heterogeneously-catalysed oxidation of propene: mass spectrometric study, J. Chem. Soc. D (1970) 621-622.

[7] Z. Dolejsek, J. Nováková, Mass spectrometric observation of allyl radicals during the interaction of propene with some oxides at low pressures, J. Catal. 37 (1975) 540-543.

[8] D.E. Tevault, M.C. Lin, M.E. Umstead, R.R. Smardzewski, Evidence for production of the hydroxycarbonyl radical in the decomposition of formic acid on platinum, Int. J. Chem. Kinet. 11 (1979) 445-449.

[9] L.D. Talley, D.E. Tevault, M.C. Lin, Laser diagnostic of matrix-isolated OH radicals from oxidation of H_2 on platinum, Chem. Phys. Lett. 66 (1979) 584-586.

[10] C.S. Dulcey, M.C. Lin, C.C. Hsu, Thermal desorption of the PO radical from polycrystalline Pt surfaces, Chem. Phys. Lett. 115 (1985) 481-485.

[11] V.T. Amorebieta, A.J. Colussi, Gas-phase free radicals in the catalytic decomposition of hexane over tungsten. A modulated-beam mass spectrometric study, J. Phys. Chem. 86 (1982) 2760-2765.

[12] K.D. Campbell, J.H. Lunsford, Contribution of gas-phase radical coupling in the catalytic-oxidation of methane, J. Phys. Chem. 92 (1988) 5792-5796.

[13] D.J. Driscoll, J.H. Lunsford, Gas-phase radical formation during the reactions of methane, ethane, ethylene, and propylene over selected oxide catalysts, J. Phys. Chem. 89 (1985) 4415-4418.

[14] D.J. Driscoll, W. Martir, J.X. Wang, J.H. Lunsford, Formation of gas-phase methyl radicals over magnesium oxide, J. Am. Chem. Soc. 107 (1985) 58-63.

[15] T. Ito, J.H. Lunsford, Synthesis of ethylene and ethane by partial oxidation of methane over lithium-doped magnesium oxide, Nature 314 (1985) 721-722.

[16] T. Ito, J. Wang, C.H. Lin, J.H. Lunsford, Oxidative dimerization of methane over a lithium-promoted magnesium oxide catalyst, J. Am. Chem. Soc. 107 (1985) 5062-5068.

[17] J.H. Lunsford, The role of surface-generated gas-phase radicals in catalysis, Langmuir 5 (1989) 12-16.

[18] E. Morales, J.H. Lunsford, Oxidative dehydrogenation of ethane over a lithium-promoted magnesium-oxide catalyst, J. Catal. 118 (1989) 255-265.

[19] E.B.H. Quah, C.-Z. Li, Effects of radical desorption on catalyst activity and coke formation during the catalytic pyrolysis and oxidation of light alkanes, Appl. Catal. A 250 (2003) 83-94.

[20] E.B.H. Quah, C.-Z. Li, Roles of desorbed radicals and reaction products during the oxidation of methane using a nickel mesh catalyst, Appl. Catal. A 258 (2004) 63-71.

[21] E.B.H. Quah, C.-Z. Li, Pyrolysis of liquefied petroleum gas assisted by radicals desorbed from mesh catalyst surface, Int. J. Chem. Kinet. 35 (2003) 637-646.

[22] E.B.H. Quah, J.F. Mathews, C.-Z. Li, Interinfluence between reactions on the catalyst surface and reactions in the gas phase during the catalytic oxidation of methane with air, J. Catal. 197 (2001) 315-323.

[23] W.J. Lee, C.-Z. Li, Coke formation and reaction pathways of catalyst-surface-generated radicals during the pyrolysis of ethane using Ni mesh catalyst, Appl. Catal. A 316 (2007) 90-99.

[24] W.J. Lee, C.-Z. Li, Opposite effects of gas flow rate on the rate of formation of carbon during the pyrolysis of ethane and acetylene on a nickel mesh catalyst, Carbon 46 (2008) 1208-1217.

[25] G.E. Keller, M.M. Bhasin, Synthesis of ethylene via oxidative coupling of methane : I. Determination of active catalysts, J. Catal. 73 (1982) 9-19.

[26] P.M. Couwenberg, Q. Chen, G.B. Marin, Irreducible mass-transport limitations during a heterogeneously catalyzed gas-phase chain reaction: oxidative coupling of methane, Ind. Eng. Chem. Res. 35 (1996) 415-421.

[27] P.M.P. Couwenberg, Q. Chen, G.B. Marin, Kinetics of a gas-phase chain reaction catalyzed by a solid: the oxidative coupling of methane over Li/MgO-based catalysts, Ind. Eng. Chem. Res. 35 (1996) 3999-4011.

[28] E.G. Derouane, J. Haber, F. Lemos, F.R. Ribiero, M. Guisnet, (Eds.). Catalytic Activation and Functionalisation of Light Alkanes: Advances and Challenges. Kluwer Academic Publishers, Dordrecht, The Netherlands, 1997.

[29] J.A. Labinger, J.E. Bercaw, Understanding and exploiting C-H bond activation, Nature 417 (2002) 507-514.

[30] C. Doornkamp, V. Ponec, The universal character of the Mars and Van Krevelen mechanism, J. Mol. Catal. A: Chem. 162 (2000) 19-32.

[31] E.M. Thorsteinson, T.P. Wilson, F.G. Young, P.H. Kasai, The oxidative dehydrogenation of ethane over catalysts containing mixed oxides of molybdenum and vanadium, J. Catal. 52 (1978) 116-132.

[32] A. Beretta, P. Forzatti, Partial oxidation of light paraffins to synthesis gas in short contact-time reactors, Chem. Eng. J. 99 (2004) 219-226.

[33] D. Linke, D. Wolf, M. Baerns, S. Zeyβ, U. Dingerdissen, L. Mleczko, Catalytic partial oxidation of ethane to acetic acid over $Mo_1V_{0.25}Nb_{0.12}Pd_{0.0005}O_x$: reactor operation, Chem. Eng. Sci. 57 (2002) 39-51.

[34] Y. Wang, K. Otsuka, H. Wan, Partial oxidation of methane and ethane to oxygenates over silica supported rhenium oxide, React. Kinet. Catal. Lett. 79 (2003) 127-133.

[35] Y.H. Hu, E. Ruckenstein, Catalyst temperature oscillations during partial oxidation of methane, Ind. Eng. Chem. Res. 37 (1998) 2333-2335.

[36] E. Heracleous, A.A. Lemonidou, Ni-Nb-O mixed oxides as highly active and selective catalysts for ethene production via ethane oxidative dehydrogenation. Part II: Mechanistic aspects and kinetic modeling, J. Catal. 237 (2006) 175-189.

[37] X.-B. Ren, X.-Y. Guo, Monte Carlo simulation of the oscillatory behavior in partial oxidation of methane on nickel catalyst under nonisothermal conditions, Surf. Sci. 603 (2009) 606-610.

[38] X. Lin, C.A. Hoel, W.M.H. Sachtler, K.R. Poeppelmeier, E. Weitz, Oxidative dehydrogenation (ODH) of ethane with O_2 as oxidant on selected transition metal-loaded zeolites, J. Catal. 265 (2009) 54-62.

CHAPTER 2

Experimental design and approach

2.1 Introduction

This chapter will briefly describe the design and features of the reactor systems used in this study for the investigation of the catalytic oxidative reaction of ethane as well as the thermogravimetric apparatus used in the kinetic study of nickel oxide reduction. In addition, it will also outline the analytical instruments and techniques used in the gas analysis and catalyst characterisation.

2.2 Ultra-short contact time tubular reactor with Ni mesh catalyst

The experiments on the catalytic partial oxidation of ethane at 625 °C, which will be discussed in more details in Chapter 3, were carried out in a quartz tubular reactor identical to those previously used by Lee and Li for the pyrolysis of ethane and acetylene [1, 2]. The reactor was made of quartz and had an internal diameter of 2.0 cm and a length of 80 cm. It was placed and heated inside a 60 cm long single-heated-zone electrical furnace. The reactor was positioned so that 10 cm of its top and bottom were outside of the furnace (see Figs. 2.1 and 2.2).

This reactor could be operated both as a non-catalytic and a catalytic reactor. When it was used as a catalytic reactor, a nickel mesh (36% open area and 0.38 mm width opening) was used as a catalyst. The mesh which was weaved (40 x 40) using pure nickel wires of 0.25 mm diameter was obtained from Unique Wire Weaving Co. Inc. A fresh round piece of nickel mesh with a diameter just slightly larger than 2.0 cm was used as the catalyst for each experiment described in Chapter 3. It was first washed with a mixture of methanol and chloroform to remove greases and impurities before being used.

The use of nickel mesh as a catalyst simplified the catalytic reaction steps by eliminating the internal diffusion steps, thus, allowing the catalytic reaction study to be performed without the complications of the internal mass transfer limitations that usually encountered with the use of porous catalysts.

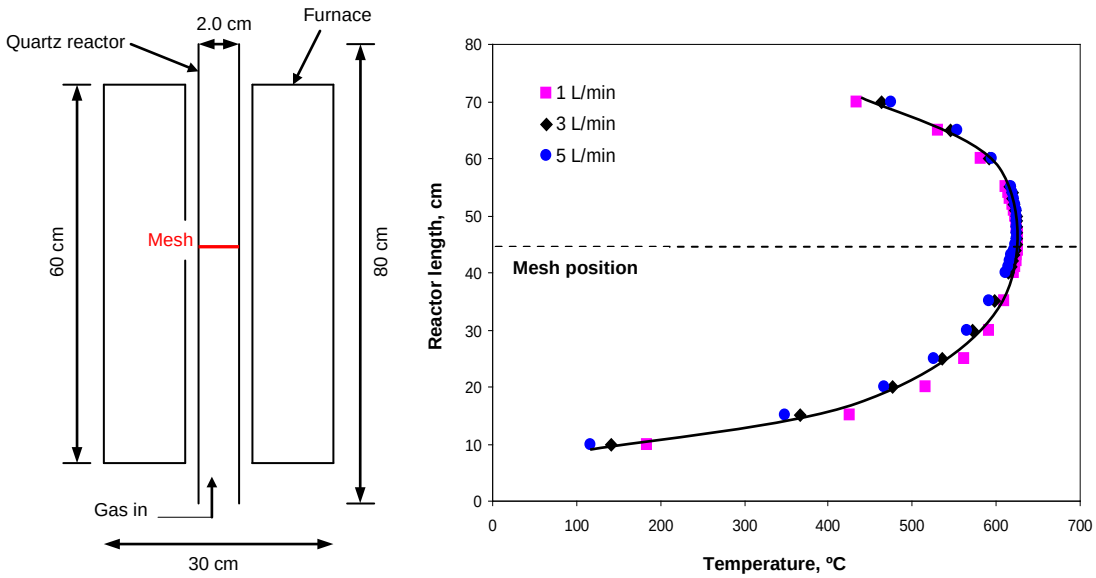

Fig. 2.1 Tubular reactor and its temperature distribution.

Fig. 2.2 A photograph of the experimental set-up for the tubular reactor system.

During the catalytic reaction studies, the mesh catalyst was placed inside the quartz tube, slightly above the middle of the reactor, which is the onset of isothermal zone as is shown in Fig. 2.1. The thermal expansion of the mesh during heating, being larger than that of quartz, ensured that the mesh catalyst remained at its intended position at all times during the course of the experiment. Fig. 2.1 shows the axial temperature profile of the reactor and indicates the position of mesh catalyst during experiments.

2.3 Fluidised-bed nanoparticle reactor

Nanoparticles possess the characteristics of an ideal catalyst. They have relatively a large surface-area-to-volume ratio, a high percentages of surface atoms and a simple, if at all, pore structure. However, nanoparticles tend to form tightly packed agglomerates inside a fixed-bed reactor due to the dominance of strong inter-particle forces. The agglomerates introduce a mass transfer resistance similar in magnitude to the porous catalyst. This problem can only be overcome by bringing the gas and nanoparticles into contact in a fluidised bed.

The traditional understanding of fluidised bed based on the Geldart's classification [3] of the particles ranging in size from a few milimeters down to a few tens of microns suggest that nanoparticles are hardly fluidisable (Fig. 2.3). However, recent researches [4-7] have showed that unlike the conventional Geldart's group C particles, nanoparticles are fluidisable in a most unexpected way. Nanoparticles were reported to form very loose agglomerates that continuously break and reform during fluidisation [7].

The dynamic behaviour of the fluidised nanoparticle agglomerates means that, inside a fluidised-bed reactor, virtually all of the massive surface area of the nanoparticles may be available for contact with gas and hence for reaction. This has been demonstrated indirectly in the coating experiments of the Professor Weimer's

research group [8, 9], where the primary nanoparticles, instead of their aggregates, were found to be individually coated.

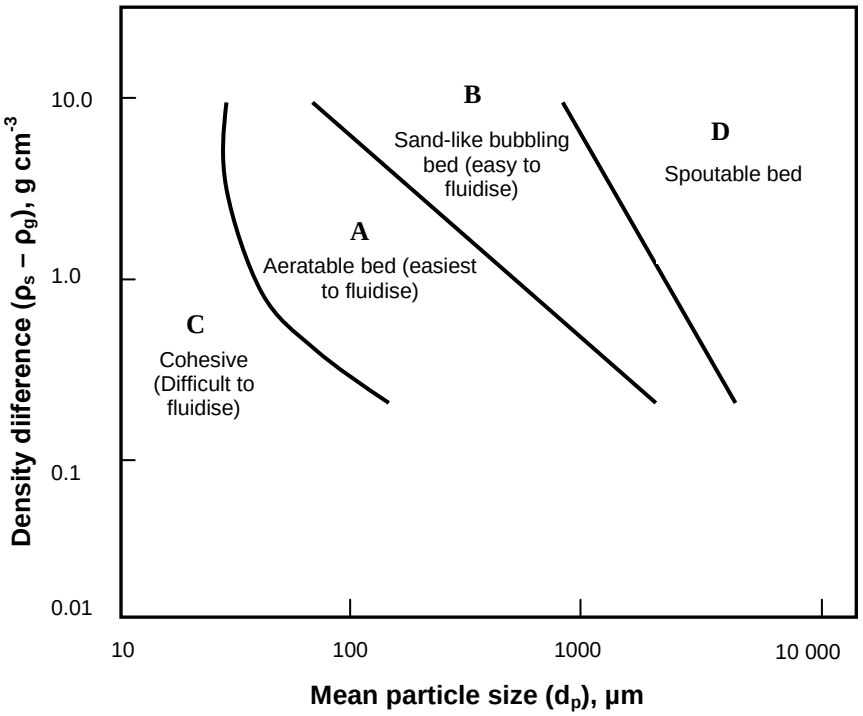

Fig. 2.3 Geldart's classification of the fluidising particles (adapted from [3]).

A fluidised-bed nanoparticle reactor offers the potential to greatly reduce the problems associated with the "irreducible" mass transfer limitations for radicals encountered with the use of traditional porous supported catalysts. In this study, the fluidised-bed reactor which was made of quartz glass was used to study the catalytic oxidative reaction of ethane using fluidised unsupported NiO nanoparticles as the catalyst. Direct comparison with the traditional porous catalytic system was also made. For this purpose, silica-supported NiO was used as a catalyst to catalyse the same reaction inside the same reactor. This will be discussed in details in Chapter 6.

A schematic representation of the reactor used in this study is presented in Fig. 2.4. As can be seen, the reactor consisted of two sections. The bottom section of the reactor had an i.d. and a length of 37 mm and 110 mm respectively. The expanded section at the top for catalyst disengagement was 70 mm i.d. and 110 mm long. The top and the bottom parts were connected together through a contracted zone of 30 mm high, making the reactor's length to be 250 mm in total. Quartz frits of 4 mm thickness were attached at the bottom and the top of reactor. The bottom frit functioned as a gas distributor while the top frit worked as a filter to prevent the significant elutriation of nanoparticles.

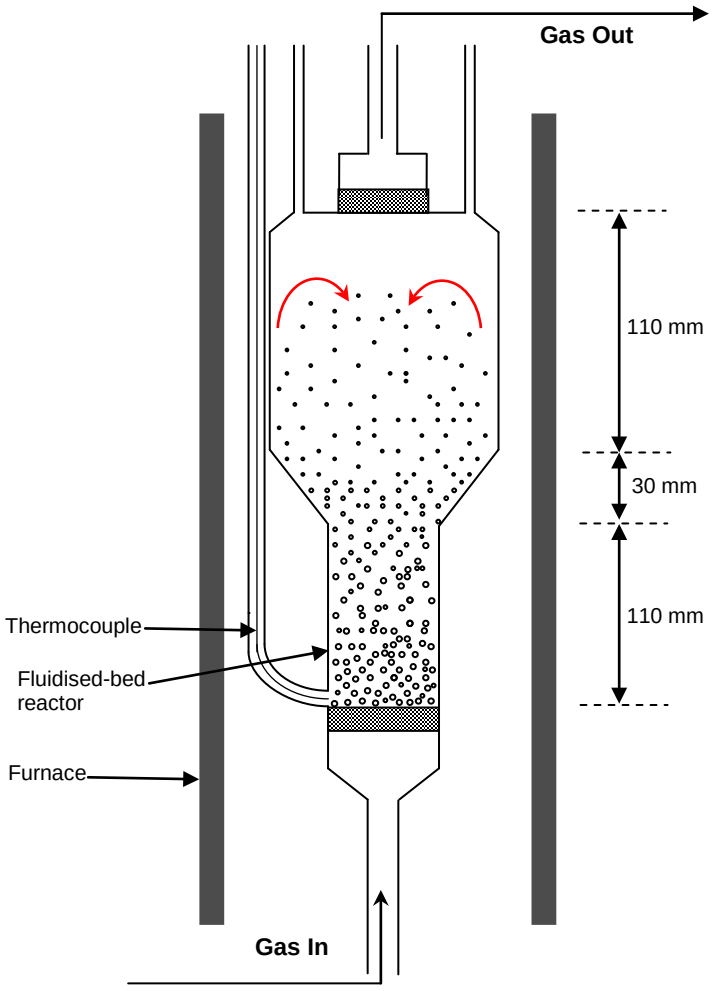

Fig. 2.4 A schematic representation of the fluidised-bed nanoparticle reactor.

During the experiments, the reactor was placed and heated inside a 54 cm long vertical split tube furnace (Fig. 2.5). A K-type thermocouple was inserted into the bed to monitor the reaction temperature. By moving the thermocouple to various locations within the catalyst bed, we confirmed the absence of hot spots in this system. In an actual experiment, the thermocouple was inserted through the side tube and the tip of thermocouple was positioned at about 0.5 cm above the distributor frit (see Fig. 2.4).

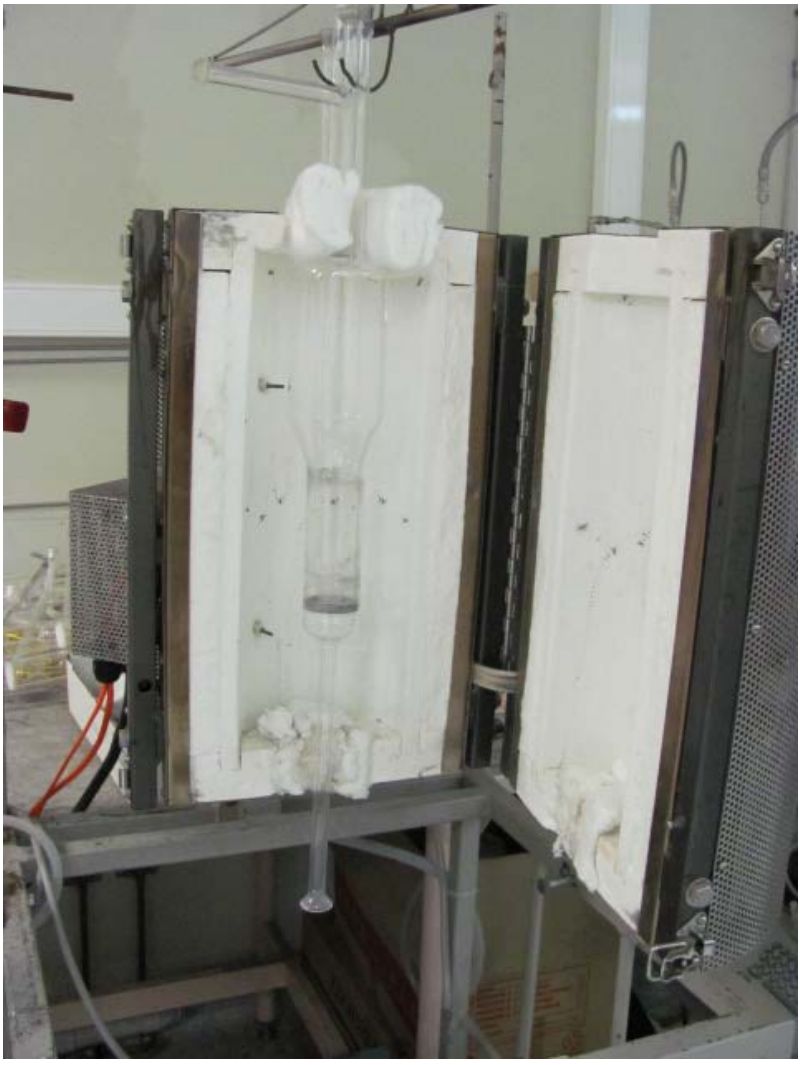

Fig. 2.5 A photograph of the quartz fluidised-bed reactor and the split tube furnace.

2.4 Thermogravimetric analysis

Measurements of changes in NiO sample mass with time were made in order to study the kinetics of NiO reduction. For this purpose, a thermogravimetric analysis (TGA) unit (TA SDT-Q600) with 0.1 µg weighing sensitivity was used (Fig. 2.46). The TGA unit consisted of a horizontal furnace which was encased inside a perforated stainless steel cowling. A cross-section of the TGA furnace is shown in Fig 2.7.

Fig. 2.6 The SDT-Q600 thermogravimetric analysis unit.

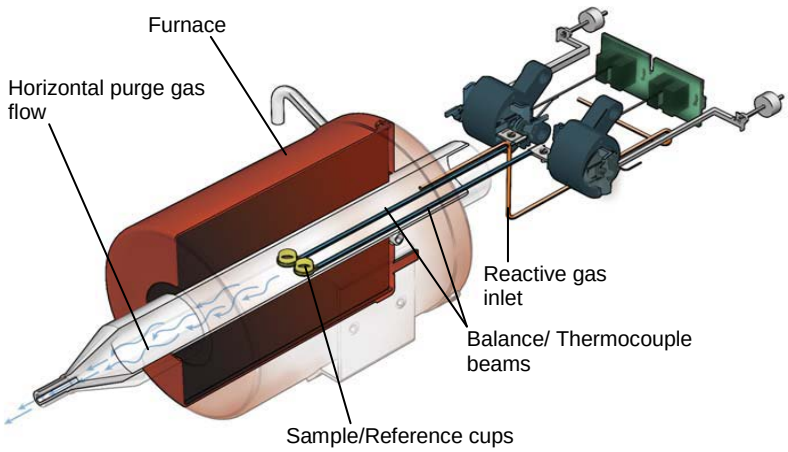

Fig. 2.7 A cross-section of the TGA furnace.

2.5 Gas analysis by gas chromatography

In the study of catalytic oxidative reaction of ethane (Chapter 3 and 6), product gas exiting from the top of reactor was collected using Tedlar gas sampling bags. The gas samples were analysed using two different gas chromatography (GC) systems. An HP 5890 GC equipped with a HayeSep DB column (15ft x 1/8 in.) and a flame ionization detector (FID) was used to quantify hydrocarbons in the product gases while other light gases were analysed using a Perkin Elmer Autosystem XL GC with a molecular sieve column (1 m x 1/8 in.), a Porapak N (3 m x 1/8 in) column and a thermal conductivity detector (TCD). For both GCs, argon was used as a carrier gas.

Gas species were quantified by reference to the calibration curves constructed using standard gas mixtures. All the standard calibration curves were prepared by measuring the ratio of component concentration to the peak area from gas chromatograms. The production rates (mmol min^{-1}) of various product species (other than H_2O) were calculated by considering the total gas flow rate used and the concentration of the species detected by the GCs using the following equation:

$$\text{Production rate of species A} = \frac{y_A \dot{V}}{\text{Molar volume of gas at } 25\ ^\circ\text{C}} \times 1000 \qquad (2.1)$$

where,

y_A = molar fraction of species A, as detected by GC

$\dot{V}$ = total gas flow rate of feed gas at at 25 °C (L min^{-1})

molar volume of gas at 25 °C = 22.465 L mol^{-1}

2.6 Catalyst characterisations by X-ray diffraction (XRD)

In this study, the XRD measurement at a step size of 0.019° and a step counting time of 0.7 sec was performed using a Bruker D8 Advance diffractometer (Cu Kα radiation, λ1=1.54053 Å; λ2=1.54431 Å) equipped with a LynxEye detector. The average size of crystallites was calculated using the Debye-Scherer equation:

$$L = \frac{K\lambda}{\beta \cos\theta} \tag{2.2}$$

where,

λ = wavelength of the X - rays

θ = diffraction angle

K = shape factor

β = peak width at half - maximum intensity

2.7 Other characterisation techniques

The fresh and spent catalysts were also characterised by the electron microscopy (EM) and the energy dispersive X-ray spectroscopy (EDX). The transmission electron microscopy (TEM) examinations were carried out by a JEOL 3000F FEG-TEM while the scanning electron microscopy (SEM) examinations were carried out by a JEOL JSM-6400F microscope.

N_2 adsorption experiments were performed using a Miromeritics Tristar-3000. The specific surface areas were calculated by the multipoint Brunauer-Emett-Teller (BET) method in the relative pressure (P/P_o) range of 0.05 – 0.30. For the supported catalysts used in this study, the pore volume was derived from the adsorption amount at a relative pressure (P/P_o) of 0.99 and the average pore width was calculated using the Barrett-Joyner-Hallenda (BJH) method.

2.8 References

[1] W.J. Lee, C.-Z. Li, Coke formation and reaction pathways of catalyst-surface-generated radicals during the pyrolysis of ethane using Ni mesh catalyst, Appl. Catal. A 316 (2007) 90-99.

[2] W.J. Lee, C.-Z. Li, Opposite effects of gas flow rate on the rate of formation of carbon during the pyrolysis of ethane and acetylene on a nickel mesh catalyst, Carbon 46 (2008) 1208-1217.

[3] D. Geldart, Types of gas fluidization, Powder Technol. 7 (1973) 285-292.

[4] W. Yao, G. Gu, W. Fei, W. Jun, Fluidization and agglomerate structure of SiO_2 nanoparticles, Powder Technol. 124 (2002) 152-159.

[5] J. Jung, D. Gidaspow, Fluidization of Nano-size Particles, J. Nanopart. Res. 4 (2002) 483-497.

[6] C. Zhu, Q. Yu, R.N. Dave, R. Pfeffer, Gas fluidization characteristics of nanoparticle agglomerates, AlChE J. 51 (2005) 426-439.

[7] L.F. Hakim, J.L. Portman, M.D. Casper, A.W. Weimer, Aggregation behavior of nanoparticles in fluidized beds, Powder Technol. 160 (2005) 149-160.

[8] J.R. Wank, S.M. George, A.W. Weimer, Nanocoating individual cohesive boron nitride particles in a fluidized bed by ALD, Powder Technol. 142 (2004) 59-69.

[9] L. Hakim, J. Blackson, S. George, A. Weimer, Nanocoating individual silica nanoparticles by atomic layer deposition in a fluidized bed reactor, Chem. Vap. Deposition 11 (2005) 420-425.

CHAPTER 3

Radical desorption and adsorption during the catalytic partial oxidation of ethane using nickel mesh catalyst

Overview:

The catalytic reactions between O_2 and hydrocarbons are an important class of reactions in energy and chemical industries. This study aims to investigate the complicated reactions involving reactive radicals on the catalyst surface and in the gas phase during the partial oxidation/combustion of light alkanes. In order to avoid intra-particle transport constraints associated with the traditional porous catalysts, a non-porous nickel mesh catalyst has been used in this study for the partial oxidation of ethane with O_2 at 625 °C at atmospheric pressure. The catalytic effects of the nickel mesh strongly depended on the flow rate of gas reactants passing through the mesh. At a low gas flow rate, the nickel mesh catalyst showed negative effects for the oxidation of ethane. At a high gas flow rate, the same catalyst showed positive catalytic effects. The results of this study can be explained by considering the selective/preferential adsorption and desorption of different radicals onto and from the catalyst surface.

3.1 Introduction

The catalytic reactions between O_2 and hydrocarbons are an important class of reactions in energy and chemical industries. The catalytic combustion of natural gas is a promising technology to drastically reduce the emissions of air pollutants from power generation activities. The catalytic partial oxidation of alkanes with O_2, on the other hand, remains as a potential clean alternative to the energy-intensive steam cracking of light alkanes [1] in the production of alkenes, especially ethylene and propylene whose demands continue to rise [2].

Traditionally, catalysts in the form of porous particles are normally employed to catalyse this type of reactions. There are, however, some great disadvantages associated with the use of porous catalysts especially for fast reactions such as hydrocarbon-O_2 reactions at high temperature. The reaction system can easily become rate-limited by mass and/or heat transfer.

At high temperature, the catalytic reactions of hydrocarbon-O_2 mixture are exceedingly complex. The heterogeneous and homogeneous reactions are coupled not only by adsorption and desorption of reactants and products molecules, but also by adsorption and desorption of radical intermediates. Significant evidence [3-12] exists to show that surface-generated radicals do not always continue their reactions on the catalyst surface but can also desorb from the surface to participate in the gas-phase reactions both outside the catalyst particle as well as inside the catalyst pore itself. When porous catalysts are used, the mass transfer limitation for reactive radicals inside the catalyst pores can become “irreducible” [13, 14]. Unlike the molecular species, the elimination of transport limitations for highly reactive radical species would require particle sizes that are too small to be achieved practically, for example, based on pressure drop consideration. It then becomes a forbidden task to understand the inter-influence between the reactions on the catalyst surface and those in the “gas phase” within the pores of a catalyst particle.

The dual roles of catalyst surface in generating and quenching the radical intermediates [9, 12-15] brings further intricacy in evaluating the exact contributions

of homogeneous and heterogeneous pathways to the overall reaction mechanism. When the radicals generated on the catalyst surface desorb into the gas phase, these radicals may initiate and speed up the gas-phase radical reactions. The catalyst would thus show positive effects on the observed reaction rates [3-5, 10]. On the other hand, when the radicals generated in the gas phase adsorb onto the catalyst surface [16], the chain of radical reactions in the gas phase would be effectively shortened. The catalyst would then show negative effects on the observed reaction rates.

For a non-porous mesh catalyst, the absence of a complicated internal porous structure means the automatic elimination of intra-particle diffusion resistance for the radicals, which would otherwise exist for a porous catalyst. Previous studies [8-12] using non-porous mesh catalysts have shown that the desorption of radicals from the catalyst surface into the gas phase can be effectively facilitated by decreasing the gas film thickness around the mesh wires. This was achieved conveniently by increasing the gas flow rate passing through the mesh catalyst [8-12]. Clearly, the non-porous mesh catalysts provide a convenient means to examine the effects of radical adsorption/desorption on the mechanisms of hydrocarbon reactions which are often overlooked in kinetic studies.

It has been shown [8, 12] that the desorption of radicals can not only change the observed reaction rates but also change the formation of carbon deposit on the catalyst surface. More recently, it was demonstrated [17] that the desorption of radicals from the catalyst surface can be used to control/enhance the growth of carbon nanofibres. The focus of the previous studies by this group on the catalytic reaction of light hydrocarbons with nickel mesh catalyst [8-11, 17] has mainly been on the adsorption and desorption of hydrocarbon radicals. In the study presented in this chapter, the aim was to investigate the adsorption and desorption of radicals in the more complicated ethane-O_2 reaction system where hydrocarbon radicals together with O-containing radicals (e.g. OH radicals) are present. Both positive and negative catalytic effects of a nickel mesh catalyst have been observed for this reaction system. The experimental observations are explained by considering the preferential adsorption and desorption of C_2H_5 and OH radicals.

3.2 Experimental

The experiments were carried out in a quartz tube reactor described earlier in Section 2.2. Reactant gases used were chemically pure grade ethane (99.00% purity) from BOC and the mixture of O_2 in argon balance (Coregas). The flow rates of the gases were controlled with mass flow controllers (Aalborg) separately and are reported throughout this chapter as the flow rates under normal ambient condition (25 ºC and 1 atm). With the pre-set ratios controlled by the mass flow controllers, all the gases were allowed to mix before being fed directly into the reactor from the bottom.

The reactor was operated both as a catalytic reactor with the presence of a wire mesh in the isothermal zone and as a non-catalytic reactor in the absence of wire mesh in a heated zone. In this study, experiments were also performed using three layers of nickel mesh, 5 mm apart, as catalyst. In the presence of the first piece of mesh, the temperature at locations 5 and 10 mm above the first mesh was measured, confirming that all meshes would be in the isothermal zone. In each experiment, the reactor was heated slowly from room temperature to 625°C in the isothermal zone after purging the reactor with the reactant gas. This temperature was chosen for this study because the non-catalytic reactions proceed significantly (but not excessively) under current experimental conditions. A significant extent of non-catalytic reactions is necessary in order to investigate the inter-influence between the reactions on the catalyst surface and those in the gas phase.

A K-type thermocouple was installed in contact with the mesh catalyst inside the quartz tube reactor to monitor the reaction temperature. All experiments were run for more than 120 min, during which the reaction rates reached their plateau values. After holding for 120 min, the reactor was immediately cooled to allow the mesh to drop to the bottom of the reactor. As soon as the mesh dropped, the temperature was once again raised to the same set temperature for the study of reactions without a catalyst (blank experiment). During the blank experiment, the thermocouple remained inside the reactor at the same location as in the corresponding catalytic experiment.

Reaction products were analysed by the gas chromatography units described in Chapter 2. The formation rates of various product species (other than H_2O) were calculated by considering the total gas flow rate and the concentration of the species as detected by the GCs. Each datum of product formation rate reported here represents an average of at least three samples taken after the reaction had reached its steady state during the same experiment.

3.3 Results and discussion

3.3.1 Gas-phase ethane oxidation

Extensive experiments with an empty reactor were carried out in order to understand the non-catalytic gas-phase reactions. Total gas flow rates were varied to see the effects of residence time on reactant conversion and product distributions. In all experiments, $C_2H_6/O_2/Ar$ feed composition was 10/5/85 (by vol) and the temperature inside the reactor was kept constant at 625 °C. Fig. 3.1 shows product formation rates at different total gas flow rates.

Mechanisms describing gas-phase reactions of ethane oxidation have been proposed in previous studies [3, 18-22]. A list of commonly accepted main elementary reactions in the absence of a catalyst is presented in Table 3.1. It should be emphasised that Table 3.1 is not meant to include hundreds of all possible elementary reactions but only to include the main reactions responsible for the formation and destruction of main products. In a purely homogenous system, two possibilities of ethane activation exist. Ethane can undergo unimolecular decomposition to form CH_3 radicals (3.1) or alternatively it may react with molecular oxygen to form C_2H_5 and HO_2 radicals (3.2). Using rate constant values in Table 3.1, the relative importance of radical initiations by reactions (3.1) and (3.2) can be estimated. Under the reaction conditions used in this study, i.e. 5.0% oxygen (6.8 x 10^{-4} mole/litre), 625 °C and 1 atm,

$$\frac{\text{rate}\,(3.1)}{\text{rate}\,(3.2)} = \frac{k_{3.1}}{k_{3.2}[O_2]} \approx 35$$

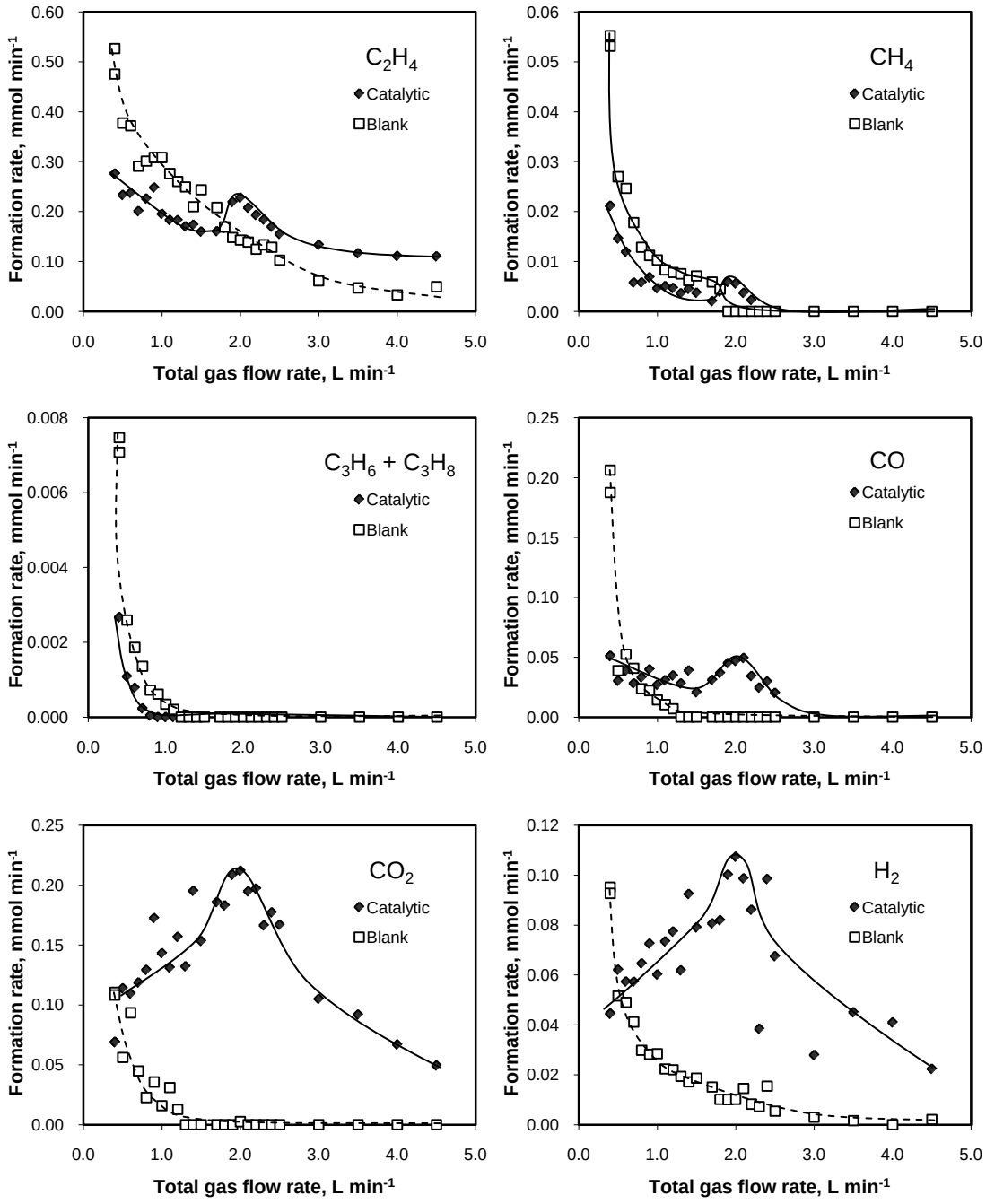

Fig. 3.1 Changes in product formation rates with the total gas flow rate from the catalytic and non-catalytic (blank) partial oxidation of ethane at 625 °C and atmospheric pressure with the feed composition of $C_2H_6/O_2/Ar$ = 10/5/85 (by vol).

Table 3.1 A list of main elementary gas-phase reactions and their rate constants under present (Chapter 3) experimental conditions.

No.	Reaction	k (sec^{-1}or $M^{-1}sec^{-1}$ or $M^{-2}sec^{-1}$) at 898K	Refs
	Initiation		
3.1	$C_2H_6 = CH_3 + CH_3$	9.17×10^{-5}	[21]
3.2	$C_2H_6 + O_2 = C_2H_5 + HO_2$	3.86×10^{-3}	[20]
3.3	$CH_3 + C_2H_6 = CH_4 + C_2H_5$	2.74×10^{6}	[21]
	Propagation		
3.4	$C_2H_5 + O_2 = C_2H_4 + HO_2$	2.47×10^{7}	[20]
3.5	$C_2H_5 = C_2H_4 + H$	3.63×10^{0}	[23]
3.6	$HO_2 + C_2H_6 = C_2H_5 + H_2O_2$	6.30×10^{4}	[20]
3.7	$2HO_2 = H_2O_2 + O_2$	2.00×10^{9}	[21]
3.8	$H_2O_2 + M = 2OH + M$	1.01×10^{3}	[22]
3.9	$OH + C_2H_6 = H_2O + C_2H_5$	3.53×10^{9}	[21]
	Termination		
3.10	$CH_3 + CH_3 = C_2H_6$	1.68×10^{10}	[20]
3.11	$C_2H_5 + C_2H_5 = C_2H_6 + C_2H_4$	1.40×10^{9}	[20]
3.12	$C_2H_5 + CH_3 = C_3H_8$	1.14×10^{10}	[24]
3.13	$C_2H_5 + CH_3 = C_2H_4 + CH_4$	2.43×10^{6}	[20]
3.14	$C_2H_5 + OH = C_2H_4 + H_2O$	2.41×10^{10}	[20]
3.15	$HO_2 + OH = H_2O + O_2$	2.00×10^{10}	[21]
	Reactions leading to CO_x and H_2 formation		
3.16	$C_2H_5 + HO_2 = CH_3 + CH_2O + OH$	2.50×10^{10}	[20]
3.17	$C_2H_5 + OH = CH_3 + CH_2O + H$	2.41×10^{10}	[20]
3.18	$C_2H_4 + OH = CH_3 + CH_2O$	1.17×10^{9}	[22]
3.19	$C_2H_4 + OH = C_2H_3 + H_2O$	7.31×10^{8}	[21]
3.20	$C_2H_3 + OH = C_2H_2 + H_2O$	3.00×10^{10}	[21]
3.21	$CH_2O + OH = CHO + H_2O$	1.53×10^{10}	[21]
3.22	$C_2H_2 + OH = CH_3 + CO$	2.76×10^{10}	[22]
3.23	$CH_3 + OH = CH_2O + H_2$	1.03×10^{10}	[21]
3.24	$CH_3 + HCO = CH_4 + CO$	9.05×10^{9}	[22]
3.25	$CO + OH = CO_2 + H$	1.79×10^{8}	[21]
3.26	$H + H + M = H_2 + M$	7.13×10^{8}	[21]

Therefore, reaction (3.1), followed by reaction (3.3), is the main initiation step of the radical chain reactions in the gas phase. It should be noted that the chain initiation through reactions (3.1) and (3.3) or through reaction (3.2) would lead to the same radical of C_2H_5 for further reactions.

The resulting ethyl radicals will then transform into ethylene by direct attack of oxygen molecule (3.4) or through its thermal decomposition (3.5). However, from the following expression,

$$\frac{\text{rate(3.4)}}{\text{rate(3.5)}} = \frac{k_{3.4}[O_2]}{k_{3.5}} \approx 4600$$

reaction (3.4) is the prevailing pathway for ethylene formation. The HO_2 radical produced by reaction (3.4) can abstract hydrogen from another ethane molecule to return an ethyl radical while producing hydrogen peroxide (3.6). Hydrogen peroxide acts as a chain branching agent whereby its decomposition through reaction (3.8) yields more reactive OH radicals [3, 19]. As the reaction proceeds inside the reactor, the concentration of HO_2 radicals will increase rapidly and as a result, reaction (3.7) is promoted more than reaction (3.6) [18]. Likewise, the concentration of OH radicals will also increase and hence reaction (3.9) immediately becomes the primary reaction for ethane consumption [18].

From this mechanism in Table 3.1, it is obvious that OH radicals play crucial roles in the gas-phase reactions involving ethane and oxygen. Since this radical is very reactive, it will not only act as a hydrogen abstractor from ethane molecules (3.9) but also responsible for further degradation of C_2H_4 which ultimately leads to the formation of CO, CO_2 and H_2 as terminal products as is described in Table 3.1.

In this study, the oxidation of ethane in the empty reactor shows typical behaviour of a radical chain process. As is shown in Figs. 3.1 and 3.2, the gas-phase non-catalytic reaction rates, labelled as “blank”, were observed to increase monotonically with decreases in the total gas flow rate. This implies that the gas-phase reactions were profoundly dependent on the concentrations of various free radicals [18]. During a blank experiment at a high gas flow rate, the short residence time did not generate radicals at concentrations high enough to allow the reactions to take place at

high rates. Short residence time also means that the radicals and the reactants did not have enough time to react in the heated zone. At high gas flow rates (>2.0 L min^{-1}) where C_2H_6 conversion was found to be very low, C_2H_4 turned out to be practically the only C-containing product species. As the conversion increased with increasing residence time, other species started to show up in the product gas. Changes in product selectivities (Fig. 3.3) are mainly attributed to the degradation of C_2H_4 through reactions (3.18) to (3.26) as the gas spent relatively longer time inside the reactor. As presented in Table 3.1, the pathway for C_2H_4 degradation involves OH radical attack to yield CO_x, H_2 and H_2O via various intermediates such as C_2H_3, CH_3 and CH_2O.

3.3.2 Catalytic partial oxidation of ethane using a single layer of nickel mesh catalyst

Product formation rates in the presence of a single layer of mesh catalyst are also plotted in the same figure (Fig. 3.1) as for the blank experiments in order to facilitate comparison between catalytic and non-catalytic reactions. In contrast to the results obtained in the blank experiments where formation rates of all products increase monotonically with decreasing gas flow rate, reactions with the nickel mesh catalyst exhibit more complex patterns. From Fig. 3.1, the effects of nickel mesh catalyst can be broadly divided into two distinct regions. One is the lower flow rate region (< 1.7 L min^{-1}) in which formation rates of hydrocarbon products particularly C_2H_4 were lower ("negative catalytic effects") than that obtained by the reactions without a catalyst. Another is the higher flow rate region (> 1.7 L min^{-1}) where "positive catalytic effects" in term of product formation rates and reactant conversions were observed.

3.3.2.1 Quenching of radicals – negative catalytic effects of mesh catalyst

A careful comparison of reactant conversions between blank and catalytic experiments (Fig. 3.2) reveals that there was a slight decrease in the conversion of ethane in the catalytic experiments compared to the blank ones at the very low gas flow rates (<1.7 L min^{-1}). As can be seen from Fig. 3.1, significant amounts of product species were formed from the homogeneous non-catalytic reactions in this

region. Mass balance calculation also indicated that appreciable amounts of H_2O (not shown in the graph) were also formed from the gas-phase reactions. The adsorption of product molecules (e.g. CO_2 and H_2O) onto the catalyst surface could have inhibited the reaction on the catalyst surface [11, 25, 26]. However, this inhibition could at most give similar C_2H_6 conversions, but would not cause decreases in C_2H_6 conversion as was observed experimentally (Fig. 3.2).

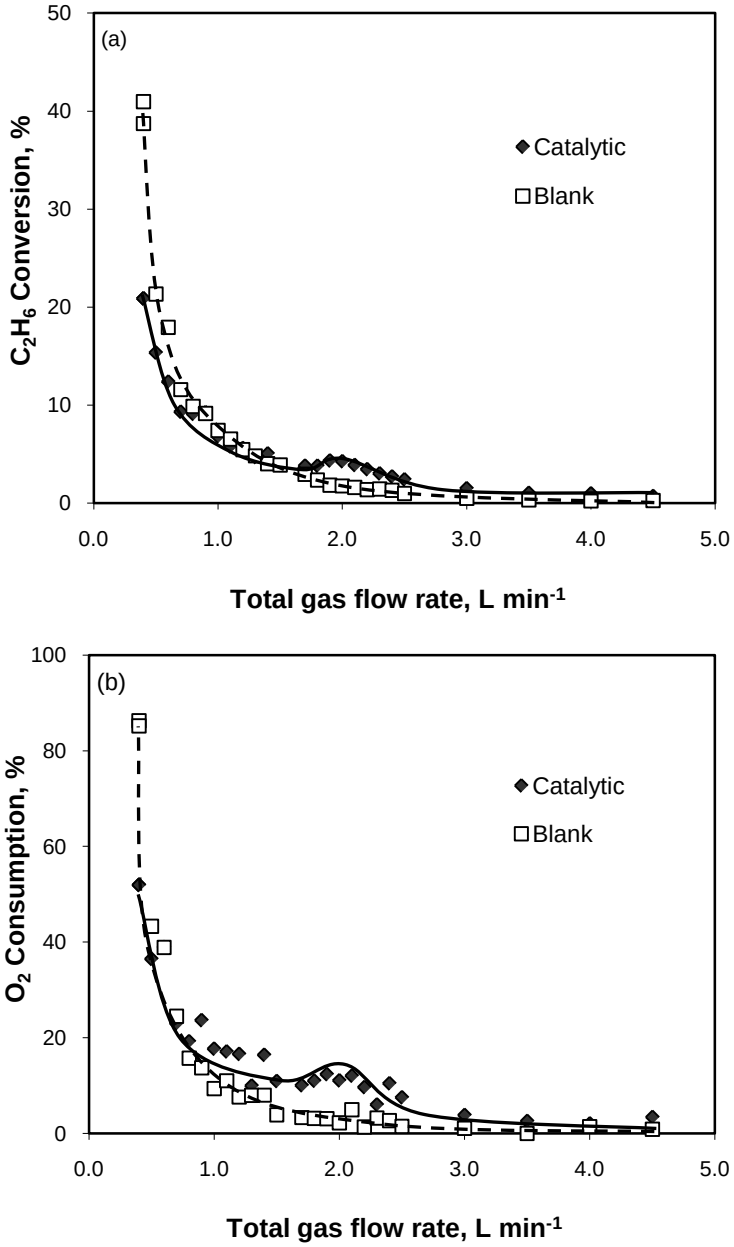

Fig. 3.2 Changes in ethane conversion (a) and oxygen consumption (b) with the total gas flow rate. T = 625 °C and $C_2H_6/O_2/Ar$ = 10/5/85.

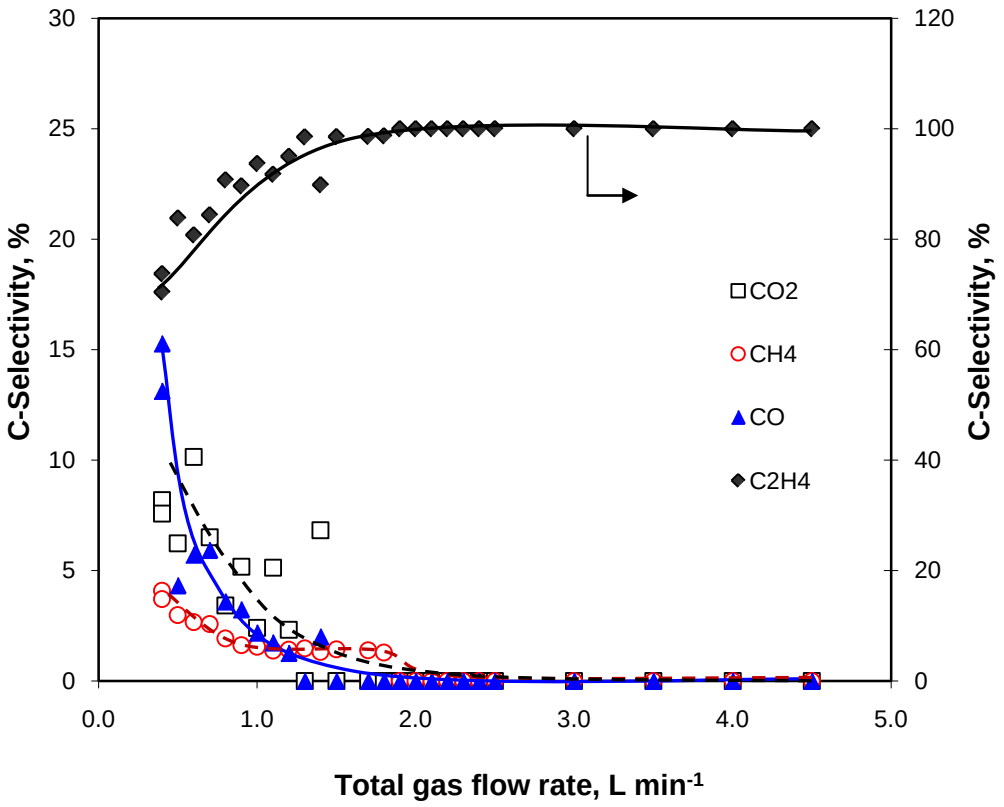

Fig. 3.3 Changes in C-selectivity with the total gas flow rate for the non-catalytic partial oxidation of ethane at 625 °C and $C_2H_6/O_2/Ar$ = 10/5/85.

It is believed that the presence of a nickel mesh has disrupted the chain reactions in the gas phase by providing a surface to catalyse the radical termination reactions, i.e. the "negative catalytic effect". More than one type of radical species could be quenched on the catalyst surface. However, the data in Fig. 3.2 show a bigger negative effect of catalyst on formation rates of C_2H_4 and other hydrocarbon products than other products. Therefore, hydrocarbon radicals would be quenched the most. Hydrocarbon radicals such as C_2H_5 and CH_3 formed in the gas phase upstream of the Ni mesh may collide with the catalyst surface to form alkoxide species. Collision between a methyl radical and catalyst surface is believed to result in the formation of surface methoxide [15]. Similarly, the collision of an ethyl radical with the nickel

mesh catalyst covered by the adsorbed oxygen species in this study could result in the formation of surface ethoxy species:

$$CH_3\ (g) + O^-\ (s) = CH_3O\ (s) \quad (3.27)$$

$$C_2H_5\ (g) + O^-\ (s) = C_2H_5O\ (s) \quad (3.28)$$

The unstable surface ethoxide can be transformed to ethylene. However, if ethylene fails to diffuse immediately into the bulk gas stream, reaction (3.29) can then be easily shifted to the right [27, 28] to form thermodynamically more stable CO_x in the same way as that of the methoxide degradation (3.30) [15]:

$$C_2H_4\ (s) + OH\ (s) \leftrightarrow C_2H_5O\ (s) \rightarrow CH_3COO\ (s), HCOO\ (s) \rightarrow CO_x \quad (3.29)$$

$$CH_3O\ (s) \rightarrow HCOO \rightarrow CO_x \quad (3.30)$$

While the formation and degradation of surface alkoxide species, as outlined above, may explain the increased formation of CO_2 (Fig. 3.1) in the presence of the mesh catalyst, other reactions on catalyst surface must be considered to account for the decreases in the ethane conversions due to the presence of the mesh catalyst as shown in Fig. 3.2. It is suspected that C-containing radicals could adsorb on Ni surface and then recombine to form the original C_2H_6, e.g. through reactions (3.31) and (3.32):

$$CH_3\ (s) + CH_3\ (s) = C_2H_6\ (s) \quad (3.31)$$

$$C_2H_5\ (s) + C_2H_5\ (s) = C_2H_6\ (s) + C_2H_4\ (s) \quad (3.32)$$

Clearly, reaction (3.32) is more important than reaction (3.31) because C_2H_5 would be more populated than CH_3.

Another possible mechanism of negative catalytic effect is the quenching of the O-containing radicals [13-15]. As discussed in Section 3.3.1, O-containing radicals

(HO_2 and OH) are very important chain-carriers in the gas-phase reaction network. Since their reactions are so crucial in the activation/consumption of ethane and also in the subsequent reactions involving radicals and molecular products, the depletion in their concentration will lead to the decrease in the overall conversion of C_2H_6. In this study, however, it is believed that the quenching of the O-containing radicals was less significant than that of the hydrocarbon radicals. As will be discussed later in the next section, under the experimental conditions of this study, it is expected that surface-generated O-containing radicals will have more tendency to desorb from the catalyst surface. By considering the reversibility at the micro molecular level, species easy to desorb must not adsorb easily. It is therefore presumed that the quenching of the oxygen-containing radicals had less effects on the inhibition of the gas-phase reactions observed in this study. Indeed, if HO_2/OH radicals are quenched more than the hydrocarbon radicals, the adverse effects of radical quenching must have been seen more profoundly on the formation rates of the degradation products (CO_x), due to their ability to facilitate deep oxidation [29], which is opposite to the experimental observation: the CO_2 formation rate actually increased due to the mesh catalyst (see Fig. 3.1).

3.3.2.2 Radical desorption – positive catalytic effects of mesh catalyst

Although the catalytic formation rate of C_2H_4 was lower than the blank at low gas flow rates (< 1.7 L min^{-1}), an abrupt increase within a narrow flow rate range was observed when the flow rate was increased from 1.7 L min^{-1} to 2.0 L min^{-1} (Fig. 3.1). This somewhat unusual "abrupt-effect" of gas flow rate is however completely unexplained by the theory of molecular species diffusion. This is because the mass transfer of molecular species to and from the catalyst alone would only exhibit a monotonic pattern in product formation rate [12], which is absolutely contrary to that observed in this study (Fig. 3.1).

A plausible explanation of the above observation is the change in the mass transfer of reactive radical species [8-12]. It is widely accepted [6, 25] that the first step in the catalytic activation of saturated light hydrocarbon involves the breaking of C-H bond on an active surface site to form radicals. In the case of ethane, the

molecule could dissociatively adsorb on the nickel metallic sites to form C_2H_5 and H radicals:

$$C_2H_6\,(g) = C_2H_5\,(s) + H\,(s) \qquad (3.33)$$

The dissociative adsorption of C_2H_6 took place concurrently with the adsorption of another reactant O_2:

$$O_2\,(g) = 2O^-\,(s) \qquad (3.34)$$

Therefore, an alternative step of C_2H_6 initiation is likely to be the reaction of C_2H_6 with the adsorbed oxygen atoms rather than its direct adsorption on the clean surface:

$$C_2H_6\,(g) + O^-\,(s) = C_2H_5\,(s) + OH\,(s) \qquad (3.35)$$

In fact, it was found in the past [30-33] that oxygen species adsorbed on Ni surface has promoted C-H bond cleavage during the catalytic oxidation of methane.

Taking into account of reactions (3.33) – (3.35), it is clear that four types of reactive species, namely O(s), H(s), OH(s) and C_2H_5(s), were present on the catalyst surface. The tendency of each type of the species to desorb from the surface is largely determined by the strength of their bonding with Ni surface. The binding energies of O-Ni, H-Ni, OH-Ni and C_2H_5-Ni at zero coverage are 115, 63, 60.9 and 49 kcal/mol [34-36], respectively. The strength of OH-Ni bond is however very dependent on the surface oxygen coverage. Patrito et al. [37] have studied the energetics of hydroxyl adsorption on Ni and other metals. They found that high oxygen coverage lowers the OH-Ni bond strength from 60.9 kcal/mol at the zero coverage to 42.9 kcal/mol and 33.9 kcal/mol at the surface coverages of 0.6 and 1, respectively. The effects of oxygen coverage on the desorption of OH from Ni surface were observed by other researchers [38, 39] where variation in the activation energy of OH desorption was reported.

Under current experimental conditions, low gas flow rates caused a thick and relatively stagnant gas film to be developed around the Ni wire mesh. The thick gas film would bring a difficulty for the radicals to diffuse into the bulk gas phase. Hence, few radicals would manage to desorb into the gas phase before they are consumed within the gas film. The increase in the gas flow rates (0.4 L min^{-1} to ~2.0 L min^{-1}) decreased the thickness of the gas film around the mesh. The desorption and diffusion of the radicals into the gas phase then became easier [8-12]. Under the reaction conditions employed in this study, where high oxygen coverage is expected, it is believed that the less tightly held OH radicals could desorb into the gas phase once the gas film thickness was reduced with increasing flow rate. The desorption of OH radicals from Ni surface has, in fact, been detected in the past studies [39, 40] using a laser-induced fluorescence technique during the reaction of H_2 and O_2.

The desorption of OH radicals from the catalyst increased the concentration of OH radicals in the gas phase, which in turn resulted in the increases in the overall gas-phase reaction rate. As can be seen in reactions (3.9), (3.14), (3.15), and (3.17) to (3.26), OH radicals are involved in both C_2H_6 consumption and many parts of deep oxidation mechanisms that lead to the formation of CO. Further reactions of OH with CO yield the thermodynamically stable CO_2 product together with H radical. One fate of H radicals would be their recombination to form H_2. Therefore, the desorption of OH radicals will increase the consumption of C_2H_6 (Fig. 3.2) and the formation of C_2H_4 and other products including CO, CO_2 and H_2 (Fig. 3.1). However, as OH radicals are involved in many rapid deep oxidation reactions [e.g. reactions (3.17) to (3.26)], the increased OH radical concentration in the gas phase would certainly speed up these deep oxidation reactions more than the reactions for the formation of C_2H_4 [e.g. reactions (3.9) and (3.4)]. This explains why the selectivity of C_2H_4 decreased while that of CO_2 increased (Fig. 3.5) as the flow rate was increased up to 2.0 L min^{-1}.

At very high gas flow rates (>2.0 L min^{-1}), the mass transfer resistance for the desorption of OH radicals from the catalyst surface is very small and no longer the rate-limiting step. The rates of OH radical generation on catalyst, which are chemical reactions, become the rate-limiting step. Hence, further increases in the total gas flow

rate beyond 2.0 L min^{-1} would not result in further increases in the rate of OH radical generation and desorption. Instead, further increases in gas flow rate beyond this point would only dilute the concentrations of OH radical in the gas phase downstream the catalyst. The combined effects of decreased radical concentration and decreased residence time for subsequent reactions in the gas-phase reaction at the higher flow rates (beyond 2.0 L min^{-1}) result in decreases in the reaction rates.

The explanation outlined here provides a plausible explanation for the decreases in the catalytic formation rates of all products (C_2H_4, CH_4, CO, CO_2 and H_2) at flow rates higher than 2.0 L min^{-1} (Fig. 3.1). The changes in product selectivity (Fig. 3.4) with increasing gas flow rate (>2.0 L min^{-1}) are due to two related reasons. Firstly, decreased OH radical concentration due to the dilution effect mentioned above would also decrease the relative importance of deep oxidation reactions [reactions (3.17) to (3.26)]. This contributes to the increases in the selectivity of C_2H_4 and the decreases in the selectivities of CO_2 and CO (Fig. 3.5) from the catalytic reactions at total gas flow rates higher than 2.0 L min^{-1}. Secondly, further increase in the gas flow rate beyond 2.0 L min^{-1} would mean shorter time spent in the heated zone of the reactor by C_2H_4 product molecules, allowing them to exit from the reactor before they were destroyed to CO_x, H_2 and H_2O

3.3.3 Effects of reactant partial pressures

In this study, the experiments at different ethane/oxygen partial pressures have been carried out in order to justify the above discussion made on the radical quenching and radical desorption. With the total pressure remained at atmospheric, the reactant partial pressures were varied by changing the relative proportions of C_2H_6 and O_2 while the percentage of argon dilution was kept at 85%. In this examination, two different flow rates were chosen (1.5 L min^{-1} and 3.5 L min^{-1}) to represent two different regions: the region of negative catalytic effect and the region of positive catalytic effect respectively.

As noted in the previous sections, gas-phase activation via reactions (3.1) and (3.3) are dominant at lower flow rates. Increasing C_2H_6 partial pressure will promote

these activation reactions. However, due to the importance of O_2 in the propagation steps, continued increases in the C_2H_6 partial pressure would not always result in continuous increases in the overall reactions rate. As is clearly shown in Fig. 3.5, the formation rates of C_2H_4 from the catalytic and non-catalytic reactions increased initially as the C_2H_6 partial pressure was increased. Further increases in the C_2H_6 partial pressure for the reactions at 1.5 L min^{-1} however resulted in the catalytic formation rate of C_2H_4 to approach its maximum value. It is also obvious in Fig. 3.5 that the formation rate of C_2H_4 and the conversion of C_2H_6 were always lower in the presence than in the absence of a mesh catalyst during reactions at 1.5 L min^{-1} even around the maximum values. This has given further evidence on the dominance of the gas phase reactions at lower flow rate region and the effect of radical quenching during catalytic reactions in this region.

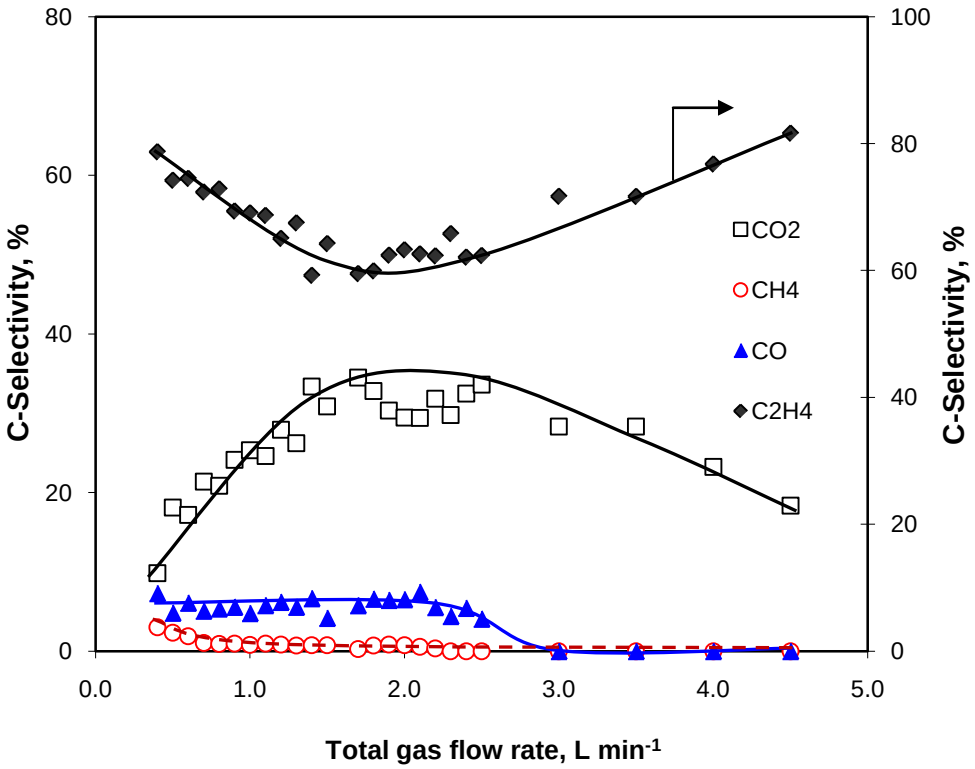

Fig. 3.4 Changes in C-selectivity with the total gas flow rate for the catalytic partial oxidation of ethane at 625 °C and $C_2H_6/O_2/Ar$ = 10/5/85.

The reactions in the higher flow rate region are more influenced by the activation on the catalyst surface and the desorption of radicals. At 3.5 L min^{-1}, the catalytic reaction rates at all C_2H_6 partial pressures studied showed larger values than those obtained from the blank experiments. Within this range of C_2H_6/O_2 ratio (partial pressures), O_2 did not become a limiting reactant on the catalyst surface, as is evidenced by its low conversion (Fig. 3.5). Increasing C_2H_6 partial pressure could promote surface activation via reaction (3.35) and consequently resulted in the increased formation of surface-generated OH radicals which subsequently desorbed into the gas phase to enhance ethane consumption via reaction (3.9). It is clear that two consequences existed when the C_2H_6 partial pressure was increased at 3.5 L min^{-1}. One was the increase in ethane activation on the catalyst surface and another was the increase in the reaction of ethane with OH radicals in the gas phase. These two effects combine to provide a conceivable explanation to the non-linear increase (Fig. 3.5) of catalytic reaction rates with increasing C_2H_6 partial pressure observed at the flow rate of 3.5 L min^{-1}.

3.3.4 Further study using 3 layers of nickel mesh

Further investigation was carried out by employing three pieces of nickel mesh. In these experiments, the meshes were placed in the isothermal zone with a distance of about 5 mm apart. The first layer of mesh was always ensured to be in the position identical to that in the experiments using one piece of mesh. The second and third pieces were down stream (physically on top of) of the first (see Fig. 2.1). The "net" catalytic contributions in term of reactant conversions and product formation rates were calculated by subtracting the rates of the blank experiments from the ones obtained with Ni mesh (1 or 3 layers) at the same flow rate (Figs. 3.6 and 3.7).

Surprisingly, increasing catalyst surface area by increasing the number of mesh pieces did not always bring a proportional increase in reactant conversion. As is shown in Fig. 3.6, extra catalyst surface area had a promoting effect on ethane and oxygen conversion at higher flow rate (>1.5 L min^{-1}) region. However, at the lower flow rate (< 0.8 L min^{-1}) region, reactant conversions (especially C_2H_6) were much lower than those of the blank experiments.

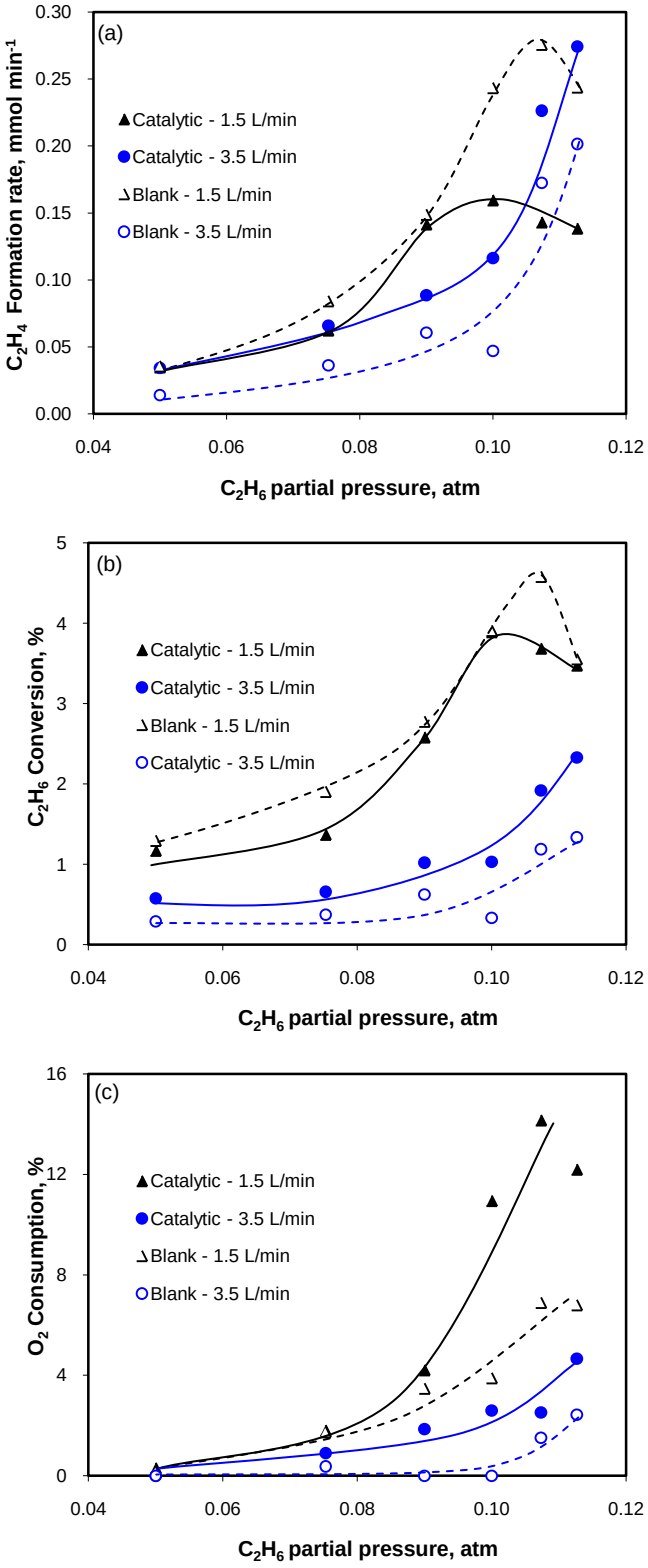

Fig. 3.5 Effects of C_2H_6 partial pressure on (a) C_2H_4 formation rate, (b) C_2H_6 conversion and (c) O_2 consumption at total gas flow rate of 1.5 L min^{-1} and 3.5 L min^{-1}

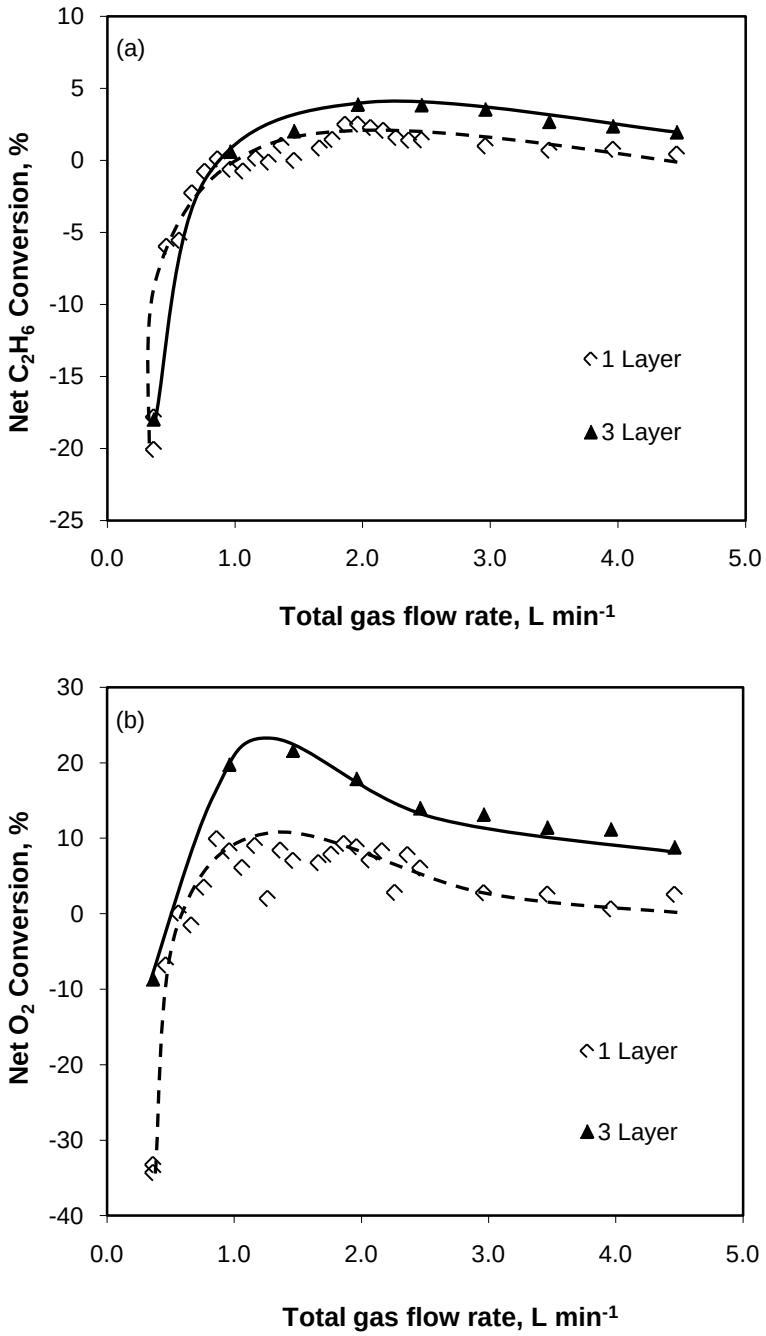

Fig. 3.6 Effects of increasing number of Ni mesh layers on (a) net-catalytic C_2H_6 conversion and (b) net-catalytic O_2 consumption.

As can be seen in Fig. 3.7, the use of three layers of nickel mesh tended to give higher formation rates of CO_2 and H_2 than that obtained with a single layer of mesh. The formation rates of other products (mainly C_2H_4) however only increased at high flow rates (>2.0 L min^{-1}) but dropped significantly at low flow rates (<2.0 L min^{-1}). The C_2H_4 formation rates at high flow rates though did not increase to the same magnitude as the increases in CO_x and H_2.

The results using 3 layers of mesh support the discussion presented in previous sections on the roles of mesh catalyst. In particular, the large negative impact on the formation rates of hydrocarbon products at lower flow rates further confirms that the radical species which has been quenched most by the catalyst surface at lower flow rates region must be hydrocarbon radicals (e.g. C_2H_5). It is also clear that the desorption of surface-generated O-containing radicals (OH radicals) has resulted in the enhanced reaction rates to form CO_x and H_2 more than C_2H_4. Some C_2H_5 radicals desorbed form the earlier catalyst layer may have been quenched by the next catalyst layer. This explains why C_2H_4 formation rates at high gas flow rates did not increase to the same magnitude as the increase in CO_x and H_2 when the number of catalyst layer was increased from one layer to three layers.

The void regions in between mesh pieces at least partly represent the situations inside the pores of a porous catalyst through which radicals have to diffuse to reach the bulk stream of the gas flow. Inside these regions, radicals could have migrated from one catalyst surface to another catalyst surface and many reactions could take place on them before they exit the catalyst zone. Although the actual situations inside the pore structure of a porous catalyst are much more complicated than the (5 mm apart) space between the mesh pieces, the heterogeneous-generation, desorption and quenching of the radicals observed from the experiments using three layers of mesh have nevertheless given some insights into the potential reaction mechanisms in the pores of a traditional porous catalyst.

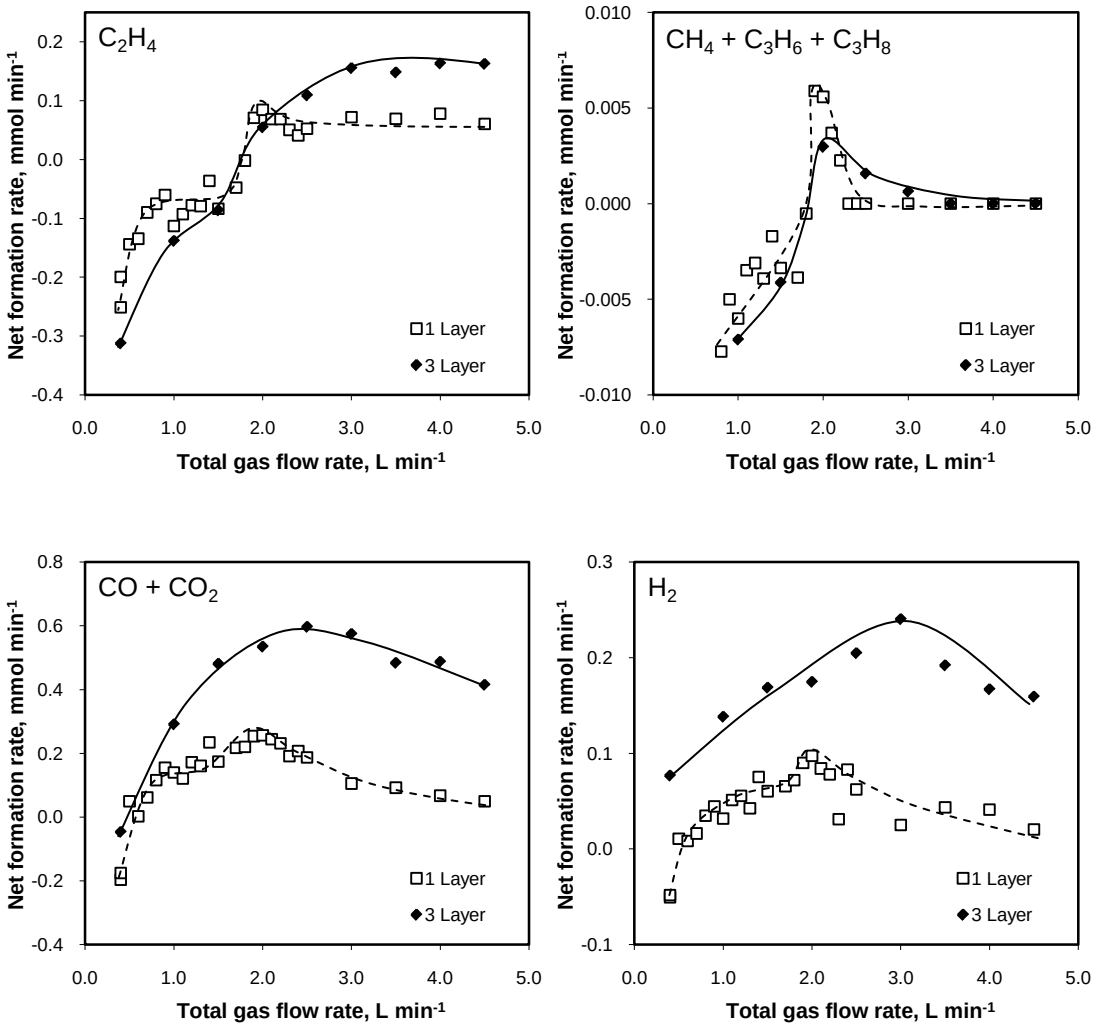

Fig. 3.7 Comparison of product net-catalytic formation rates from reactions with 1 layer of mesh catalyst and 3 layers of mesh catalyst.

3.4 Conclusions

A catalyst may influence the gas-phase radical chain reactions in two different ways. In this study using a non-porous nickel mesh catalyst for the partial oxidation of ethane, the exact catalytic effects of the catalyst strongly depended on the flow rate of gas reactants passing through the mesh. At a low gas flow rate, the nickel mesh catalyst showed negative effects for the oxidation of ethane due to the quenching of hydrocarbon radicals (e.g. C_2H_5) by the catalyst. At a high gas flow rate, the same catalyst showed positive catalytic effects due to the selective/preferential desorption of some radicals such as OH radicals from the catalyst surface. The overall effects of radical desorption would be the preferential increases in the formation of terminal products (CO_2 and H_2) relative to the formation of C_2H_4. The results of the study presented in this chapter will be valuable both in the fundamental research for the rethinking of the reaction mechanism and in the applied research for the improvement in catalyst and process design related to any catalytic conversion of light hydrocarbons.

3.5 References

[1] T. Ren, M. Patel, K. Blok, Olefins from conventional and heavy feedstocks: Energy use in steam cracking and alternative processes, Energy 31 (2006) 425-451.

[2] M. Eramo, Ethylene, propylene demand will experience increased growth in 2005-10, Oil Gas J. 103, (2005) 52-60.

[3] E. Morales, J.H. Lunsford, Oxidative dehydrogenation of ethane over a lithium-promoted magnesium-oxide catalyst, J. Catal. 118 (1989) 255-265.

[4] J.H. Lunsford, The role of surface-generated gas-phase radicals in catalysis, Langmuir 5 (1989) 12-16.

[5] K.D. Campbell, J.H. Lunsford, Contribution of gas-phase radical coupling in the catalytic-oxidation of methane, J. Phys. Chem. 92 (1988) 5792-5796.

[6] K.T. Nguyen, H.H. Kung, Generation of gaseous radicals by a V-Mg-O catalyst during oxidative dehydrogenation of propane, J. Catal. 122 (1990) 415-428.

[7] F. Gudmundson, J.L. Persson, M. Försth, F. Behrendt, B. Kasemo, A. Rosén, OH Gas Phase Chemistry outside a Pt Catalyst, J. Catal. 179 (1998) 420-430.

[8] E.B.H. Quah, C.-Z. Li, Effects of radical desorption on catalyst activity and coke formation during the catalytic pyrolysis and oxidation of light alkanes, Appl. Catal. A 250 (2003) 83-94.

[9] E.B.H. Quah, C.-Z. Li, Roles of desorbed radicals and reaction products during the oxidation of methane using a nickel mesh catalyst, Appl. Catal. A 258 (2004) 63-71.

[10] E.B.H. Quah, C.-Z. Li, Pyrolysis of liquefied petroleum gas assisted by radicals desorbed from mesh catalyst surface, Int. J. Chem. Kinet. 35 (2003) 637-646.

[11] E.B.H. Quah, J.F. Mathews, C.-Z. Li, Interinfluence between reactions on the catalyst surface and reactions in the gas phase during the catalytic oxidation of methane with air, J. Catal. 197 (2001) 315-323.

[12] W.J. Lee, C.-Z. Li, Coke formation and reaction pathways of catalyst-surface-generated radicals during the pyrolysis of ethane using Ni mesh catalyst, Appl. Catal. A 316 (2007) 90-99.

[13] P.M. Couwenberg, Q. Chen, G.B. Marin, Irreducible mass-transport limitations during a heterogeneously catalyzed gas-phase chain reaction: oxidative coupling of methane, Ind. Eng. Chem. Res. 35 (1996) 415-421.

[14] P.M.P. Couwenberg, Q. Chen, G.B. Marin, Kinetics of a gas-phase chain reaction catalyzed by a solid: the oxidative coupling of methane over Li/MgO-based catalysts, Ind. Eng. Chem. Res. 35 (1996) 3999-4011.

[15] Y.S. Su, J.Y. Ying, W.H. Green, Upper bound on the yield for oxidative coupling of methane, J. Catal. 218 (2003) 321-333.

[16] R.C. Burch, M.E. Crabb, Homogeneous and heterogeneous contributions to the catalytic oxidative dehydrogenation of ethane, Appl. Catal. A 97 (1993) 49-65.

[17] W.J. Lee, C.-Z. Li, Opposite effects of gas flow rate on the rate of formation of carbon during the pyrolysis of ethane and acetylene on a nickel mesh catalyst, Carbon 46 (2008) 1208-1217.

[18] D.M. Kulich, J.E. Taylor, Mathematical simulation of oxygen-ethane reaction, Int. J. Chem. Kinet. 7 (1975) 895-905.

[19] J.E. Taylor, D.M. Kulich, Homogeneous gas-phase pyrolyses with a wall-less reactor. III. The oxygen-ethane reaction. A double reversal in oxygen and surface effects, Int. J. Chem. Kinet. 5 (1973) 455-468.

[20] P. Dagaut, M. Cathonnet, J.C. Boettner, Kinetics of ethane oxidation, Int. J. Chem. Kinet. 23 (1991) 437-455.

[21] Y. Hidaka, K. Sato, H. Hoshikawa, T. Nishimori, R. Takahashi, H. Tanaka, K. Inami, N. Ito, Shock-tube and modeling study of ethane pyrolysis and oxidation, Combust. Flame 120 (2000) 245-264.

[22] C.K. Westbrook, F.L. Dryer, Chemical kinetic modeling of hydrocarbon combustion, Prog. Energy Combust. Sci. 10 (1984) 1-57.

[23] Y. Hidaka, K. Kimura, K. Hattori, T. Okuno, Shock tube modeling study of ketene oxidation, Combust. Flame 106 (1996) 155-167.

[24] S. Mousavipour, A theoretical study on the kinetics of disproportionation versus association reaction of $CH_3 + C_2H_5$, J. Phys. Chem. A 107 (2003) 8566-8574.

[25] R. Burch, M.J. Hayes, C-H bond activation in hydrocarbon oxidation on solid catalysts, J. Mol. Catal. A: Chem. 100 (1995) 13-33.

[26] L. Leveles, K. Seshan, J.A. Lercher, L. Lefferts, Oxidative conversion of propane over lithium-promoted magnesia catalyst: I. Kinetics and mechanism, J. Catal. 218 (2003) 296-306.

[27] E. Heracleous, A.A. Lemonidou, Homogeneous and heterogeneous pathways of ethane oxidative and non-oxidative dehydrogenation studied by temperature-programmed reaction, Appl. Catal. A 269 (2004) 123-135.

[28] E. Heracleous, A.A. Lemonidou, Reaction pathways of ethane oxidative and non-oxidative dehydrogenation on gamma-Al_2O_3 studied by temperature-programmed reaction (TP-reaction), Catal. Today 112 (2006) 23-27.

[29] J.C. Mackie, J.G. Smith, P.F. Nelson, R.J. Tyler, Inhibition of C_2 oxidation by methane under oxidative coupling conditions, Energy Fuels 4 (1990) 277-285.

[30] G. Krishnan, H. Wise, Interaction of methane and carbon monoxide with oxygen adspecies on Ni(111), Appl. Surf. Sci. 37 (1989) 244-249.

[31] C.T. Au, M.S. Liao, C.F. Ng, A detailed theoretical treatment of the partial oxidation of methane to syngas on transition and coinage metal (M) catalysts (M = Ni, Pd, Pt, Cu), J. Phys. Chem. A 102 (1998) 3959-3969.

[32] Y.H. Hu, E. Ruckenstein, Pulse-MS study of the partial oxidation of methane over Ni/La_2O_3 catalyst, Catal. Lett. 34 (1995) 41-50.

[33] O. Dewaele, G.F. Froment, TAP study of the mechanism and kinetics of the adsorption and combustion of methane on Ni/Al_2O_3 and NiO/Al_2O_3, J. Catal. 184 (1999) 499-513.

[34] E. Shustorovich, The bond-order conservation approach to chemisorption and heterogeneous catalysis: applications and implications, Adv. Catal. 37 (1990) 101-163.

[35] A.A. Zeigarnik, C. Callaghan, R. Datta, I. Fishtik, E. Shustorovich, Prediction of comparative catalytic activity in the series of single crystalline surfaces in a water-gas shift reaction, Kinet. Catal. 46 (2005) 509-515.

[36] A.T. Bell, E. Shustorovich, Analysis of the thermochemistry of C_2 hydrocarbons on transition metal surfaces using refined BOC-MP approach, Surf. Sci. 235 (1990) 343-350.

[37] E.M. Patrito, P.P. Olivera, H. Sellers, The nature of chemisorbed hydroxyl radicals, Surf. Sci. 306 (1994) 447-458.

[38] H. Yang, J.L. Whitten, Energetics of hydroxyl and influence of coadsorbed oxygen on metal surfaces, J. Phys. Chem. B 101 (1997) 4090-4096.

[39] J.T. Keiser, M.A. Hoffbauer, M.C. Lin, Production of hydroxyl on polycrystalline nickel studied by thermal desorption/laser-induced fluorescence, J. Phys. Chem. 89 (1985) 2635-2638.

[40] S. Ljungstrom, J. Hall, B. Kasemo, A. Rosen, T. Wahnstrom, A comparative study of OH radical desorption in the $H_2 + O_2$ reaction on Pt, Pd, Rh, Ir, and Ni, J. Catal. 107 (1987) 548-556.

CHAPTER 4

Effects of crystallite size on the kinetics and mechanism of NiO reduction

Overview:

This chapter deals with the kinetic investigation on the reduction of nanometer-size nickel oxide particles (supported and unsupported) with hydrogen. The change in the reduction behaviour was found to be related to the average size of NiO crystallites. When the NiO crystallite size was < about 20 nm, the dissociation of H_2 was the key rate-limiting factor and remained unchanged almost throughout the reduction process. However, when the NiO crystallite size was > 20 nm, its reduction kinetics changed with conversion, showing two kinetic compensation effects at lower and higher NiO conversion levels. It is believed that the migration of H radicals from H_2 dissociation sites towards the Ni-NiO boundary significantly influenced the reduction kinetics at lower (5 – 30%) levels of NiO conversion. On the other hand, at higher (50 – 90%) NiO conversion levels, the movement and re-arrangement of H atoms inside such bulk Ni/NiO solid could be an important aspect of the reduction kinetics.

4.1 Introduction

The reduction of nickel oxide by hydrogen (4.1) is an important reaction from both fundamental and application points of view. Understanding the reduction of nickel oxide is an important part in the process to understand catalytic reactions taking place via a redox cycle mechanism over a nickel-based catalyst. In industrial practice, nickel catalysts are often manufactured and delivered to a chemical plant in the form of nickel oxides which are not necessarily catalytically-ready for the reaction. Reduction at elevated temperature, for example, by using hydrogen is often required as the final catalyst activation step [1]:

$$NiO\ (s) + H_2\ (g) = Ni\ (s) + H_2O\ (g) \qquad (4.1)$$

Extensive studies [2-26] have been conducted on this reaction using various techniques and over a wide variety of particle sizes, shapes and forms. However, the kinetics and mechanism of reduction are still unclear. Voluminous disagreements exist in the literature, with the reported values of activation energy varying considerably from as low as ~0 kJ mol^{-1} to as high as >200 kJ mol^{-1} [4-13, 17-21]. In some studies [14-16], activation energy was, in fact, reported to vary with NiO conversion.

The consideration of chemical reactions and the diffusion of molecules [4, 6] alone cannot fully explain the discrepancies outlined above. The complicated (i.e. non-monotonic) relationships between reaction rate and temperature observed in the absence of significant mass transfer resistance for molecules [3, 19] provide evidence that the reaction between solid NiO and gaseous H_2 is more complicated than the traditional view of gas-solid reactions [27], which only takes into consideration the chemical reactions and the mass transfer of molecules (reactants and products). It may then be necessary to consider the migration of radicals on the catalyst surface as well as the mass transfer of these radicals through a solid bulk in order to understand the gas-solid NiO reduction.

The fates and roles of radicals generated on catalyst surface can have significant influences in determining the overall kinetics and reaction pathways in the gas-solid catalytic reactions [28-32]. In the reduction of NiO with H_2, the dissociation of H_2 on the particle surface is a pre-requisite, resulting in the formation of H radicals that then participate in the removal of oxygen from NiO [6]. Considering the very different particle sizes of NiO used in the various past studies, the failure to consider the H radical migration process including the distance of migration especially from the surface to the interior of an NiO crystallite in understanding the reduction kinetics, may have partly contributed to the considerable disagreements among the previous studies on this topic.

The study presented in this chapter was aimed at investigating the possible importance of H radical migration to the kinetics of NiO reduction. It has been considered that the crystallite size is an important factor determining the surface-to-volume ratio of the atoms and thus the nature of H migration (i.e. surface-dominant versus bulk-dominant) in the reduction of NiO. By varying the size of NiO crystallite in the NiO samples, some insights into the importance of H radical migration and the effects of NiO crystallite size on the kinetics and mechanism of NiO reduction with H_2 were successfully gained.

4.2 Experimental

Two types of nickel oxide were used in this study. The first one was the unsupported nano-sized NiO, supplied by Nanostructured and Amorphous Inc. (USA). The second one was the silica-supported NiO (60 wt% NiO), obtained from Sigma-Aldrich. Before being used in the experiments, the samples were thermally treated inside a quartz fluidised-bed reactor under the flow of argon at 350 °C for 45 mins to volatilise moisture and some potential impurities on their surface introduced during their preparation. The observation by transmission electron microscopy (TEM) confirmed that the physical sizes of unsupported NiO were in the range of 5 – 10 nm. The calculation using the Debye-Scherer equation based on the X-ray

diffraction (XRD) peaks showed that the average NiO crystallite size was 3.3 nm. For the supported NiO, the particle sizes of the silica support were in the range of 150 – 250 μm and the XRD-derived average crystallite size of NiO was 55 nm. The BET surface area, pore volume and pore width of NiO/SiO_2, as determined by Micromeritics Tristar 3000, was 143 $m^2\ g^{-1}$, 0.29 ml g^{-1} and 8.41 nm, respectively.

The reduction of NiO samples was carried out in a thermogravimetric analysis (TGA) unit described in 2.4. In an experiment, NiO sample was loaded into a platinum sample pan (5.4 mm ID and 2.0 mm height) and the particles were well spread into a very thin layer inside the pan. The amount of sample used in each experiment was ~5.5 mg for the unsupported nano NiO and ~9.2 mg (5.5 mg NiO + 3.7 mg SiO_2) for the silica-supported NiO. The NiO sample was firstly heated at a heating rate of 10 °C min^{-1} inside the TGA under a flow of argon (99.999% purity) at 100 ml min^{-1} from ambient temperature to the required isothermal temperature. Once the set temperature was reached, the hydrogen-argon gas mixture (60% H_2) at a flow rate of 20 ml min^{-1} was introduced into the TGA through a separate gas inlet to mix with the argon flow to give a total flow rate of 120 ml min^{-1} and 10% hydrogen concentration as the sample's reducing gas.

For each type of NiO, the isothermal reduction was studied separately at six different temperatures within the range of 500 to 600 °C. The TGA data in each experiment were recorded at 0.25 s intervals. The actual total weight loss in each experiment was found to vary less than 2% from the theoretical (stoichiometric) total weight loss estimation. Using the differential weight loss (d*W*/d*t*) data obtained from the TGA instrument, the specific reducibility of NiO, i.e. the rate of reduction per unit mass of the sample (excluding the weight of silica), R_x, (min^{-1}) at any instant was calculated using the following equation:

$$R_x = -\frac{1}{W} \cdot \frac{dW}{dt} \tag{4.2}$$

where W (mg) is the mass of the sample (excluding silica) at any time t. At a given conversion level and under a constant H_2 partial pressure, the above equation can be expressed as:

$$R_x = A\exp\left(-\frac{E_a}{RT}\right) \tag{4.3}$$

where A = pre-exponential factor (min^{-1}), includes a function of H_2 partial pressure and a sum of many conversion-dependent factors relating to solid NiO which are all constants at a given conversion level and a constant H_2 partial pressure, E_a = activation energy (J mol^{-1}), R = gas constant (J K^{-1} mol^{-1}) and T = temperature (K).

The Arrhenius plots of ln (R_x) versus 1/T were then used to obtain kinetic parameters of the NiO reduction at different conversion levels. Here, the conversion of NiO was calculated using the following equation:

$$\text{NiO conversion (\%)} = \frac{W_i - W}{W_i - W_f} \times 100 \qquad (4.4)$$

In above equation (4.4), W_i and W_f are the initial and final mass of the sample, respectively. Straight Arrhenius lines were obtained within the conversion levels of 5 to 90%, confirming the broad suitability of the kinetic equations derived above for use in this study.

4.3 Results and discussion

4.3.1 Key observations in the reduction of supported and unsupported NiO nanoparticles with H_2

Fig. 4.1 shows the isothermal TGA curves for the reduction of silica-supported NiO and unsupported NiO nanoparticles with 10% hydrogen (in argon) at various isothermal temperatures. It is important to note that zero minute in the figure refers to the time when H_2 was introduced into the TGA after the sample had achieved the required temperature.

The data in Fig. 4.1 suggest that the reduction of supported NiO was slower than the reduction of unsupported NiO. At 500 °C, for example, the unsupported NiO achieved its complete reduction around 1.2 min, whereas only 76% of the silica-supported NiO was reduced during the same period of time. The shapes of the curves in Fig. 4.1 also indicate that the reductions of the two types of NiO were significantly

different. Based on information available in the literatures, this difference could be due to many potential factors. The possible contributions of those factors towards the results obtained in this study have been critically assessed and are discussed in the following sub-sections.

4.3.1.1 Insignificance of nucleation

The initial formation of Ni crystallites from NiO can be divided into two stages: the initial slow dissociation of H_2 on NiO (and thus the induction) to form Ni^0 atoms and their subsequent nucleation to form Ni crystallites [33]. In the past [16, 20], the difficulty in reducing supported NiO (as compared to the unsupported bulk NiO) was attributed, among other factors, to the slow and difficult nucleation of a metallic phase on the very small NiO crystallites deposited on the support. It was argued that the nickel nuclei could not easily form on the layers which are too thin [16, 20]. The same hypothesis, however, is not valid to explain the lower reduction rates observed with the supported NiO in this study. This is because, in this study, the NiO crystallite size for the supported NiO (55 nm) was much bigger than the crystal size of the unsupported NiO (3.3 nm) while the former was reduced slower than the latter.

The insignificance of nucleation can be seen from a closer examination of the data in Fig. 4.1. There was always an induction period before a steady decrease in the sample's weight begun. Although the induction period for the silica-supported NiO was shorter, the total length of reduction, however, was longer than the unsupported NiO. While the reduction curves for the unsupported NiO (Fig. 4.1b) do not show a significant decrease in the rate of weight reduction after the induction period up to the end of reduction, the shape of NiO/SiO_2 reduction curves (Fig. 4.1a), on the contrary, clearly indicates that the weight reduction rate decreased significantly with increasing NiO conversion. The results explained above indicate that the reduction for the silica-supported NiO in this study cannot be attributed to the possible difficulty of nucleation because if nucleation was a limiting factor in the reduction of NiO/SiO_2, a more profound effect should have been seen on its induction length. Instead, the results of this study intimate that a shorter induction length was followed by slower reduction for NiO/SiO_2 than the unsupported NiO.

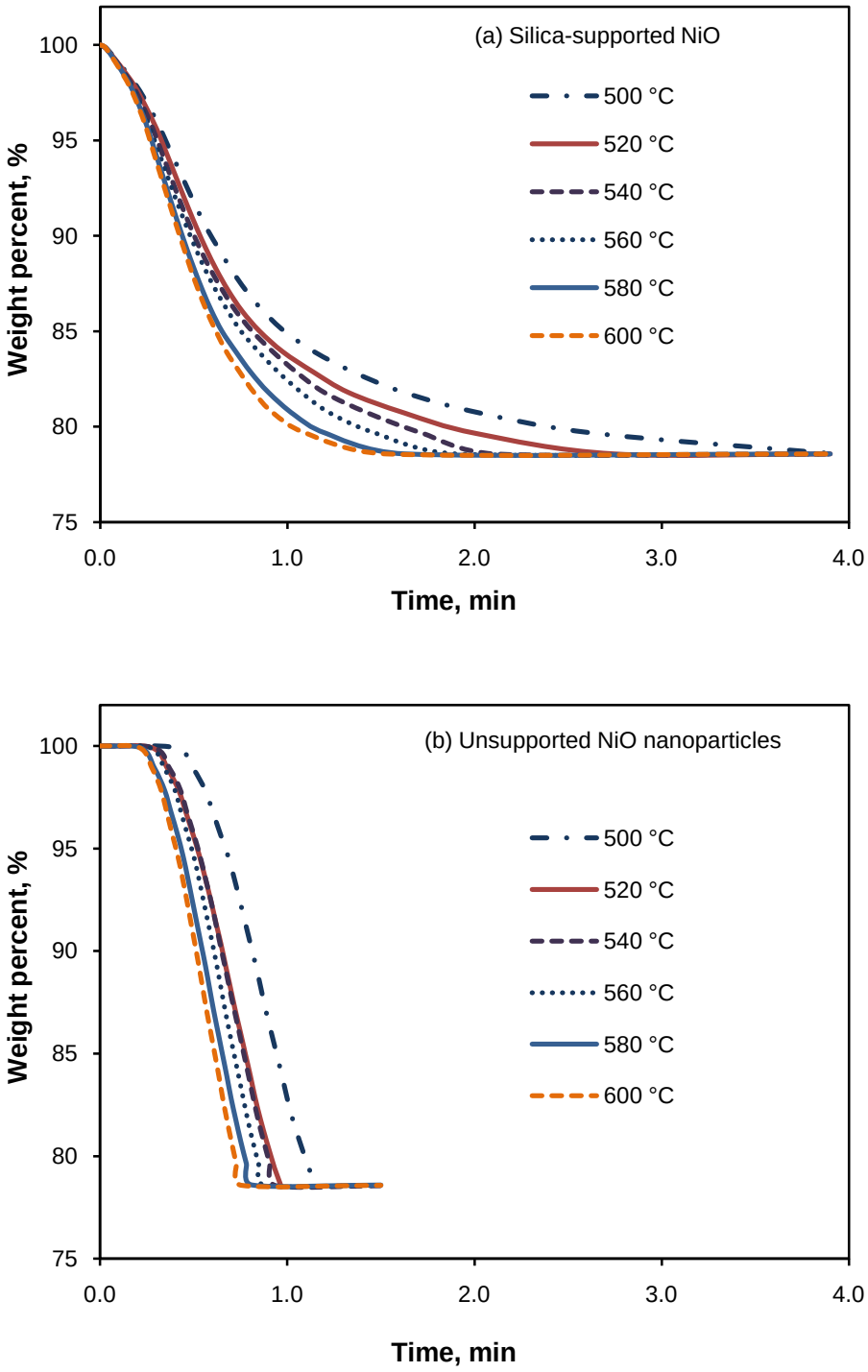

Fig. 4.1 Reduction profiles of the silica-supported NiO (a) and the unsupported NiO nanoparticles.

4.3.1.2 Absence of dominating mass transfer resistance for molecules

To examine the possible presence of a strong resistance for the diffusion of molecules in the reduction of silica-supported NiO with H_2, the NiO/SiO_2 catalyst particles were ground from the original sizes of around 150 – 250 µm to the new size of less than 25 µm. The new (<25 µm) NiO/SiO_2 particles were then reduced under the same conditions as those for the original 150 – 250 µm particles. The TGA curve for the reduction of ground NiO/SiO_2 at 560 °C is compared with the corresponding TGA curves for the reduction of original NiO/SiO_2 and unsupported NiO at the same temperature (Fig. 4.2).

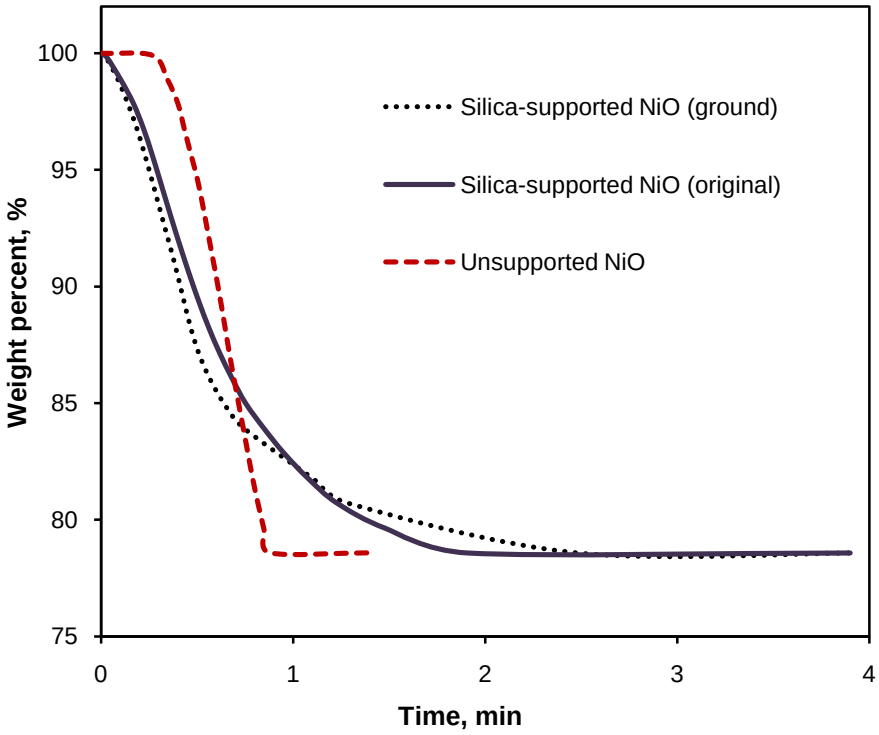

Fig. 4.2 TGA curve for the reduction of ground NiO/SiO_2 (<25 µm) with H_2 at 560 °C and its comparison with the original NiO/SiO_2 and the unsupported nano NiO particles.

It was found that the rate and the TGA curve shape of reduction of finely ground NiO/SiO_2 did not differ substantially from those of the original NiO/SiO_2 despite of the drastic reduction of the NiO/SiO_2 particle size. This implies that the consideration of molecular diffusion of H_2 inside the pore structures of silica cannot solely account

for the obvious difference between the reduction of silica-supported NiO and the unsupported NiO (Fig. 4.1). This examination also indirectly ruled out the possible retardation effect of H_2O [6, 16] in causing a big difference between the reduction of supported and unsupported NiO in this study. This is because the retarding effect of water is largely associated with the difficulty in the removal of water vapour by means of molecular diffusion out of the pores.

Further insights into the reduction kinetics can be gained by comparing the activation energies for the supported and unsupported NiO. As is shown in Fig. 4.3, the plots of E_a versus NiO conversion for the supported and unsupported NiO exhibit distinctively different trends. Activation energy for the reduction of unsupported NiO nanoparticles with hydrogen remains unchanged within the experimental errors almost throughout the whole period of reduction (up to 85% conversion, also see below) and the values are close to the theoretical intrinsic value for the dissociation of H_2 on Ni (4.6 – 9.6 kJ mol^{-1}) [34-36].

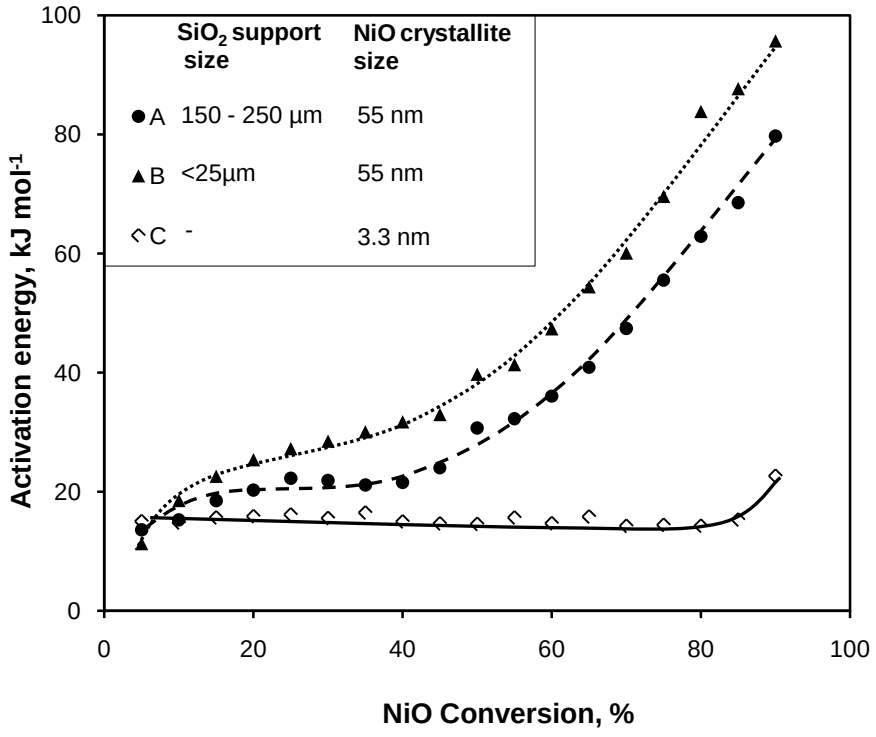

Fig. 4.3 Activation energy as a function of NiO conversion for the reduction of silica-supported NiO and unsupported NiO.

For the silica-supported NiO (regardless of the particle size of silica support), as can be seen in Fig. 3, the activation energy increases continuously with the progress of reduction. A similar increase has also been observed in a number of previous studies [14-16] but, hitherto, no plausible explanation is available. Although the data of the ground and original NiO/SiO_2 in Fig. 4.3 show some degree of pore diffusional resistance (decrease in E_a with the increase in the size of support), it is believed that the molecular diffusion was not the main rate-limiting step in the reduction of NiO/SiO_2 for the reasons outlined here. Firstly, the mass transfer resistance in the reduction of NiO/SiO_2 existed mainly due to the pore structure of the silica. During the NiO reduction, the silica was not consumed. Therefore, the pore structure and the distance of molecular diffusion and thus the value of E_a would not change with the degree of reduction. Secondly, even if there were some changes on the pore structure of silica, the value of the highest activation energy (at 90% conversion) should not be too far from twice ($E_T = 2E_{App}$) of the lowest activation energy (at 5% conversion). In other words, the molecular diffusion could not have possibly caused the activation energy to change from ~15 to ~95 kJ mol^{-1} and thus was not an important or rate-limiting step.

4.3.1.3 Absence of nickel silicate

Previous studies [16, 22, 24, 25] have suggested that one of the reasons for the difficult reducibility of silica-supported NiO was due to the possible formation of nickel silicate during the catalyst preparation and/or during the subsequent reduction.

To test the possible formation of nickel silicates and their role during catalyst reduction, the catalyst particles have been re-oxidised with air after its full reduction. The as-received NiO/SiO_2 samples as well as the re-oxidised samples were analysed using XRD. No evidence was found from the XRD of these samples to indicate the presence of nickel silicates. Realising that XRD may not detect amorphous nickel silicates, experiments were carried out to check the stoichiometry and kinetics of the reduction and re-oxidation of NiO/SiO_2 by subjecting NiO/SiO_2 to cycles of reduction, re-oxidation and re-reduction. To minimise/control the sintering process, the reduction was always carried out at 500 °C. It was found that the total weight loss

in the reduction of NiO/SiO_2 varied not more than 2% from the theoretical weight loss calculated based on stoichiometry. It was observed that the NiO/SiO_2 particles always regained their weight to within ±2% of the original weight during oxidation. Considering the difficulties [16, 22] for nickel silicates to undergo reduction and re-oxidation within a reasonable period of time under current conditions, the data in Fig. 4.4a do not provide any evidence that nickel silicates were ever formed.

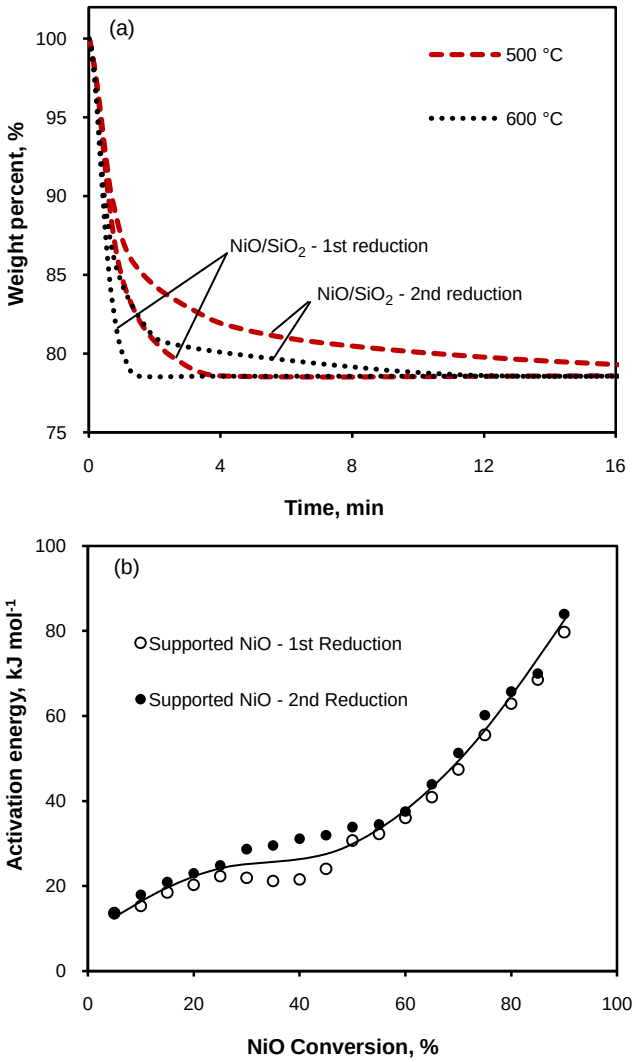

Fig. 4.4 The plot of weight percentage versus time for the first and second reduction of silica supported NiO at 500 and 600 °C (a) together with the plots of activation energy versus NiO conversion (b).

The TGA curves and the plots of E_a versus NiO conversion for the second reduction of NiO/SiO_2 are compared with those of the first reduction in Fig. 4.4. There were decreases in the reduction rate (Fig. 4.4a) from the first to the second reduction of NiO/SiO_2. However, the activation energies of reduction at all conversion levels did not vary to a significant extent from the first reduction (Fig. 4b). From the kinetic point of view, if nickel silicates were formed, the activation energies for the first and second reduction would be significantly different if the nickel silicates were reducible under current experimental conditions. While the hypothesis that the nickel silicates were completely irreducible (i.e. acting as inert materials) may explain why the activation energies remained unchanged (Fig. 4.4b) from the first to the second reduction, this hypothesis would mean that the total weight loss in the second reduction would be smaller than that during the first reduction, which contradicts the data in Fig. 4.4a. Therefore, the stoichiometric (Fig. 4.4a) and kinetic (Fig. 4.4b) data clearly indicate that the formation of nickel silicates did not take place under the experimental conditions used.

4.3.2 Evidence for the importance of NiO crystallite size for its reduction

The only clear distinction between the two types of NiO used, other than the presence/absence of silica support, was their average sizes of NiO crystallites. In order to examine the potential effect of crystallite size, multiple reduction/oxidation cycles were carried out on the unsupported NiO. After the first reduction and re-oxidation at 500 °C, the average size of NiO crystals increased from 3.3 to 20 nm. After the second reduction and re-oxidation at the same temperature, the average crystal size grew to 24 nm.

The TGA curves for the first, second and third reduction of unsupported NiO nanoparticles with hydrogen at 500 °C are compared in Fig. 4.5a. Surprisingly, the curves for the second and third reduction of unsupported NiO differ significantly from the first reduction. Unlike the first reduction, the TGA curves for the second and third reduction of unsupported NiO show a similar pattern to those of the reduction of silica-supported NiO (Figs. 4.1a & 4.4a), suggesting that there was a decrease in the reduction rate after a certain level of NiO conversion. Although the

decrease in surface area due to the sintering effect can explain the changes in the reaction rate, the same reason cannot explain why there are changes in the activation energy of reduction (see below).

Even more interestingly, the plots of E_a versus NiO conversion (Fig. 4.5b) for the second and third reduction of unsupported NiO also deviate completely from the trend of the first reduction and instead display a similar pattern to the plots for the reduction silica-supported NiO, i.e., a continuous increase in E_a with the progress of reduction (Fig. 4.4b). This observation provides additional indirect evidence that the physical and chemical effects of silica were not directly responsible for the increase in E_a as observed in the reduction of silica-supported NiO in this study.

We believe that the main reason for the changes in the behaviour during the consecutive reduction of the unsupported NiO nanoparticles was due to the related physical changes (other than surface area) associated with the change in the crystallite size. At 3.3 nm (i.e. at the beginning of the first reduction), about 60 – 70% atoms of the crystal are exposed to or on the surface, while above 20 nm, the atoms on the surface represent less than 10% of the crystal [37]. The changes in the surface-to-bulk ratio with the average crystallite size of NiO may explain the reason for the changes in their reduction behaviour with average crystallite size, as will be discussed next in detail.

4.3.3 Kinetic compensation effects in the reduction of NiO

The Arrhenius plots for the reduction of unsupported NiO are shown in Fig. 4.6. For the first reduction (crystallite size = 3.3. nm), the data in Figs. 4.6a and 4.6c indicate that the Arrhenius plots (except for 90% conversion, see below) do not show any tendency to converge. The plot of ln$A$ versus E_a, normally termed as "Constable plot" in Fig. 4.6e, show a vertical line, indicating the absence of any kinetic compensation effect in the reduction of the very fine NiO particles. The changes in ln$A$ with NiO conversion are a result of the increases in the number of active sites (neighbouring Ni atoms) for the dissociation of reductant molecules. However, the nature of the active sites remains unchanged to give a constant E_a.

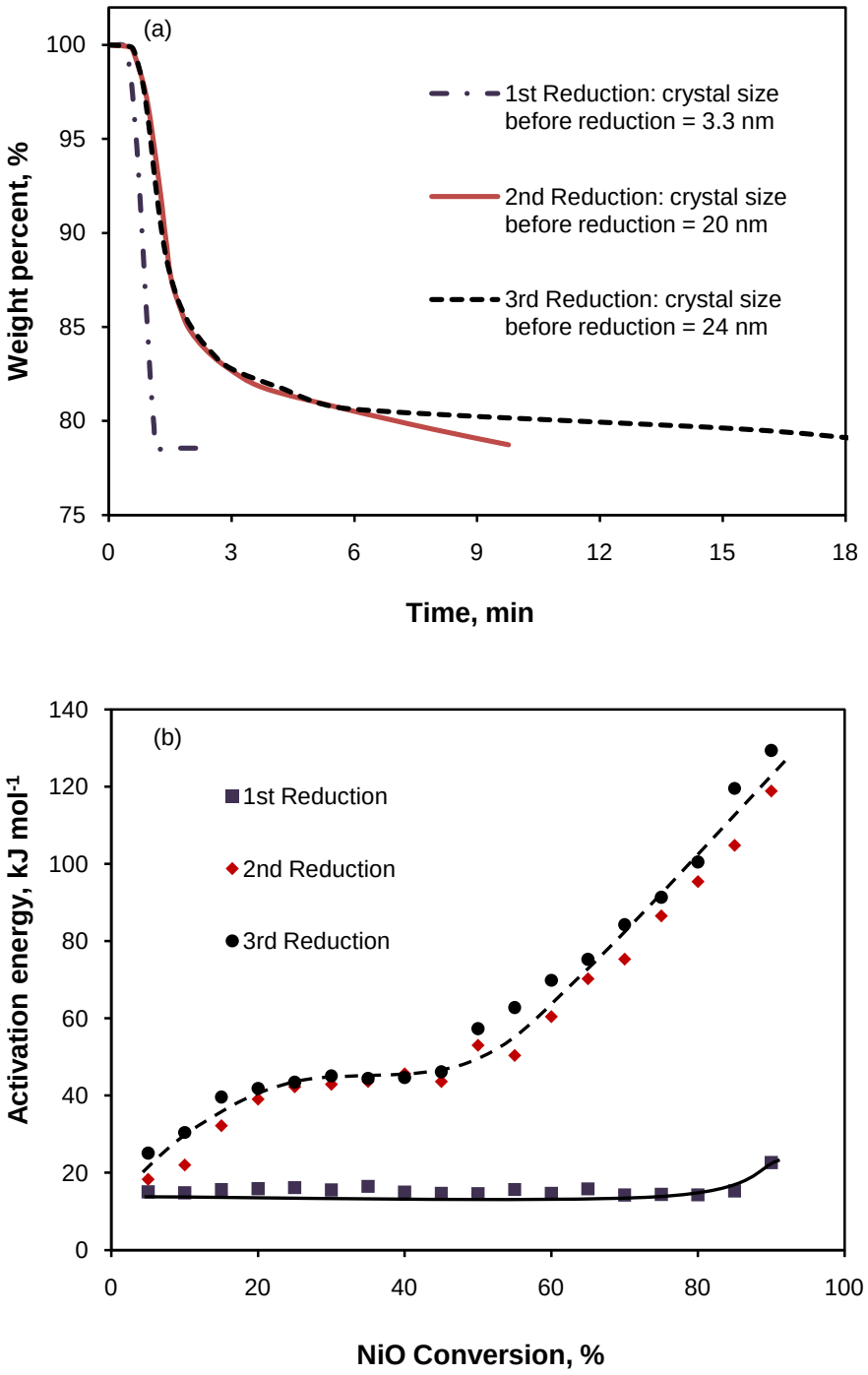

Fig. 4.5 TGA curve for the first, second and third reduction of unsupported NiO nanoparticles at 500 °C (a) and their corresponding plot of E_a versus NiO conversion.

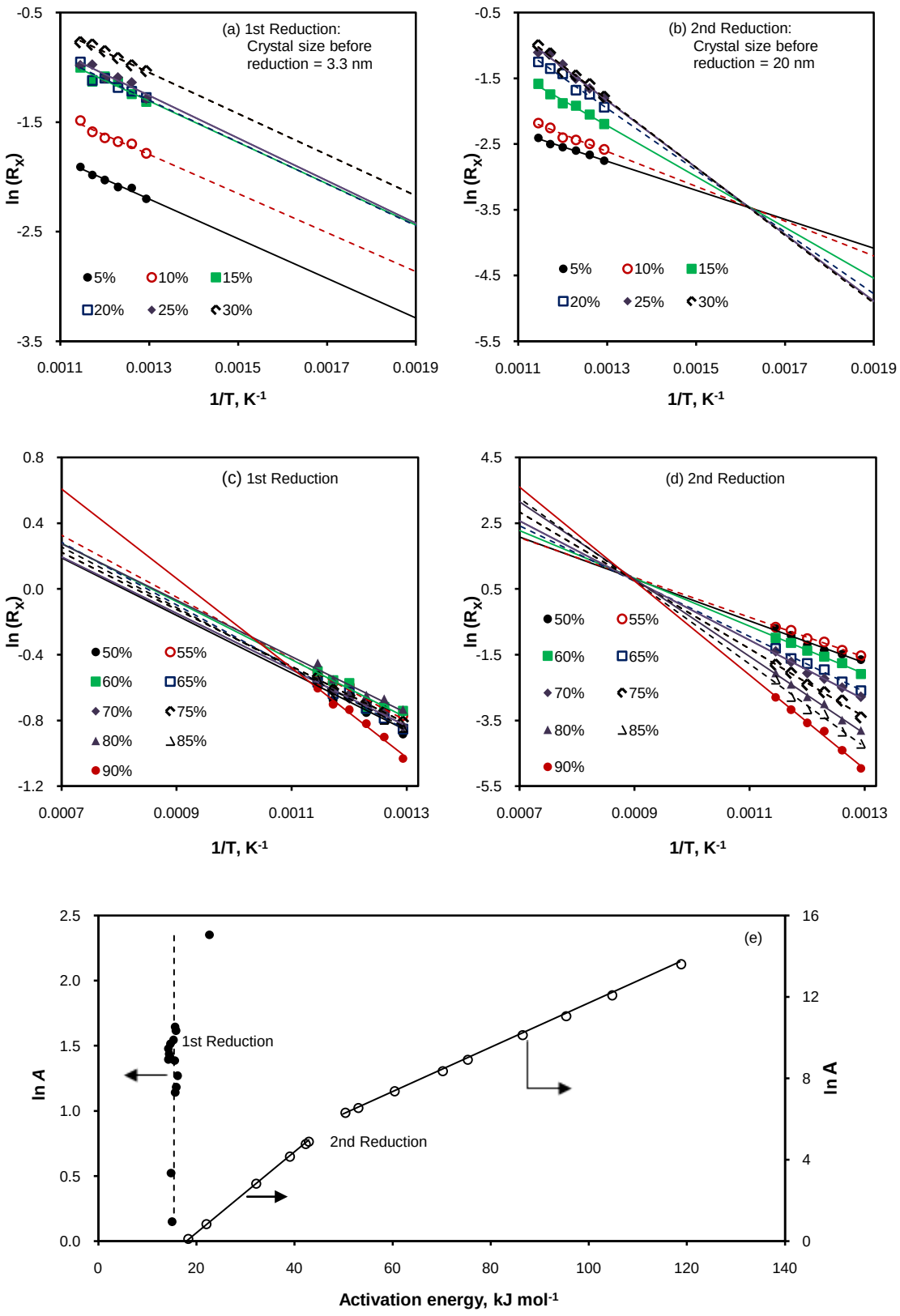

Fig. 4.6 Arrhenius plots for the first (a & c) and second (b & d) reduction of unsupported nano NiO particles and their corresponding Constable plots (e).

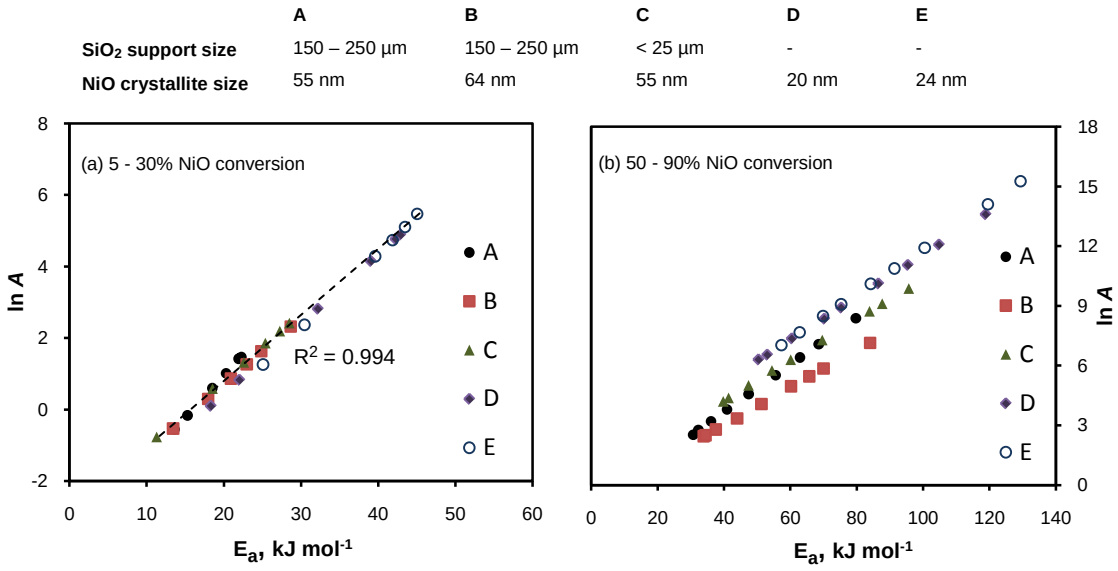

Fig. 4.7 ln *A* versus E_a at lower (a) and higher (b) conversion levels for the reduction of NiO with crystallite size ≥20 nm.

The Arrhenius plots for the second reduction of unsupported NiO (after the crystallite size grew to 20 nm) surprisingly converged to two different points (Figs. 4.6b and d), depending on the conversion levels. The corresponding Constable plots also showed two different slopes, indicating the existence of kinetic compensation effects [38-40] with isokinetic temperatures [i.e. the temperatures corresponding to the two converging (1/*T*) values for the Arrhenius plots]: ~340 °C at lower NiO conversions (5 – 30%) and ~860 °C at higher conversion levels (50 – 90%). Similar observations were also made for the reduction of all other NiO samples with crystallite size bigger than 20 nm (supported or unsupported). Apparently, there exist the kinetic compensation effects in the reduction of bigger crystallite NiO. Taken together, these data indicate that the reduction of NiO follows two different mechanisms for NiO crystallite sizes below and above ~20 nm.

Fig. 4.7 plots the values of ln*A* and E_a from the reduction of supported and unsupported NiO samples with crystallite sizes of 20 nm and bigger. All datum points at low conversion levels (e.g. 5 – 30% in Fig. 4.7a) fall into a single straight

line with R^2 value close to one. At higher NiO conversion levels (e.g. 50-90% in Fig. 4.7b), the ln*A* versus E_a plots show individual straight lines. These data indicate that, for NiO crystallite sizes bigger than ~20nm, the mechanism operative at higher conversion levels is much more sensitive to the particle characteristics than the mechanism operative at lower conversion levels.

4.3.4 Further discussion of the mechanisms of NiO reduction with H_2

As is shown in Fig. 4.8, the reduction of metal oxide always proceeds through the formation of metallic nuclei on the particle surface [6, 33, 41]. It was explained earlier (Section 4.3.1) that the dissociation of H_2 to produce H on the surface, which is an intermediate required for the reduction of NiO, is more favourable on two neighbouring Ni atoms rather than on the adjacent Ni and O atoms [42]. Upon their formation, the metallic nuclei would coalesce (sinter/agglomerate) to form larger metallic islands, which would provide more venues for the dissociation of H_2 to form atomic hydrogen radicals. From the hydrogen dissociation sites of the island, hydrogen radicals would have to migrate to the Ni-NiO boundary to react with oxygen.

Depending on the size of island, the H-radical migration would require a series of Ni-H breaking and re-forming steps before the radicals can reach the boundary. For a very small particle, the whole particle surface can be instantaneously covered by the metallic layer without requiring a significant growth of islands. The islands themselves, indeed, are big enough to occupy the whole surface of the very fine particles. The reduction rate would only increase with the size of the islands (i.e. the number of sites for H_2 dissociation).

For a big particle with significant atoms in the interior (e.g. >20 nm NiO crystallite sizes in this study), it might take quite some time for the growth of island to cover the whole particle's surface. When the size of the island grows, the number of hydrogen dissociation sites (neighbouring Ni atoms) would automatically be increased. However, when the island is bigger, H radical would need to migrate from its dissociation site over a longer distance in order to reach the Ni-NiO boundary.

This surface diffusion/migration is distinctively different from the diffusion in the gas phase. While the gas-phase diffusion is completely physical process, the surface migration of H radicals requires a series of individual Ni-H bond breaking and bond re-forming steps. Although the activation energy for an individual step is always the same, the overall activation energy for the series of steps could result in a big value of activation energy.

Therefore, the increases in the reaction rate due to the increases in the number of hydrogen dissociation sites as a result of the increases in island size are well "compensated" for by the corresponding decreases in reaction rate due to the increases in the number of H radical migration steps. This may plausibly be the reason for the existence of a kinetic compensation effect at lower NiO conversion levels (5 – 30%) observed in this study.

Once the surface has been covered completely by the metal product, the Ni-NiO boundary would then progressively advance inwards. The further reduction of NiO would not only require the migration of radicals to the Ni-NiO boundary on the surface, but also involve the diffusion, i.e. movement and re-arrangements of atoms, possibly in multi-steps, in the interior of the particle. The solid-state diffusion of atoms requires very high activation energy [43]. The number of steps of diffusion in the solid state would appear to increase with NiO conversion, resulting in continuous increases in the activation energy. This explains why there was a significant increase in the value of activation energy beyond 50% conversion levels in the reduction of NiO with a crystallite size of 20 nm and bigger. As is shown in Figs. 4.6 and 4.7, at high NiO conversion levels, the increases in the activation energy increasingly overweigh the increases in the site for H_2 dissociation and the Ni-NiO interface, resulting in changes in the slope of the Constable plots.

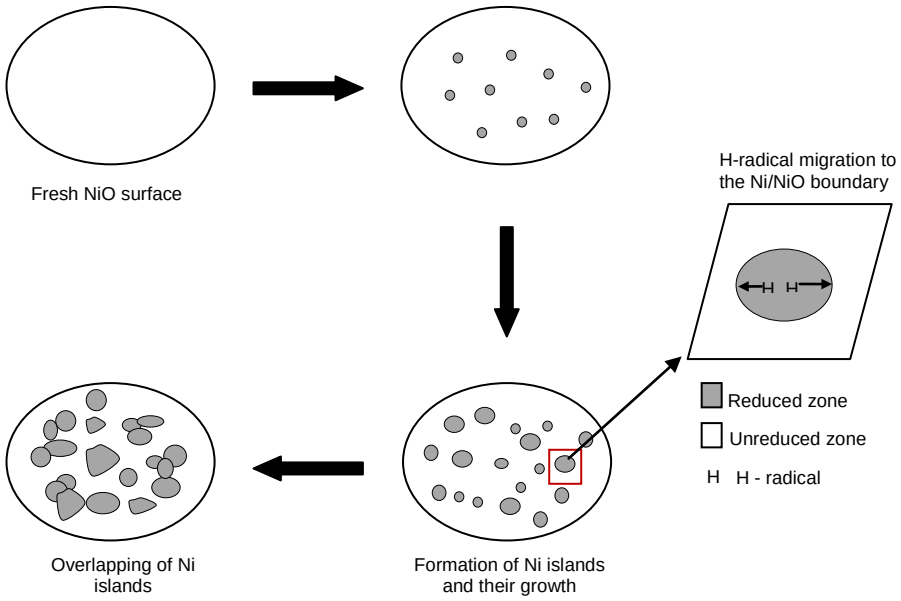

Fig. 4.8 Nucleation and nuclei growth during the reduction.

4.4 Conclusions

The results of this study have shown that the reduction of unsupported nano-sized NiO particles (<10 nm) with hydrogen can be quite different from the reduction of silica-supported NiO. The average crystallite NiO size grows significantly during the reduction of unsupported NiO nanoparticles, diminishing the difference between their reduction and that of NiO/SiO_2. While the reduction of nano NiO particles of 3.3 nm average crystal size does not show any kinetic compensation effect, the reduction of NiO with crystal sizes bigger than about 20 nm show strong kinetic compensation effects with two isokinetic temperatures for the low and high NiO conversion levels. The data obtained from this study provide strong evidence for the importance of H radical migration/diffusion both on the surface and inside the NiO crystals/particles. For a small NiO crystal/particle, the key kinetic step in its reduction is the dissociation of H_2 on the surface. For a big (>20 nm) crystallite/particle containing significant portion of its atoms in the interior, the movement and re-arrangement of atoms in the interior can make very significant contribution to the overall activation energies.

4.5 References

[1] B. Delmon, From the precursor to the final catalyst, in: G. Ertl, H. Knozinger, J. Weitkamp, (Eds.), Preparation of Solid Catalysts, Wiley-VCH, Weinheim,1999, pp. 541-589.

[2] T. Hidayat, M.A. Rhamdhani, E. Jak, P.C. Hayes, On the relationships between the kinetics and mechanisms of gaseous hydrogen reduction of solid nickel oxide, Metall. Mater. Trans. B 40 (2009) 474-489.

[3] T. Hidayat, M.A. Rhamdhani, E. Jak, P.C. Hayes, The kinetics of reduction of dense synthetic nickel oxide in H_2-N_2 and H_2-H_2O atmospheres, Metall. Mater. Trans. B 40 (2009) 1-16.

[4] P. Erri, A. Varma, Diffusional effects in nickel oxide reduction kinetics, Ind. Eng. Chem. Res. 48 (2009) 4-6.

[5] J.T. Richardson, M. Lei, B. Turk, K. Forster, M.V. Twigg, Reduction of model steam reforming catalysts: NiO/α-Al_2O_3, Appl. Catal. A 110 (1994) 217-237.

[6] J.T. Richardson, R. Scates, M.V. Twigg, X-ray diffraction study of nickel oxide reduction by hydrogen, Appl. Catal. A 246 (2003) 137-150.

[7] J. Szekely, J.W. Evans, A structural model for gas-solid reactions with a moving boundary - II : The effect of grain size, porosity and temperature on the reaction of porous pellets, Chem. Eng. Sci. 26 (1971) 1901-1913.

[8] J. Szekely, C. Lin, H. Sohn, A structural model for gas-solid reactions with a moving boundary - V: An experimental study of the reduction of porous nickel-oxide pellets with hydrogen, Chem. Eng. Sci. 28 (1973) 1975-1989.

[9] J. Bandrowski, C.R. Bickling, K.H. Yang, O.A. Hougen, Kinetics of the reduction of nickel oxide by hydrogen, Chem. Eng. Sci. 17 (1962) 379-390.

[10] B. Delmon, A. Roman, Kinetic study of the reduction of nickel oxide near its antiferromagnetic-paramagnetic transition. Influence of the magnetic structure

of the reactant on the kinetics of nucleus formation on its surface, J. Chem. Soc., Faraday Trans. 1 69 (1973) 941-948.

[11] G. Parravano, The Reduction of nickel oxide by hydrogen, J. Am. Chem. Soc. 74 (1952) 1194-1198.

[12] H. Charcosset, R. Frety, G. Labbe, Y. Trambouze, Increase of the rate of reduction of NiO by H_2, due to pretreatment with CO or NH_3, J. Catal. 35 (1974) 92-99.

[13] F. Chiesa, M. Rigaud, La reduction de l'oxyde de nickel par l'hydrogene, Can. J. Chem. Eng. 49 (1971) 617-620.

[14] X.G. Wang, Y.D. Wei, J. Zhang, H.Y. Xu, W.Z. Li, On the reduction kinetics of coprecipitated NiO-Al_2O_3 and NiO-La_2O_3-Al_2O_3 catalysts, React. Kinet. Catal. Lett. 89 (2006) 97-104.

[15] A. Sannomiya, K. Ichimura, M. Yano, Y. Harano, Reduction of supported nickel oxides and their interactions with supports, Kag. Kog. Ronbunshu 10 (1984) 158-165.

[16] J.W.E. Coenen, Reduction of silica-supported nickel catalysts, Stud. Surf. Sci. Catal. 3 (1979) 89-111.

[17] J. Evans, S. Song, C. Leonsucre, Kinetics of nickel-oxide reduction by hydrogen - measurements in a fluidized-bed and in a gravimetric apparatus, Metall. Trans. B 7 (1976) 55-65.

[18] G. Plascencia, T. Utigard, The reduction of Tokyo and Sinter 75 nickel oxides with hydrogen, Chem. Eng. Sci. 64 (2009) 3879 - 3888.

[19] T.A. Utigard, M. Wu, G. Plascencia, T. Marin, Reduction kinetics of Goro nickel oxide using hydrogen, Chem. Eng. Sci. 60 (2005) 2061-2068.

[20] A. Roman, B. Delmon, Promoter and carrier effects in reduction of NiO-SiO_2, J. Catal. 30 (1973) 333-342.

[21] F. Medina, P. Salagre, J.L.G. Fierro, J.E. Sueiras, NiO Reducibilities: structural and catalytic properties of their pure and potassium-doped reduced forms, J. Catal. 142 (1993) 392-405.

[22] J.W.E. Coenen, Characterization of the standard nickel/silica catalyst EuroNi-1: II. chemical aspects: precipitation, reduction and chemical analysis, Appl. Catal. 54 (1989) 65-78.

[23] J. Zieliński, Morphology of nickel/alumina catalysts, J. Catal. 76 (1982) 157-163.

[24] J. Zieliński, Reductibility of silica supported nickel oxide, Catal. Lett. 31 (1995) 47-56.

[25] O. Clause, L. Bonneviot, M. Che, Effect of the preparation method on the thermal stability of silica-supported nickel oxide as studied by EXAFS and TPR techniques, J. Catal. 138 (1992) 195-205.

[26] J.T. Richardson, M.V. Twigg, Reduction of impregnated NiO/α-Al_2O_3 association of Al^{3+} ions with NiO, Appl. Catal. A 167 (1998) 57-64.

[27] J. Szekely, J.W. Evans, H.Y. Sohn, Gas-Solid Reactions, Academic Press, New York, 1976.

[28] E.B.H. Quah, C.-Z. Li, Effects of radical desorption on catalyst activity and coke formation during the catalytic pyrolysis and oxidation of light alkanes, Appl. Catal. A 250 (2003) 83-94.

[29] E.B.H. Quah, C.-Z. Li, Roles of desorbed radicals and reaction products during the oxidation of methane using a nickel mesh catalyst, Appl. Catal. A 258 (2004) 63-71.

[30] E.B.H. Quah, C.-Z. Li, Pyrolysis of liquefied petroleum gas assisted by radicals desorbed from mesh catalyst surface, Int. J. Chem. Kinet. 35 (2003) 637-646.

[31] E.B.H. Quah, J.F. Mathews, C.-Z. Li, Interinfluence between reactions on the catalyst surface and reactions in the gas phase during the catalytic oxidation of methane with air, J. Catal. 197 (2001) 315-323.

[32] W.J. Lee, C.-Z. Li, Coke formation and reaction pathways of catalyst-surface-generated radicals during the pyrolysis of ethane using Ni mesh catalyst, Appl. Catal. A 316 (2007) 90-99.

[33] Y. Koga, L.G. Harrison, Reactions of solids with gases other than oxygen, in: C.H. Bamford, C.F.H. Tipper, R.G. Compton, (Eds.), Comprehensive Chemical Kinetics, vol. 21, Elsevier, Amsterdam,1984, pp. 146-149.

[34] H. Yang, J.L. Whitten, Dissociative adsorption of H_2 on Ni(111), J. Chem. Phys. 98 (1993) 5039-5049.

[35] K.D. Rendulic, A. Winkler, H.P. Steinrück, The role of surface defects in the adsorption and desorption of hydrogen on Ni(111), Surf. Sci. 185 (1987) 469-478.

[36] S.M. Foiles, M.I. Baskes, C.F. Melius, M.S. Daw, Calculation of hydrogen dissociation pathways on nickel using the embedded atom method, J. Less-common Met. 130 (1987) 465-473.

[37] G. Palumbo, S.J. Thorpe, K.T. Aust, On the contribution of triple junctions to the structure and properties of nanocrystalline materials, Scripta Metall. Mater. 24 (1990) 1347-1350.

[38] N. Koga, A review of the mutual dependence of Arrhenius parameters evaluated by the thermoanalytical study of solid-state reactions: the kinetic compensation effect, Thermochim. Acta 244 (1994) 1-20.

[39] L. Liu, Q.X. Guo, Isokinetic relationship, isoequilibrium relationship, and enthalpy-entropy compensation, Chem. Rev. 101 (2001) 673-695.

[40] G.C. Bond, M.A. Keane, H. Kral, J.A. Lercher, Compensation phenomena in heterogeneous catalysis: general principles and a possible explanation, Catal. Rev. Sci. Eng. 42 (2000) 323-383.

[41] K.M. Ostyn, C.B. Carter, On the reduction of nickel oxide, Surf. Sci. 121 (1982) 360-374.

[42] J.A. Rodriguez, J.C. Hanson, A.I. Frenkel, J.Y. Kim, M. Perez, Experimental and theoretical studies on the reaction of H_2 with NiO: role of O vacancies and mechanism for oxide reduction, J. Am. Chem. Soc. 124 (2002) 346-354.

[43] S. Mrowec, Defects and diffusion in solids: an introduction, Elsevier, Amsterdam, 1980.

CHAPTER 5

NiO reduction with hydrogen and light hydrocarbons: contrast between silica-supported and unsupported NiO nanoparticles

Overview:

This study investigates the reduction of unsupported NiO nanoparticles and silica-supported NiO with different reducing gases (hydrogen, methane and ethane) in the temperature range of 500 to 600 °C. It was found that, in addition to the reaction and mass transfer of molecular species, the fates and activities of surface-formed radical species have to be considered in explaining the kinetics of nickel oxide reduction. It is believed that the desorption of hydrocarbon radicals from the particle surface has significantly slowed down the reduction of unsupported NiO nanoparticles. The ease with which a radical migrates from its dissociation site on a metallic island to the Ni-NiO surface boundary, on the other hand, is an important rate-limiting step in the reduction of silica-supported NiO.

5.1 Introduction

The study on metal oxide reduction by hydrogen or hydrocarbon gases is immensely important in the area of catalysis and metallurgy as well as in the development of green power generation technology via chemical-looping combustion. The reduction of metal oxide is an essential part of the overall reaction mechanisms if a catalytic reaction proceeds via a redox cycle mechanism. The successful selection of process conditions including the type of gaseous reductant (e.g. natural gas versus hydrogen) for the metallic ore reduction process [1] or the type of support for the chemical-looping combustion [2, 3] demands a deep knowledge of the reduction kinetics and mechanism. However, the present understanding on the metal oxide reduction, even for a simple system such as NiO reduction with H_2 [4-13], is still far from complete, due largely to a lack of detailed knowledge on the fates and activities of surface radicals.

During the reduction of metal oxide, radicals such as H (s) and/or C_xH_y (s) are formed as a result of the dissociation of reductant molecules on the solid surface [5, 14]. A past study has highlighted the effect of H radical mobility in the dissociation of hydrogen on Ni [15]. It was shown that, when H mobility is low, the recombination of H atoms occurs very easily and the net H_2 dissociation rate becomes small [15]. Meanwhile, a large body of evidence [16-25] has emerged to show that the radicals generated on the solid surface do not always, as is traditionally perceived, remain to react on the surface but can also leave the surface by desorbing into the gas phase. In many catalytic reactions, the desorption of radicals is responsible for accelerating reactions in the gas phase [16-20, 22] and influencing the formation of carbon materials on the catalyst surface [16, 20, 21]. The desorption of radicals, could also influence the observed overall rate of reduction, which has largely been ignored in the previous studies, giving apparently contradicting observations.

The understanding of the fates and activities of surface-generated radicals during the reduction of metal oxide is, therefore, crucial and requires special attention. Chapter 4 of this thesis reported the importance of H radical migration/diffusion both

on the surface and inside the particles in the reduction of NiO with H_2 [26]. Further extending the efforts made in Chapter 4 [26], this study investigates the reduction of supported and unsupported nickel oxide nanoparticles with different gaseous reductants (hydrogen, methane and ethane) that will have more types of radicals (H and C_xH_y) on the surface. Based on our experimental results, different surface-formed radical species and their influences on the kinetics of nickel oxide reduction will be discussed.

5.2 Experimental

Two types of nickel oxide were used in this study [26]: (1) the nano-unsupported NiO particles and (2) the silica-supported NiO (60 wt% NiO). The particle sizes of unsupported NiO as observed with TEM were in the range of 5 – 10 nm and the XRD-derived average NiO crystallite size was 3.3 nm. For the supported NiO, the particle sizes of the silica support were in the range of 150 – 250 μm with the BET surface area, pore volume and pore width of the support as 143 m2 g-1, 0.29 ml g-1 and 8.41 nm, respectively. Grinding the NiO/SiO2 particles to <25 μm did not result in any significant changes in the observed activation energy, indicating that the intra-particle mass transfer was not the rate-liming process under our experimental conditions. The XRD-derived average crystallite size of NiO in the support was 55 nm. The use of unsupported NiO nanoparticles (having virtually no pores) in this study was mainly to provide a base for comparison in order to evaluate the importance of pore structures in a supported porous catalyst to the reduction of NiO.

The gases used in this study were argon, hydrogen, methane and ethane, supplied by BOC and were 99.999% pure. The reduction of NiO samples was carried out using a thermogravimetric apparatus (TA SDT-Q600) with weighing sensitivity of 0.1 μg. The amount of sample used in every experiment was ~5.5 mg for the unsupported nano NiO and ~9.2 mg (5.5 mg NiO + 3.7 mg SiO_2) for the silica-supported NiO.

The TGA furnace, in which the NiO or NiO/SiO_2 particles were placed and well spread into a very thin layer inside a platinum sample pan, were firstly purged with argon gas flowing at 100 ml min^{-1}. The sample temperature was then raised at a heating rate of 10 °C min^{-1} from room temperature to the desired isothermal temperature. Once the set temperature was reached, the mixture of argon-reductant gas (40% argon) which was prepared using two external mass flow controllers was introduced into the TGA through a separate gas inlet to mix with the balance chamber purge gas (Ar) to provide total flow rate of 120 ml min^{-1} reducing gas (10% reductant in argon).

5.3 Results and discussion

5.3.1 Differences in the reduction of NiO with H_2, CH_4 and C_2H_6

The reduction of unsupported NiO nanoparticles with different gaseous reductants was carried out isothermally in the temperature range of 500 – 600 °C and the results are shown in Fig. 5.1. NiO conversion was calculated using the following equation:

$$\text{NiO conversion}\,(\%) = \frac{W_i - W}{W_i - W_f} \times 100 \qquad (5.1)$$

with W_i and W_f in the above equation represent the initial and final weight of the NiO, respectively. Here, final weight (W_f) is referred to the lowest weight of the samples achieved during the reduction, which was no less than 95% of the value expected based on the stoichiometry.

The results in Fig. 5.1 show that a period of induction always appears at the beginning of NiO reduction. Koga and Harrison [27] described the induction period as the initial stage of metal oxide reduction whereby a number of metallic nuclei are formed on the outer surface of metal oxide particles. The Ni^0 atoms merge to form larger Ni^0 islands which subsequently grow in size and become a landing base for the molecules of reducing gas to dissociate. The dissociation of gaseous molecules on the metallic surface is much easier than the dissociation on the oxide surface. For this

reason, the reduction rate was seen to accelerate shortly after the induction period (i.e. upon the formation of the metallic islands).

The kinetic parameters for the reduction of NiO were determined using the TGA data. In this study, we expressed the specific reducibility of NiO (R_x) as:

$$R_x = -\frac{1}{W} \cdot \frac{dW}{dt} = A \exp(-E_a / RT) \tag{5.2}$$

where dW/dt = differential weight loss obtained from the TGA, E_a = activation energy (J mol^{-1}), A = pre-exponential factor (min^{-1}), which includes a sum of many conversion-dependent factors that are constants at a given reductant partial pressure, R = gas constant (8.314 J K^{-1} mol^{-1}) and T = temperature (K).

By plotting ln (R_x) versus $1/T$ we then obtained the value of activation energy at a specified conversion level. As is shown in Figure 5.2 (also Figure 5.5, see below), good straight lines were obtained at low ($\leqslant$ 10%) and high ($\geqslant$70%) conversion levels, reflecting that our experimental conditions were suitable for deriving the kinetic parameters. The nonlinear lines for the middle conversion levels will be discussed below. The value of activation energy at different conversion levels for the reduction of unsupported NiO nanoparticles with three different gases are listed in Table 5.1.

As indicated in Table 5.1, at 5 and 10% NiO conversion, the activation energies for NiO reduction with CH_4 and C_2H_6 are 155 – 171 and 96 kJ mol^{-1}, respectively. These values are in good agreement with the values obtained from the theoretical studies about CH_4 and C_2H_6 dissociation on NiO [28, 29]. It is believed that, at this conversion level, the activation of reductant molecules mainly took place directly on the NiO surface. From 15% up to 65% conversion, the Arrhenius plots for the reduction of unsupported NiO nanoparticles with CH_4 and C_2H_6 were found to be non-linear.

The Arrhenius plots for the reduction with CH_4 are shown in Fig. 5.2. A mixed mechanism is believed to be operative within this conversion range where the activation of gaseous molecules occurred both on the oxide and on the metallic surfaces as the number and size of metallic island increased.

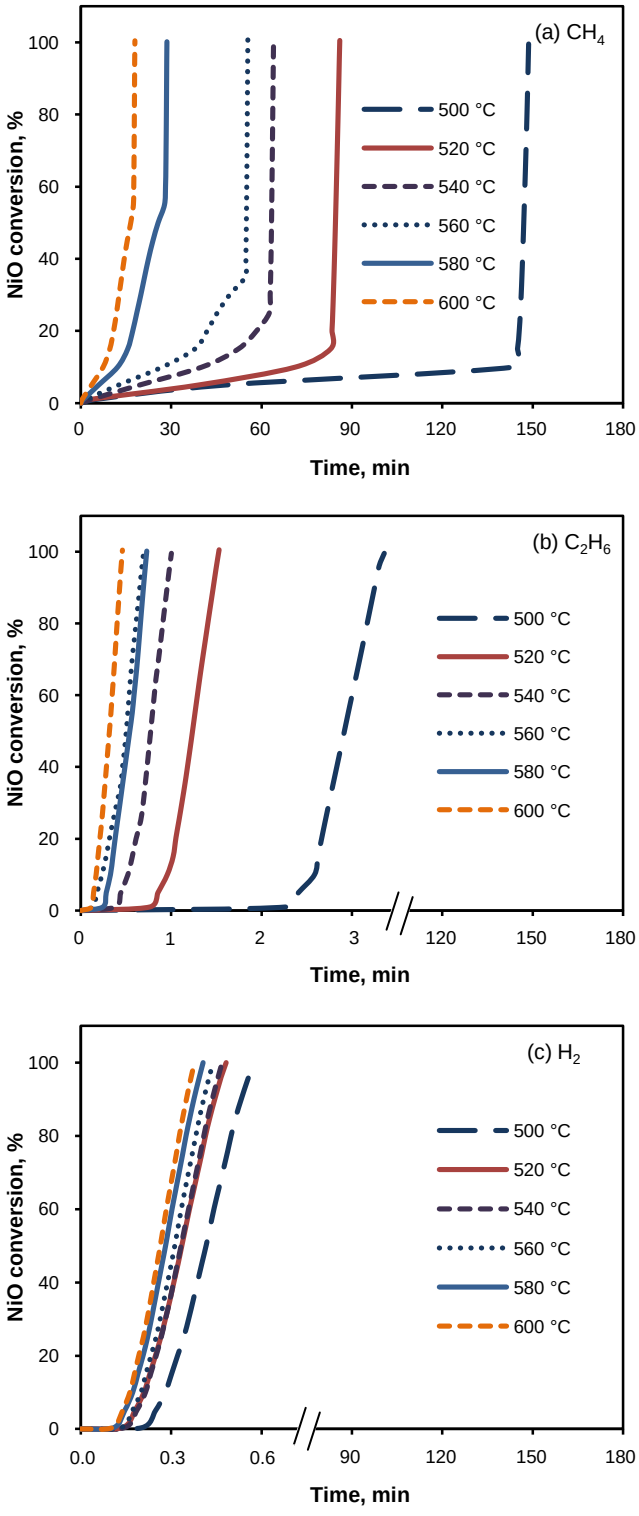

Fig. 5.1 NiO conversion as a function of time during the reduction of unsupported NiO nanoparticles with CH_4 (a), C_2H_6 (b) and H_2 (c) in TGA.

Table 5.1 The values of activation energy at different NiO conversion levels for the reduction of unsupported nano-sized NiO with methane, ethane and hydrogen.

Conversion, %	E_a for NiO reduction , kJ mol^{-1}		
	CH_4	C_2H_6	H_2
5	155.3	94.9	15.0
10	171.3	96.1	14.8
15			15.7
20			15.9
25	Arrhenius plots appeared to be non-linear	Arrhenius plots appeared to be non-linear	16.2
30			15.6
35			16.5
40			15.0
45			14.7
50			14.6
55			15.7
60			14.7
65			15.8
70	80.1	58.9	14.3
75	79.0	61.7	14.4
80	84.4	61.4	14.3
85	87.7	58.6	15.3
90	84.7	58.3	22.6

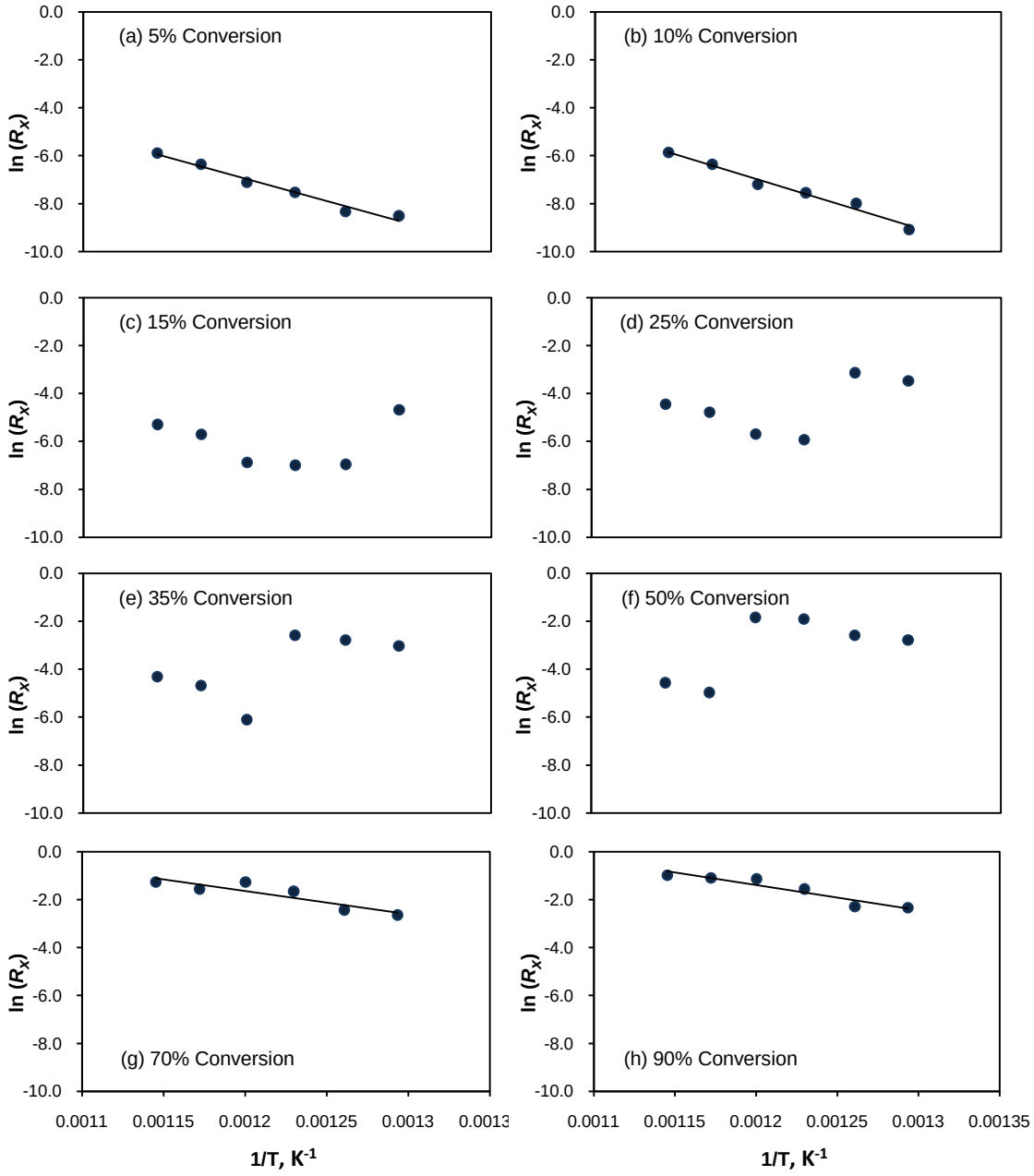

Fig. 5.2 The Arrhenius plots for the reduction of unsupported NiO nanoparticles with CH_4 at various NiO conversion levels.

The Arrhenius plots for the reduction of unsupported NiO nanoparticles with CH_4 and C_2H_6 re-gain their good straight lines at the conversion level of 70% or higher (Fig. 5.2). The activation energies within the conversion range of 70 – 90% are 79 – 88 kJ mol^{-1} for CH_4 and 58 – 62 kJ mol^{-1} for C_2H_6 (Table 5.1). These values are much lower than those obtained at the conversion levels of 5 – 10% and are close to the values of the dissociation energies of CH_4 and C_2H_6 on Ni [28, 30-32]. We believe that at 70% conversion level or higher, the particle surface was occupied mostly, if not all, by the metallic phase. At this stage, the dissociation of gaseous molecules took place dominantly on the nickel surface resulting in the lower activation energies.

For the reduction with H_2, we obtained the straight Arrhenius lines at all conversion levels (5 – 90% conversion). The E_a values (see Table 5.1) which remain unchanged within the experimental uncertainties throughout the course of reduction are close to the dissociation energies of H_2 on Ni [33-36]. The similar values of activation energy obtained at almost all conversion levels suggest that the mechanism of H_2 dissociation on the metallic and oxide surface might be similar and the rates of H_2 dissociation might be determined only by the number of activation sites (e.g. neighbouring Ni atoms).

As is seen in Fig. 5.1, the length of induction period as well as the time required to accomplish complete reduction of unsupported NiO nanoparticles increases in the order of H_2, C_2H_6 and CH_4. It corresponds well to the order of easiness of these molecules to undergo surface dissociation (based on the literature data of their dissociation [28, 30, 32-36]). The results shown in Fig. 5.1, therefore, suggest that the reduction of unsupported NiO nanoparticles in our study was controlled kinetically by the activation of gaseous molecules on the surface.

5.3.2 Consideration of fates and activities of radicals in the kinetics of NiO reduction

Fig. 5.3 shows the NiO conversion as a function of time for the isothermal reduction of silica-supported NiO with CH_4, C_2H_6 and H_2. When CH_4 or C_2H_6 was used as a reducing gas, the time required to reduce silica-supported NiO (Fig. 5.3a &

b) was very much shorter than the time required to reduce unsupported NiO nanoparticles in the same reducing environment (Fig. 5.1a & b). The opposite results, however, were obtained when H_2 was used as a reducing gas (Fig. 5.3c). The time required to reduce supported NiO with H_2 (Fig. 5.3c) was longer than the time required to reduce unsupported NiO (Fig. 5.1c).

We have also noticed that, unlike in the reduction of unsupported NiO nanoparticles where the time required to achieve complete reduction was shortest when H_2 was used as a reducing gas (Fig. 5.1), the time required to reduce silica-supported NiO (Fig. 5.3), on the contrary, was longest with H_2 compared to those with CH_4 and C_2H_6. This signifies that the reduction of silica-supported NiO in this study was not kinetically controlled only by the activation of gaseous molecules on the surface. Clearly, factors other than the activation and mass transfer of molecular species, such as the fates and activities of surface-formed radical species, have to be considered in order to explain the kinetics of NiO/SiO_2 reduction and to provide a plausible explanation for the differences between the reduction kinetics of unsupported nano NiO particles and silica-supported NiO.

As have been described in the literature [5, 14], in order for the reduction to take place, the gas molecules, have to be activated firstly on the particle surface to produce C_xH_y (s) and/or H (s) radical species. In this study, the surface activation of different reductant molecules can be represented as follows:

$$CH_4\ (s) = CH_3\ (s) + H\ (s) \tag{5.3}$$

$$C_2H_6\ (s) = C_2H_5\ (s) + H\ (s) \tag{5.4}$$

$$H_2\ (s) = H\ (s) + H(s) \tag{5.5}$$

These surface radicals can continue to dissociate on the catalyst to form CH_2 (s), CH (s), etc. However, past studies, [16-25], have shown that the radicals on the catalyst surface can, under certain circumstances, desorb from the surface to either combine with each other or react with another gaseous species in the surrounding gas

phase. The ability of a surface radical species to desorb into the bulk gas phase depends largely on the strength of its bonding with the catalyst surface [21, 22] and the extent of resistance on their diffusion (away from the surface) [16-22]. For the unsupported NiO nanoparticles, the absence of rigid pore structure means the absence of intra-particle diffusion resistance for the radicals. The fine size of the particles, on the other hand, is unlikely to cause the formation of thick gas-film to hinder the radical desorption. If the radicals formed on the surface of unsupported nano NiO particles desorb and diffuse away from the surface, the reduction of the NiO particles would be significantly slowed down.

Conversely, for the silica-supported NiO, once the radicals are formed, the rigid pore structures of the silica support impose a great resistance for the radicals to diffuse out of the pores [16-22]. As a result, the desorbed radicals would easily be re-adsorbed onto the same or other NiO surface inside the silica pores. The desorption is no longer a pathway to "lose" the radicals that are essential for the reduction of NiO. The phenomenon of radical desorption and re-adsorption in a porous supported catalyst has been demonstrated elsewhere [17, 20, 22].

Radicals with the lowest binding energy with the surface would be the easiest to desorb. The binding energies of CH_3-Ni, C_2H_5-Ni and H-Ni are 201, 205 and 268 kJ mol^{-1} [37], respectively. Thus, among the three types of surface radicals formed from the surface activation of gaseous molecules in our study, CH_3 (s) and C_2H_5 (s) definitely have higher tendency to desorb than H(s). Agreeing with this explanation, the results of our study (Fig. 5.1 and 5.3) show that the time taken to reduce unsupported NiO nanoparticles was significantly higher than the length of NiO/SiO_2 reduction when CH_4 was used as a reducing gas and slightly higher when C_2H_6 was used as a reductant.

The results with H_2, however, deserve further explanation. As was noted earlier in this chapter, after a period of induction, the reductant molecules would dissociate on the metallic island to form surface radicals. From the dissociation sites on the island, the radicals have to migrate to the Ni-NiO boundary to consume oxygen. While advancing to the Ni-NiO boundary, the radicals have to break and re-form their

bonds repeatedly with the nickel atoms [26]. The ease with which the radicals can advance to the Ni-NiO boundary depends largely on the strength of Ni-radical binding.

The binding energy between Ni and H (s), as stated above, is much higher than the binding energy between Ni and C_xH_y (s). This means, in the reduction of silica-supported NiO where the radicals do not have a chance to leave the silica pores, the C_xH_y (s) radicals have higher mobility and can migrate to the Ni-NiO boundary on the surface far more easily than the H (s) radicals. This could be the reason why the reduction of silica-supported NiO with hydrocarbon reductants was faster than the reduction with H_2.

In Chapter 4 [26], we explained that the size of NiO crystallite can affect the kinetics of NiO reduction significantly. The reduction of NiO in the bulk, which does not only involves the migration of radicals but also involve the movement and re-arrangement of atoms in the bulk, is more difficult than the reduction of NiO on the surface [26]. This means, at a given higher degree of NiO reduction, a bigger NiO crystallite would have a slower reduction rate compared to a smaller NiO crystallite. In this study, the size of NiO crystallite for the unsupported NiO nanoparticles (3.3 nm) was much smaller than the NiO crystallite of the silica-supported NiO (55 nm). This crystallite size difference may explain why under the same reduction conditions, and without the significant "loss" of radicals in both of the cases, the reduction rates of silica-supported NiO were slower than the reduction rates of unsupported NiO nanoparticles when H_2 was used as a reducing gas.

5.3.3 Further discussion on the activities of surface-generated radicals in the reduction of NiO.

The Arrhenius plots of ln (R_x) versus 1/T (such as described earlier in this paper) were plotted for the reduction of silica-supported NiO. The straight Arrhenius lines were obtained within 5 to 90% conversion levels for the reduction of NiO/SiO_2 with any of the reducing gas. Fig. 5.4 shows the values of reduction activation energy and pre-exponential factor at different levels of conversion for the reduction of silica-supported NiO with CH_4, C_2H_6 and H_2.

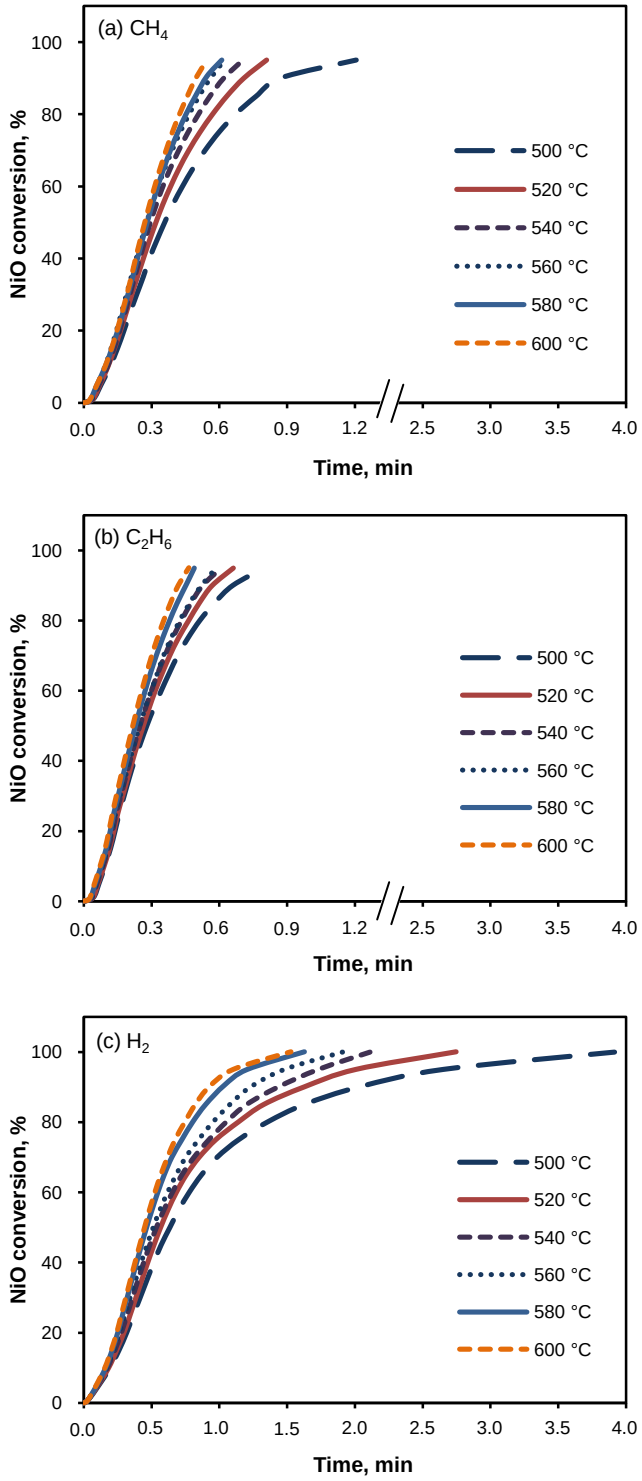

Fig. 5.3 The plots of NiO conversion versus time for the reduction of silica-supported NiO with CH_4 (a), C_2H_6 (b), and H_2 (c) within the temperature range of 500 – 600 °C.

In complete contrast to the reduction of unsupported NiO nanoparticles (Table 5.1) that have been explained earlier, the data in Fig. 5.4 show that the value of activation energy for the reduction of silica-supported NiO increases with the degree of NiO reduction. Supporting our earlier statements, this trend indicates that the limiting factor controlling the reduction kinetics of NiO/SiO_2 was different from that for the reduction of unsupported NiO nanoparticles. Indeed, the values of activation energy at the very low conversion levels for the reduction of silica-supported NiO with CH_4 and C_2H_6 (Figs. 5.4a & b) were found to be too small and far away from the reported theoretical values [28-32] to represent the activation of hydrocarbon gas molecules either on Ni or on NiO. It is important to note that the changes in the observed activation energy with conversion shown in Fig. 5.4 also indicate the absence of significant external (interparticle) mass transfer limitation under our experimental conditions. The observed activation energy would have remained unchanged with conversion had the external mass transfer been the rate-limiting process, because the inter-particle mass transfer (e.g. gas flow rate) did not change during the whole course of reaction.

Interestingly, the increases in the activation energy with the NiO conversion in the reduction of NiO/SiO_2 are accompanied by the similar increases in the value of pre-exponential factor (Fig. 5.4). The mutual dependence between activation energy and pre-exponential factor demonstrates that there exists a kinetic compensation effect in the reduction of NiO/SiO_2 in this study. To confirm the existence of kinetic compensation effect, the Arrhenius plots (ln R_x versus $1/T$) for different conversion levels (with the same reducing gas) are plotted in the same graphs. The interpolated Arrhenius lines converge at two different intersections (Fig. 5.5), thus, confirming the existence of two kinetic compensation effects; one for the lower conversion levels (from 5 to about 30%) and another for the higher conversion levels (50 – 90%). In the study on NiO reduction with H_2 presented in Chapter 4, we showed that these kinetic compensation effects only appear for the reduction of NiO with crystallite size bigger than a certain critical size. The presence of two different kinetic compensation effects means that there are possibly two different mechanisms operative at different levels of NiO conversion [26].

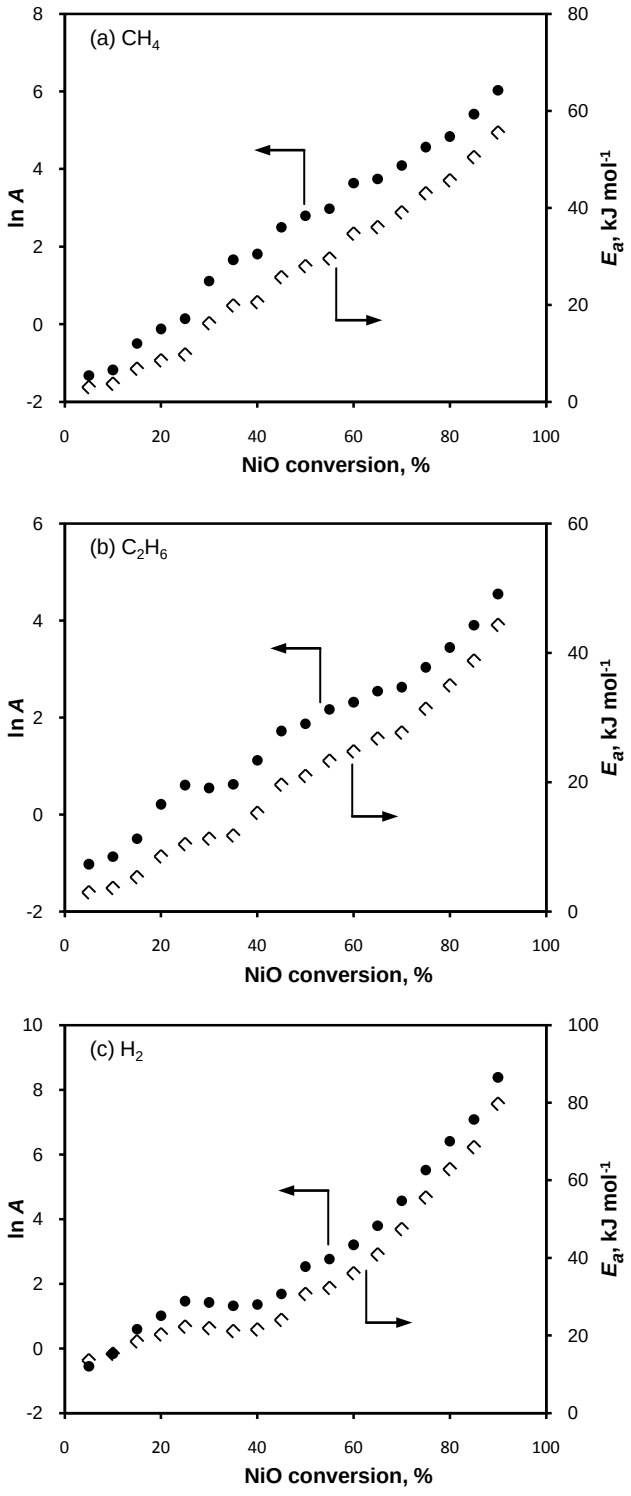

Fig. 5.4 Changes in the activation energy (*Ea*) and pre-exponential factor (ln*A*) with the NiO conversion for the reduction of silica-supported NiO with CH_4 (a), C_2H_6 (b) and H_2 (c).

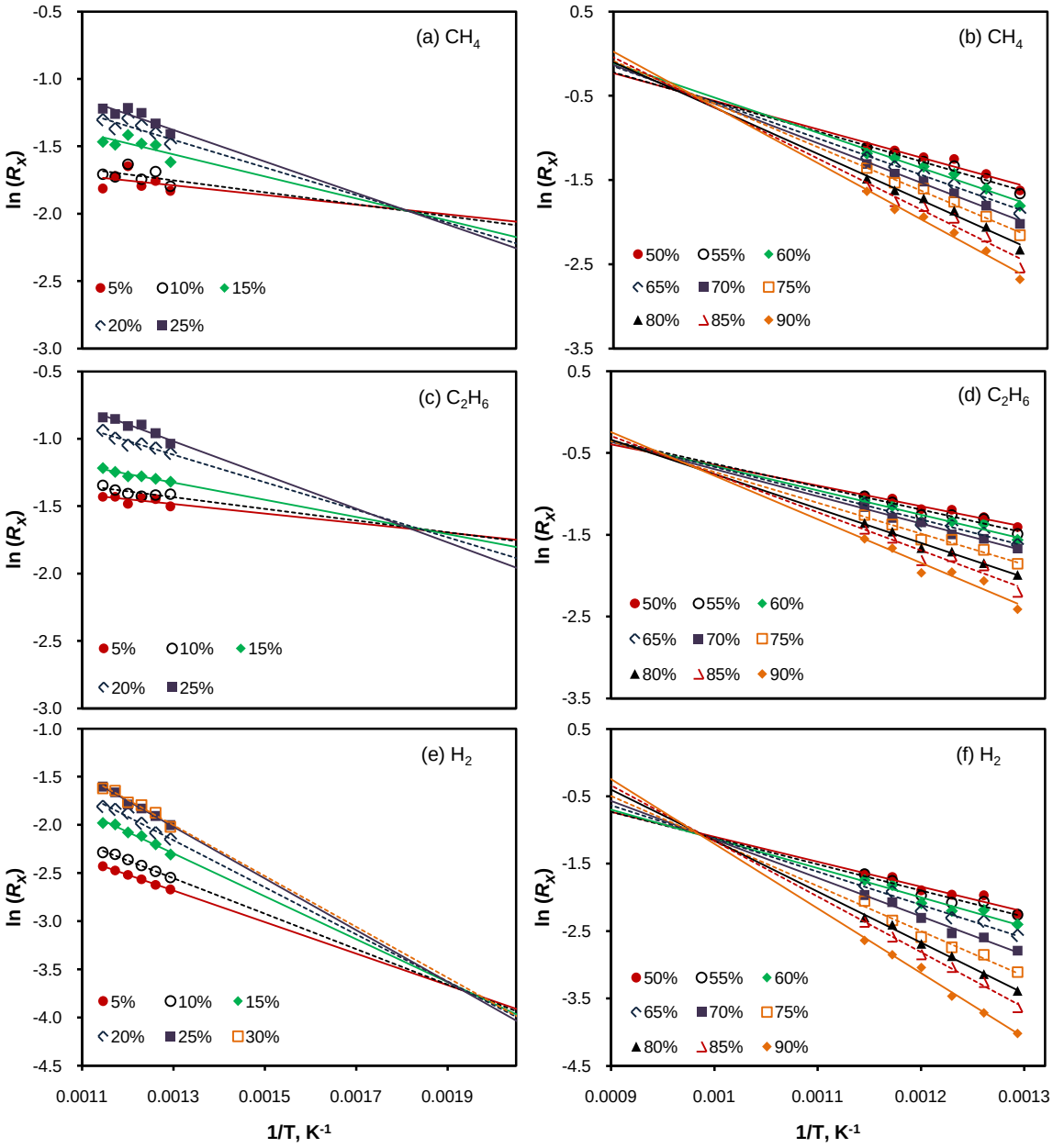

Fig. 5.5 Arrhenius plots for the reduction of silica-supported NiO with different reducing gases.

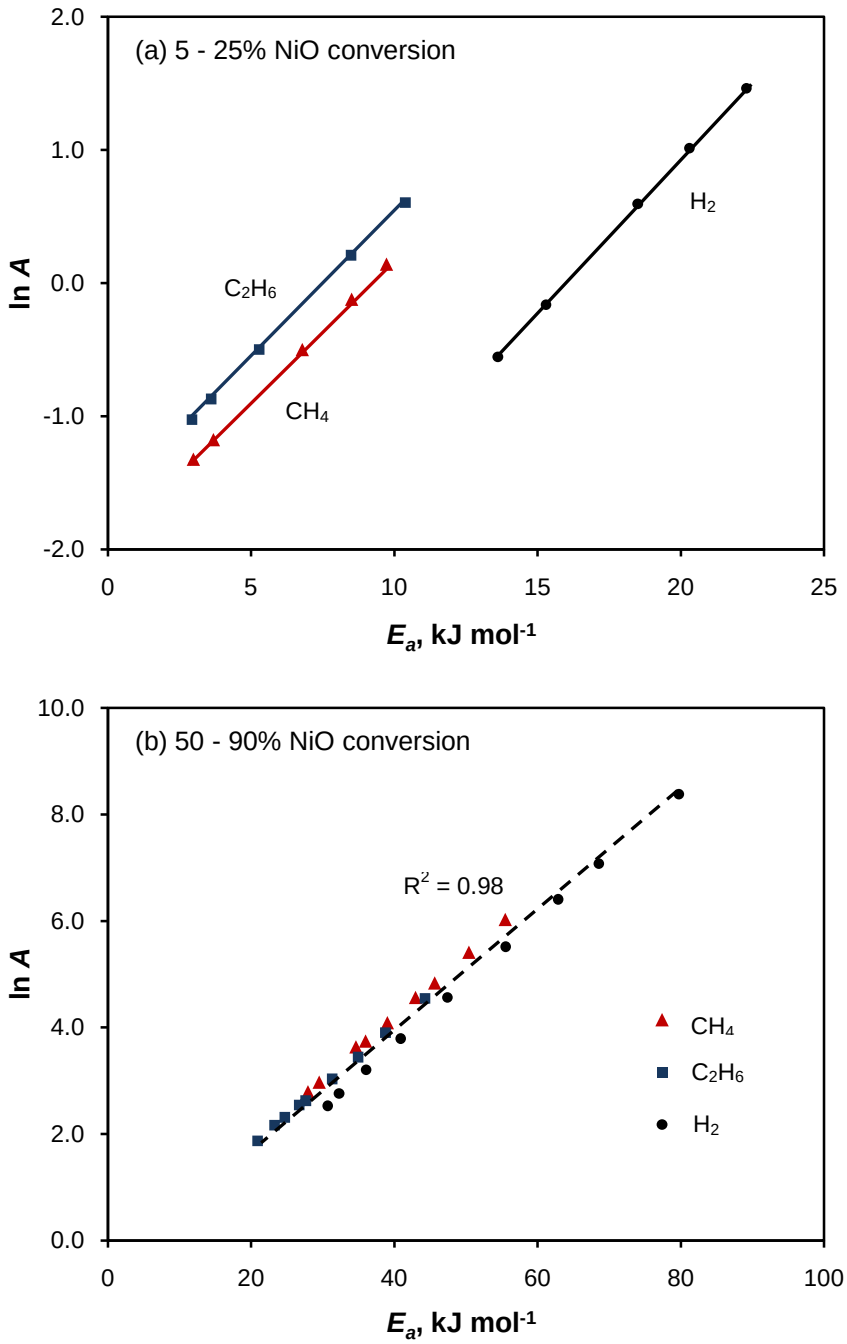

Fig. 5.6 Constable plots of the kinetic compensation effects in the reduction of silica-supported NiO.

Fig. 5.6 shows the relationship between ln$A$ and E_a for the reduction of silica-supported NiO with different reducing gases. As can be seen, two linear correlations of "ln$A$ = mE_a + C" exist for the reduction of NiO/SiO_2 with every reductant gas: one at lower NiO conversion levels (from 5 to about 30%) and the other at higher NiO conversion levels (50 -90%). What is more interesting is that, at lower conversion levels, the relationship between ln$A$ and E_a seems to be dependent on the type of reductant used (as evidenced by the appearance of three separate straight lines) while at higher conversion levels, the relationship between ln$A$ and E_a seems not to be governed by the type of reductant (since all the data for these conversion levels fall into one straight line). The above observations provide further evidence that the reduction of bigger NiO crystallites follows two different mechanisms [26]. At the intermediate NiO conversion levels (30 – 50%), no linear lines between E_a and ln$A$ are observed, suggesting that there is a transition between the two dominant reduction mechanisms.

At low NiO conversions, the reduction of NiO takes place on the outer surface of NiO crystallites. The increase in the size of metallic islands would increase the number of molecular dissociation sites. This would result in the increase of ln$A$. However, as the islands are getting bigger, the migration of radicals to the Ni-NiO boundary would also become more difficult as the radicals require more steps of bond-breaking and bond-reforming with Ni in order to reach the boundary, thus, causing an increase in the overall E_a [26]. As the radical-Ni bonding strength varies with the type of radicals, the kinetic compensation effect between ln$A$ and E_a at lower conversion levels as can be interpreted by the Constable plots in Fig. 5.6a, is determined by the type of gaseous reductants involved in the reduction.

After the metallic islands on the surface overlap (nearly) completely, the Ni-NiO interface would then move inward towards the NiO bulk. For the unsupported NiO nanoparticles with a very small crystallite size (3.3. nm), majority (60 – 70%) of the crystallite atoms, as can be estimated from a literature [38], are located or exposed on the surface. With very little bulk volume, the mechanisms of reduction of the "bulk" would not significantly differ from the mechanism of reduction on the surface. For the silica-supported NiO with much bigger NiO crystallite size (55 nm), the

appearance of different kinetic compensation effects at lower and higher conversion levels (Fig. 5.5b) suggests that the mechanisms involved in the reduction of NiO in the bulk are different from those at lower conversion levels during the metallic islands growth stage.

Unlike at the lower levels of conversion where only the surface radicals migration is important (under our experimental conditions), the reduction of NiO in the bulk requires the movement and re-arrangement of atoms inside the bulk in addition to the radical migration process. As Fig. 5.6b shows, the relationship between ln$A$ and E_a at high conversion levels is independent to the type of reducing gas (Fig. 5.6b). We believe that, at this stage, the characteristics of the particles (e.g. its crystallite size) [26] would possibly have more important influence on the reduction kinetics than the type of radicals produced on the surface.

5.4 Conclusions

While it is traditionally believed that the rates of the gas-solid reactions are controlled either by the rates of molecular transport or by the chemical reaction rates on the solids, our study indicates that this is not always the case. Our experimental results have shown that the fates and activities of surface-formed radicals must be taken into account in order to successfully elucidate the kinetics and mechanisms of nickel oxide reduction. In this study, when the radicals have little difficulties to desorb, the desorption of hydrocarbon radicals has effectively decreased the concentration of radicals on the solid surface to prolong the induction period and thus the overall reduction time of unsupported NiO nanoparticles. However, in the presence of rigid pore structure of silica support, the desorption of radicals out of the pores is greatly hindered. In this case, the ease with which the surface-formed radicals migrate from its formation site to the Ni-NiO boundary determines the rate of reduction of the silica-supported NiO.

5.5 References

[1] R. Alizadeh, E. Jamshidi, H. Ale Ebrahim, Kinetic study of nickel oxide reduction by methane, Chem. Eng. Technol. 30 (2007) 1123-1128.

[2] M.M. Hossain, H.I. de Lasa, Chemical-looping combustion (CLC) for inherent CO_2 separations - a review, Chem. Eng. Sci. 63 (2008) 4433-4451.

[3] J. AdÃ¡nez, L.F. de Diego, F. GarcÃa-Labiano, P. GayÃ¡n, A. Abad, J.M. Palacios, Selection of oxygen carriers for chemical-looping combustion, Energy Fuels 18 (2004) 371-377.

[4] J.T. Richardson, M. Lei, B. Turk, K. Forster, M.V. Twigg, Reduction of model steam reforming catalysts: $NiO/\alpha\text{-}Al_2O_3$, Appl. Catal. A 110 (1994) 217-237.

[5] J.T. Richardson, R. Scates, M.V. Twigg, X-ray diffraction study of nickel oxide reduction by hydrogen, Appl. Catal. A 246 (2003) 137-150.

[6] J. Szekely, J.W. Evans, A structural model for gas-solid reactions with a moving boundary - II : The effect of grain size, porosity and temperature on the reaction of porous pellets, Chem. Eng. Sci. 26 (1971) 1901-1913.

[7] J. Szekely, C. Lin, H. Sohn, A structural model for gas-solid reactions with a moving boundary - V: An experimental study of the reduction of porous nickel-oxide pellets with hydrogen, Chem. Eng. Sci. 28 (1973) 1975-1989.

[8] J. Bandrowski, C.R. Bickling, K.H. Yang, O.A. Hougen, Kinetics of the reduction of nickel oxide by hydrogen, Chem. Eng. Sci. 17 (1962) 379-390.

[9] B. Delmon, A. Roman, Kinetic study of the reduction of nickel oxide near its antiferromagnetic-paramagnetic transition. Influence of the magnetic structure of the reactant on the kinetics of nucleus formation on its surface, J. Chem. Soc., Faraday Trans. 1 69 (1973) 941-948.

[10] G. Parravano, The Reduction of nickel oxide by hydrogen, J. Am. Chem. Soc. 74 (1952) 1194-1198.

[11] H. Charcosset, R. Frety, G. Labbe, Y. Trambouze, Increase of the rate of reduction of NiO by H_2, due to pretreatment with CO or NH_3, J. Catal. 35 (1974) 92-99.

[12] T. Hidayat, M.A. Rhamdhani, E. Jak, P.C. Hayes, The kinetics of reduction of dense synthetic nickel oxide in H_2-N_2 and H_2-H_2O atmospheres, Metall. Mater. Trans. B 40 (2009) 1-16.

[13] J. Evans, S. Song, C. Leonsucre, Kinetics of nickel-oxide reduction by hydrogen - measurements in a fluidized-bed and in a gravimetric apparatus, Metall. Trans. B 7 (1976) 55-65.

[14] O. Ostrovski, G.Q. Zhang, Reduction and carburization of metal oxides by methane-containing gas, AlChE J. 52 (2006) 300-310.

[15] B. Jackson, H. Metiu, The dynamics of H_2 dissociation on Ni(100): A quantum mechanical study of a restricted two-dimensional model, J. Chem. Phys. 86 (1987) 1026-1035.

[16] E.B.H. Quah, C.-Z. Li, Effects of radical desorption on catalyst activity and coke formation during the catalytic pyrolysis and oxidation of light alkanes, Appl. Catal. A 250 (2003) 83-94.

[17] E.B.H. Quah, C.-Z. Li, Roles of desorbed radicals and reaction products during the oxidation of methane using a nickel mesh catalyst, Appl. Catal. A 258 (2004) 63-71.

[18] E.B.H. Quah, C.-Z. Li, Pyrolysis of liquefied petroleum gas assisted by radicals desorbed from mesh catalyst surface, Int. J. Chem. Kinet. 35 (2003) 637-646.

[19] E.B.H. Quah, J.F. Mathews, C.-Z. Li, Interinfluence between reactions on the catalyst surface and reactions in the gas phase during the catalytic oxidation of methane with air, J. Catal. 197 (2001) 315-323.

[20] W.J. Lee, C.-Z. Li, Coke formation and reaction pathways of catalyst-surface-generated radicals during the pyrolysis of ethane using Ni mesh catalyst, Appl. Catal. A 316 (2007) 90-99.

[21] W.J. Lee, C.-Z. Li, Opposite effects of gas flow rate on the rate of formation of carbon during the pyrolysis of ethane and acetylene on a nickel mesh catalyst, Carbon 46 (2008) 1208-1217.

[22] Chapter 3 of this thesis.

[23] D.J. Driscoll, J.H. Lunsford, Gas-phase radical formation during the reactions of methane, ethane, ethylene, and propylene over selected oxide catalysts, J. Phys. Chem. 89 (1985) 4415-4418.

[24] J.H. Lunsford, The role of surface-generated gas-phase radicals in catalysis, Langmuir 5 (1989) 12-16.

[25] K.D. Campbell, J.H. Lunsford, Contribution of gas-phase radical coupling in the catalytic-oxidation of methane, J. Phys. Chem. 92 (1988) 5792-5796.

[26] Chapter 4 of this thesis.

[27] Y. Koga, L.G. Harrison, Reactions of solids with gases other than oxygen, in: C.H. Bamford, C.F.H. Tipper, R.G. Compton, (Eds.), Comprehensive Chemical Kinetics, vol. 21, Elsevier, Amsterdam,1984, pp. 146-149.

[28] B. Xing, X.-Y. Pang, G.-C. Wang, Z.-F. Shang, Investigation the active site of methane dissociation on Ni-based catalysts: A first-principles analysis, J. Mol. Catal. A: Chem. 315 (2010) 187-196.

[29] W.J. Thomas, Chemisorption of ethane at iron and nickel oxide, Trans. Faraday Soc. 53 (1957) 1124-1131.

[30] R.C. Egeberg, S. Ullmann, I. Alstrup, C.B. Mullins, I. Chorkendorff, Dissociation of CH_4 on Ni(1 1 1) and Ru(0 0 0 1), Surf. Sci. 497 (2002) 183-193.

[31] F.C. Schouten, E.W. Kaleveld, G.A. Bootsma, AES-LEED-ellipsometry study of the kinetics of the interaction of methane with Ni(110), Surf. Sci. 63 (1977) 460-474.

[32] J. Gislason, H. Sellers, Desorption and C-H dissociation rate constants for C_2 hydrocarbons on Ni, Pd and Pt, Surf. Sci. 415 (1998) 70-79.

[33] K.D. Rendulic, A. Winkler, H.P. Steinrück, The role of surface defects in the adsorption and desorption of hydrogen on Ni(111), Surf. Sci. 185 (1987) 469-478.

[34] S.M. Foiles, M.I. Baskes, C.F. Melius, M.S. Daw, Calculation of hydrogen dissociation pathways on nickel using the embedded atom method, J. Less-common Met. 130 (1987) 465-473.

[35] H.J. Robota, W. Vielhaber, M.C. Lin, J. Segner, G. Ertl, Dynamics of interaction of H_2 and D_2 with Ni(110) and Ni(110) surfaces, Surf. Sci. 155 (1985) 101-120.

[36] H. Yang, J.L. Whitten, Dissociative adsorption of H_2 on Ni(111), J. Chem. Phys. 98 (1993) 5039-5049.

[37] E. Shustorovich, The bond-order conservation approach to chemisorption and heterogeneous catalysis: applications and implications, Adv. Catal. 37 (1990) 101-163.

[38] G. Palumbo, S.J. Thorpe, K.T. Aust, On the contribution of triple junctions to the structure and properties of nanocrystalline materials, Scripta Metall. Mater. 24 (1990) 1347-1350.

CHAPTER 6

Catalytic oxidation of ethane with fluidised nanoparticle NiO catalyst

Overview:

In this study, the unsupported NiO nanoparticles (<10 nm) were fluidised in a quartz-walled reactor to catalyse the reactions between ethane and oxygen in the temperature range of 240 to 420 °C. For comparison, the reaction was also studied with the traditional porous-type NiO/SiO_2 (60 wt% NiO) as the catalyst in the same reactor. Our data show that the two fluidised-bed catalytic systems behave differently. While the reactions in the fluidised bed of nanoparticles show characteristics similar to the gas-phase reactions, the reactions of ethane-O_2 mixture with NiO/SiO_2, on the contrary, show the characteristics of a reaction system rate-limited by the surface reactions. These differences can be explained by considering the difference in the diffusion resistance for the desorption of radicals from the catalyst surface between the nanoparticle system and the porous-catalyst catalytic system, respectively.

6.1 Introduction

The catalytic reactions of light hydrocarbons are extremely complicated, comprising a large number of elementary radical reactions on the catalyst surface and in the gas phase. Adding to the complexity, studies [1-10] have shown that the surface-formed radicals can desorb to take part in the gas-phase reactions. Without the complications of catalyst internal pore structure with the use of non-porous Ni mesh catalyst in our previous studies [4-10], we have shown that the desorption of radicals into the bulk gas phase can occur if the mass transfer limitations imposed by the gas film around the Ni wires are minimised, i.e., by increasing the gas flow rate traversing the mesh [4-10].

When a traditional porous supported catalyst is used, the presence of pore diffusion resistance prohibits the transfer of surface-generated radicals into the bulk gas phase. In addition to their gas-phase reactions within the pores, the desorbed radicals can also easily be re-adsorbed onto the catalyst surface [5, 8, 10]. The repeated radical desorption and re-adsorption inside the catalyst pores make the investigation of catalytic reaction pathways using a traditional supported catalyst an intricate task.

For a single unsupported nanoparticle, the absence of abundant and rigid porous structure means the almost complete absence of intra-particle mass transfer barriers. Unlike the normal Geldart-C particles, nanoparticles are fluidisable in the form of loose agglomerates [11-14] that continuously break and re-form while fluidised [14]. Nanocoating studies [15, 16] showed that the primary nanoparticles instead of their aggregates were individually coated in the fluidised-bed reactor. If reactions are catalysed by fluidised fine nanoparticles with no internal pore structure, the radicals formed on the surface would be able to desorb into the bulk gas phase to greatly alter the reaction pathways from those in the absence of radical. With other appealing advantages, for instances, good mixing and uniform temperature inside the catalyst bed, a nanoparticle fluidised-bed reactor is significantly superior to the traditional reactor system for the study of heterogeneous catalytic reactions.

The use of fluidised nanoparticles as catalyst may also bring significant changes to our chemical and energy industries. When supported catalysts are used, majority of reactor volume is occupied by the support, not the active catalyst. The use of fluidised nanoparticle catalysts in place of the traditional supported catalysts in an industrial reactor will drastically increase the ratio of active catalyst to reactor volume, thus allow the reactor size to be reduced significantly. The ability of radicals to desorb from the nanoparticle catalyst would also create an opportunity to avoid catalyst deactivation by coke formation [4, 8], a major nuisance in many commercial chemical processes.

The conversion of light hydrocarbon using fluidised NiO nanoparticles as catalyst, which has never been reported anywhere before, was explored for the first time. The catalytic reaction of ethane-oxygen mixture, an environmentally and operationally benign alternative for ethylene production [17, 18], was chosen as the model system to be studied. Comparison of the results between the fluidised nanoparticles catalytic system to that of the traditional porous supported catalyst system provides some insights into the fates and reaction pathways of the surface-generated radicals during the catalytic reaction of ethane-oxygen mixture.

6.2 Experimental

All experiments were performed in a quartz-walled fluidised-bed reactor which design has been described in details in Chapter 2. NiO nanoparticles from Nanostructured and Amorphous Inc (USA) were used as the catalysts. They first underwent a thermal treatment under an argon flow at 350 ºC for 45 mins to remove moisture and possible impurities. After the heat treatment, the catalyst particles were sieved to remove large agglomerates before being weighed and subsequently fed into the reactor. From our examination using transmission electron microscopy (TEM), the sizes of NiO nanoparticles before the experiments were in the range of 5 – 10 nm. This agrees well with our estimation (~ 8 nm) based on the BET surface area (assuming spherical shape) of the particles (Table 6.1).

For the porous catalyst system, the catalyst was NiO supported on silica (60 wt% NiO). They were purchased from Sigma-Aldrich and the particle size was between 150 – 250 μm. The BET surface area, pore volume and pore width of this catalyst were determined to be around 143 m^2 g^{-1}, 0.29 ml g^{-1} and 8.41 nm respectively and the XRD-estimated crystallite size of NiO for this catalyst was about 55 nm.

Reactant gases used in this study were ethane (BOC), oxygen (Coregas) and argon (BOC) of the ultra-high purity grade. The flow rates of the gases were controlled separately with mass flow controllers. The reactant gases were premixed before they were fed to the bed from bottom through a porous frit distributor plate (<100 μm) of 4 mm thickness. In the initial stage of our study, we identified the gas velocity capable of fluidising each type of the catalyst particles. The flow rates used for all the catalytic reaction studies were ensured to be in the fluidisation range of the particular type of particles.

The catalysts were firstly pre-heated inside the reactor while flowing the argon gas before the flow was switched to either C_2H_6/O_2/Ar mixture for the oxidative reaction, or C_2H_6/Ar mixture for the non-oxidative reaction. Furnace temperature was then adjusted to allow reaction temperature to achieve its required value. In all experiments, the reaction temperature was monitored by a K-type thermocouple inserted into the catalyst bed. By moving the thermocouple to various locations within the catalyst bed, we confirmed the absence of hot spots in our systems.

The product gas exiting from the top of the reactor first flowed through a water scrubber before being filtered and vented out through a laboratory fume extractor. This was done to make sure that no particles can escape into the atmosphere. During the course of all experiments, product gas was sampled at least 5 – 6 times using Tedlar gas sampling bags. The gas samples were analysed using two gas chromatography (GC) systems; the Perkin Elmer Autosystem XL GC and the HP 5890. The mass balance was checked for every sample and was always found within 97%. In this study, the fresh and spent catalysts were examined by means of X-ray diffraction (XRD), transmission electron microscopy (TEM) and Brunauer-Emmett-Teller (BET) surface area measurement.

Table 6.1 Crystallite size of NiO/Ni, BET surface area and the estimated particle size of catalysts before and after some experiments.

Description	Crystallite Size (nm)		BET Surface Area (m^2/g)	Estimated Particle Size $D = 6000/(SA \cdot \rho)$ (nm)
	NiO	Ni		
Nanoparticles just after heat treatment	3.3	-	111.29	8.08
Nanoparticles after oxidation at 320 °C	3.6	-	109.23	8.24
Nanoparticles after oxidation at 380 °C	3.9	-	104.37	8.62
Nanoparticles after non-oxidative reaction at 320 °C	4.2	24.2	24.33	36.98[a] (27.69)[b]
Nanoparticles after non-oxidative reaction at 380 °C	4.7	22.8	34.11	26.37[a] (19.75)[b]
Fresh NiO/SiO_2	54.7	-	142.05	-
NiO/SiO_2 after oxidation at 320 °C	56.7	-	142.89	-
NiO/SiO_2 after oxidation at 380 °C	53.3	-	144.13	-

a: calculated based on true density of NiO

b: calculated based on true density of Ni

6.3 Results and discussion

6.3.1 Catalytic conversion of ethane inside a fluidised-bed nanoparticle reactor

The catalytic conversion of ethane in a fluidised-bed reactor containing NiO nanoparticles was firstly investigated in both the presence and absence of oxygen at different temperatures. For every temperature studied, the total flow rate of the feed gas was adjusted so that the superficial velocity of the gas through the catalyst bed (i.e. velocity in the absence of any particle or obstruction inside the bed) always equals to 4.1 m min^{-1} (at reaction temperature).

6.3.1.1 Key observations in the presence and absence of molecular oxygen

We found that the oxidative conversion of ethane ($C_2H_6/O_2/Ar$ = 10/5/85 by vol) started to take place at a temperature slightly above 200 °C (Fig. 6.1). Please note

that each datum shown in Fig. 6.1 represents an average value of the samples collected within 100 minutes operation of every experiment during which the reaction rate was constant (e.g. Fig. 6.2a – the data in Fig. 6.2b will be discussed below).

The only products detected by the GCs in the oxidation of C_2H_6 were C_2H_4 and CO_2 (Fig. 6.2a), in broad agreement with the previous studies [19-25]. Our results show that the conversion of ethane (Fig. 6.1) increased with increasing temperature, reaching a maximum level around 30% conversion at 380 °C when the oxygen was completely consumed. Further increase in temperature up to 420 °C did not cause further change either in the conversion level or the product selectivity (at least within 100 minutes of operation). However, from the temperature of 430 °C (Fig. 6.2b), we observed that the C_2H_4 selectivity immediately dropped and the particles defluidised after the reactant gas flowed into the reactor for more than 40 min.

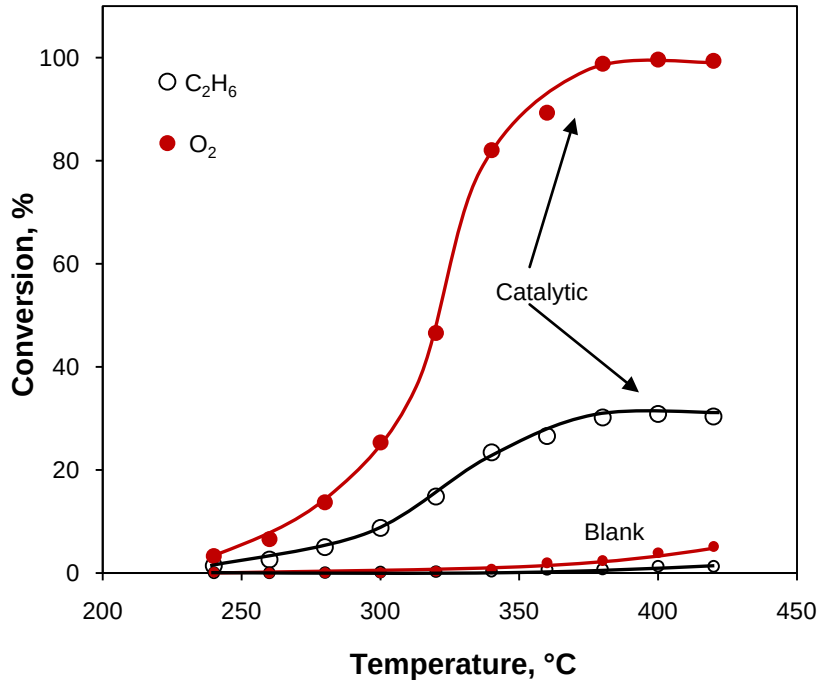

Fig. 6.1 Reactant conversion as a function of temperature for the oxidation of ethane with and without the fluidised NiO nanoparticles. In all experiments, gas superficial velocity = 4.1 m min^{-1} and $C_2H_6/O_2/Ar$ = 10/5/85 (by vol).

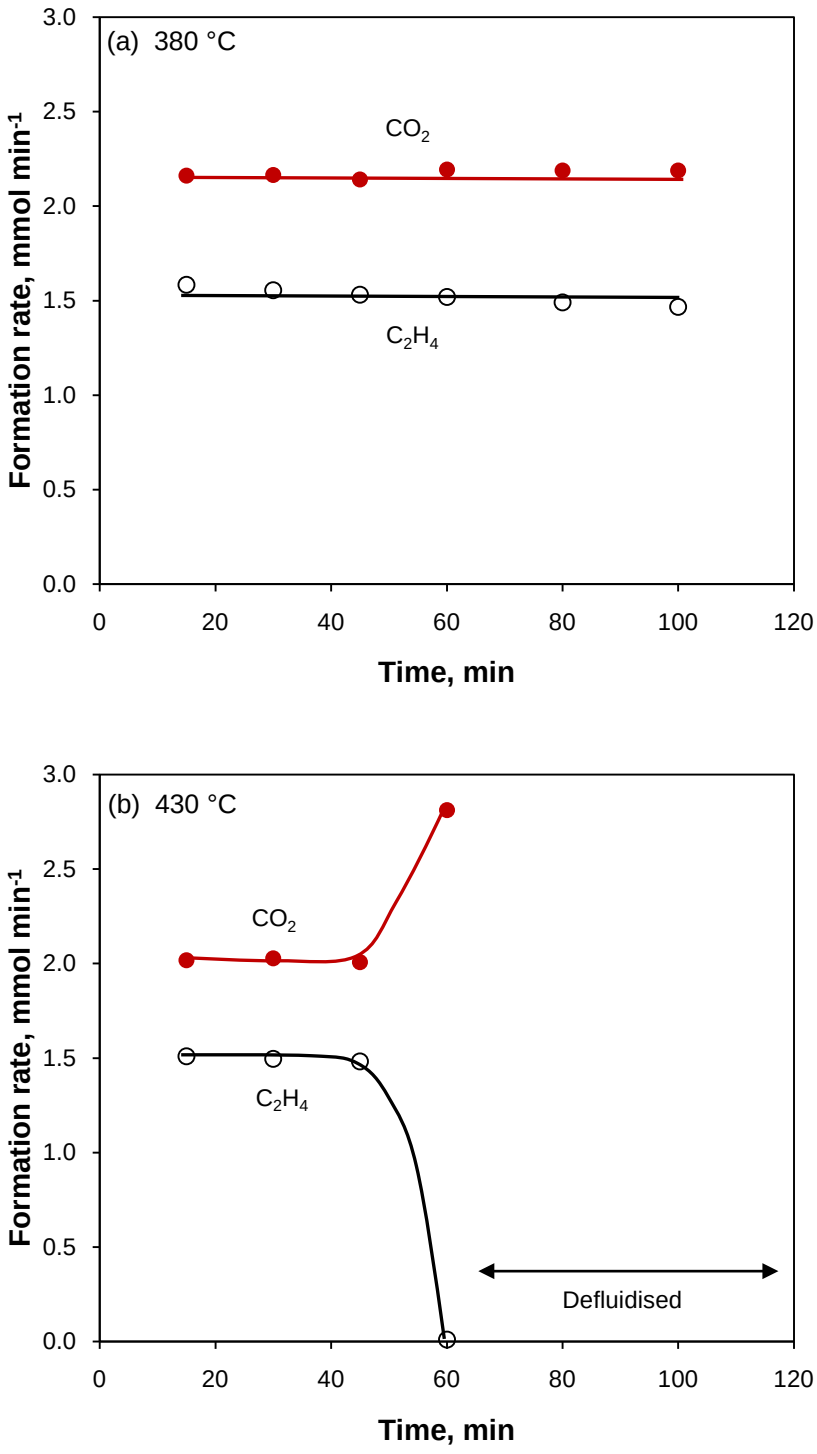

Fig. 6.2 Product formation rate as a function of time for the catalytic oxidative reaction of ethane with fluidised NiO nanoparticles at 380 °C (a) and 430 °C (b).

In the absence of gaseous oxygen (C_2H_6/Ar = 10/90 by vol), no reaction product was detected at temperatures up to 300 °C (Fig. 6.3), even after 150 mins. However, from 320 °C, the reaction of ethane with the fluidised NiO nanoparticles resulted in the direct conversion of ethane to CO_2. The formation of CO_2 (inset of Fig. 6.3) increased gradually with the reaction time, accompanied by the formation of minute amounts of H_2 and CO, at later stages. The formation of CO_2 continued to increase up to the point where the catalyst particles stop to fluidise, i.e., settled down at the bottom of reactor (we did not continue the reactions after particles defluidised). The time the particles could sustain the fluidisation in the absence of oxygen shortened significantly with increasing temperature (Fig. 6.3).

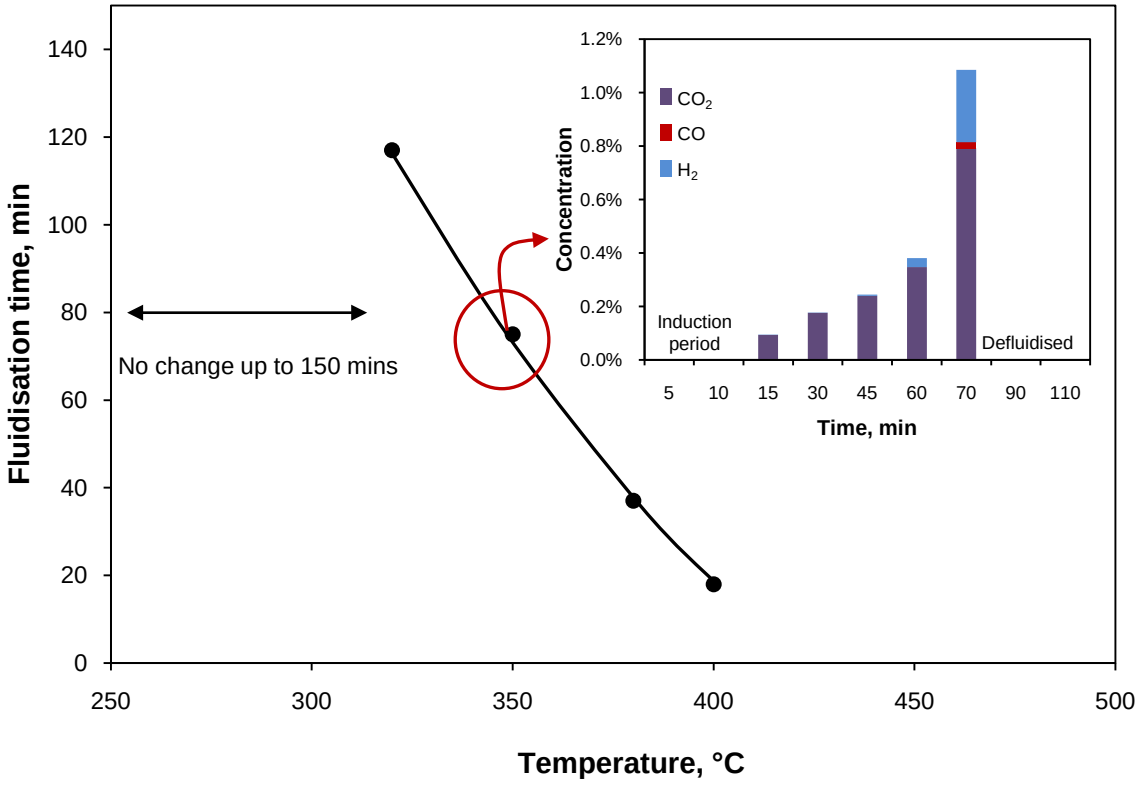

Fig. 6.3 Fluidisation time of the NiO nanoparticles in the mixture of C_2H_6 and Ar (C_2H_6/Ar = 10/90 by vol) as a function of temperature. The inset shows the concentrations of reaction products as a function of holding time at 350 °C.

Fig. 6.4 shows the XRD patterns for the catalysts that have been used in the oxidation (remained to fluidise until the end of experiments) and non-oxidative (defluidised) reactions. As can be seen, the "defluidised" particles show clear Ni peaks and NiO peaks while the "fluidised" particles show only the NiO peaks. Further studies on the used catalysts have been carried out by TEM/EDX. No evidence of carbon formation was found with any of the samples. The possibility that carbon formation on the catalyst surface has led to the defluidisation can therefore be ruled out. We believe that the reason for the defluidisation was due to the sintering of the reduced/partially reduced particles. The results of BET surface area in Table 6.1 provide evidence for the extreme changes in the surface area of particles from > 100 m^2 g^{-1} at the "fluidised" condition to around 24 – 34 m^2 g^{-1} when they became "defluidised".

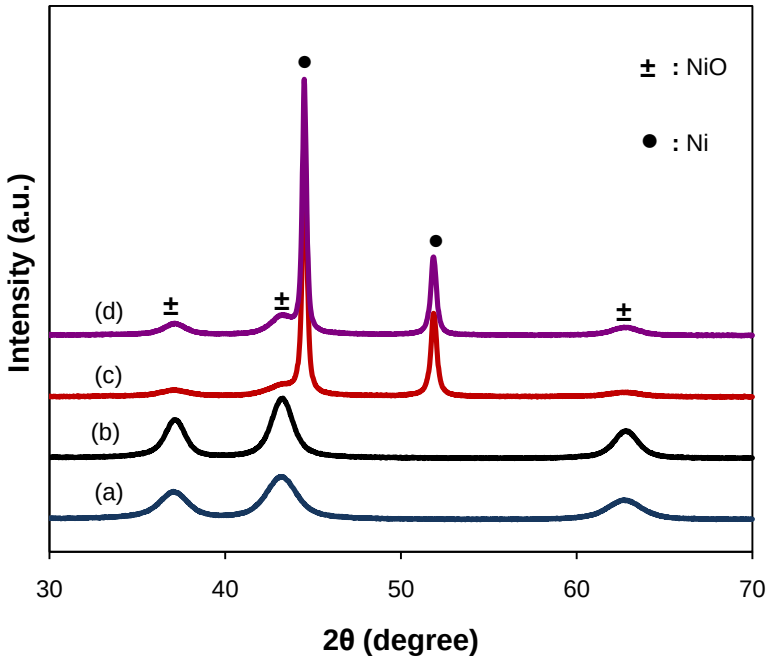

Fig. 6.4 XRD patterns of the spent nanoparticles used in oxidation at 320 °C (a) and 380 °C (b) and non-oxidative reaction at 320 °C (c) and 380 °C (d). Note that nanoparticles in (a) and (b) remained fluidised until the end of experiments, while nanoparticles in (c) and (d) were defluidised.

6.3.1.2 Desorption of radicals from the surface of fluidised NiO nanoparticles

Production of ethylene via the oxidative dehydrogenation of ethane over a metal oxide catalyst is commonly said [25-28] to take place over a redox mechanism, in which the reduction of catalyst by the adsorbed ethane through the extraction of oxide oxygen is followed by the re-oxidation of catalyst by the molecular oxygen [25-28]. Detailed of this mechanism [28, 29] are explained and represented by reactions (6.1) to (6.9) below.

$$C_2H_6\ (g) \longrightarrow C_2H_5\ (s) + H\ (s) \tag{6.1}$$

$$C_2H_5\ (s) \longrightarrow C_2H_4\ (s) + H\ (s) \tag{6.2}$$

$$C_2H_5\ (s) + O\ (s) \longrightarrow C_2H_5O\ (s) \tag{6.3}$$

$$C_2H_5O\ (s) \longrightarrow CH_3CHO\ (s) \longrightarrow CH_3COO\ (s) \longrightarrow CO_x\ (s) \tag{6.4}$$

$$C_2H_5O\ (s) \longrightarrow C_2H_4\ (s) + OH\ (s) \tag{6.5}$$

$$H\ (s) + O\ (s) \longrightarrow OH\ (s) \tag{6.6}$$

$$H\ (s) + OH\ (s) \longrightarrow H_2O\ (s) \tag{6.7}$$

$$OH\ (s) + OH\ (s) \longrightarrow H_2O\ (s) + O\ (s) \tag{6.8}$$

$$O_2\ (g) \leftrightarrow O_2\ (s) \leftrightarrow O_2^-\ (s) \leftrightarrow O_2^{2-}\ (s) \leftrightarrow 2O^-\ (s) \leftrightarrow 2O^{2-}\ (s) \leftrightarrow 2O\ (s) \tag{6.9}$$

The formation of ethyl and hydrogen radical by the rupture of C-H bond (6.1) is the first step of the reaction. The surface ethyl species may either undergo further dehydrogenation to form ethylene (6.2) or react with the oxide to form ethoxy radical (6.3). The surface ethoxy radical may undergo two different reactions; the α-hydrogen abstraction that leads to the formation of undesired CO_x product (6.4) or the β-hydrogen abstraction that produce the desired ethylene product (6.5) [28]. The removal of oxygen from NiO via H_2O formation can be represented by reactions (6.6) to (6.8) [28] and the regeneration of the oxidised site follows the sequence showed in reaction (6.9) [25].

While the mechanism described above suggests that ethylene can be produced in the absence of gaseous oxygen [e.g. through the sequence of reactions (6.1) , (6.3) and (6.5)], our data show that the reaction of ethane with fluidised NiO nanoparticles in the absence of O_2 never resulted in the formation of ethylene. The non-oxidative reaction either did not show any product formation or completely oxidised ethane to CO_x (Fig. 6.3). This is in contrast with the reaction in the presence of gaseous O_2 (240 – 420 °C), where ethylene was always detected in the product gas (see Section 6.3.1.1).

In addition to the difference in the product selectivity (i.e. mainly C_2H_4 or mainly CO_x) between the reactions in the presence and absence of O_2, the reactions also differ in their onset temperature. Our data in Figs. 6.1 and 6.3 show that the conversion of ethane could occur in the presence of molecular oxygen at temperatures (from 240 °C) lower than the temperature (320 °C) at which ethane started to show some interactions with the oxide particles in the absence of O_2. To investigate the importance of surface oxygen intermediates formed by the interactions of molecular oxygen with NiO nanoparticles (6.9) in the activation of ethane during the oxidative reaction, we carried out a “swing” type experiment where the oxygen was first flowed into the reactor before the reaction was quickly shifted to the non-oxidative mode. Even with this experiment, we still could not see the formation of ethylene and the conversion of ethane within 240 to 300 °C without the co-feeding of ethane and O_2.

Our data thus indicate that the molecular oxygen played important roles in the reactions in the gas phase, not on the catalyst surface, during the catalytic oxidation of ethane with fluidised NiO nanoparticles under our experimental conditions. If we exclude the unimolecular or the bimolecular activation of ethane in the gas phase which are impossible at low temperature (as evidenced by the blank experiments showed in Fig. 6.1), the only possible means of the involvement of gas-phase reactions involving molecular oxygen is through the participation of reactive intermediates (i.e. radicals) that have desorbed from the catalyst surface.

As reaction (6.1) shows, the activation of ethane (see also details below) on the catalyst surface results in the formation of radicals (C_2H_5 and H) on the surface. Many studies [1-10] have shown that the surface-generated radicals do not always continue their reactions on the surface but instead desorb into the gas phase. We believe that the desorption of C_2H_5 radicals (6.10) in our study has significantly reduced the chance of reactions (6.2) to (6.5) to take place on the surface.

$$C_2H_5\ (s) \longrightarrow C_2H_5\ (g) \qquad (6.10)$$

In the presence of molecular oxygen, reactions (6.11) to (6.21) below may take place in the gas phase upon the desorption of C_2H_5 radicals. It is important to note, however, that we only show the main reactions and do not intend to list all the possible elementary reactions in the gas phase [30-35]. Clearly, the desorption of C_2H_5 radicals (even in the small number) in the presence of O_2 would not only encourage the formation of C_2H_4 by reaction (6.11), but also encourage other radical reactions in the gas phase [(6.12) – (6.21)].

$$C_2H_5\ (g) + O_2\ (g) \longrightarrow C_2H_4\ (g) + HO_2\ (g) \qquad (6.11)$$

$$HO_2\ (g) + C_2H_6\ (g) \longrightarrow C_2H_5\ (g) + H_2O_2\ (g) \qquad (6.12)$$

$$HO_2\ (g) + HO_2\ (g) \longrightarrow H_2O_2\ (g) \qquad (6.13)$$

$$H_2O_2\ (g) + M \longrightarrow OH\ (g) + OH\ (g) \quad (6.14)$$

$$OH\ (g) + C_2H_6\ (g) \longrightarrow C_2H_5\ (g) + H_2O\ (g) \quad (6.15)$$

$$OH\ (g) + C_2H_4\ (g) \longrightarrow CH_3\ (g) + CH_2O\ (g) \quad (6.16)$$

$$CH_3\ (g) + O_2\ (g) \longrightarrow CH_2O\ (g) + OH\ (g) \quad (6.17)$$

$$CH_2O\ (g) + OH\ (g) \longrightarrow CHO\ (g) + H_2O\ (g) \quad (6.18)$$

$$CHO\ (g) + OH\ (g) \longrightarrow CO\ (g) + H_2O\ (g) \quad (6.19)$$

$$CO\ (g) + OH\ (g) \longrightarrow CO_2\ (g) + H\ (g) \quad (6.20)$$

$$H\ (g) + O_2\ (g) \longrightarrow HO_2\ (g) \quad (6.21)$$

In the absence of O_2 and the chain-propagating radicals (i.e. OH and HO_2), reaction (6.11) and its subsequent chain reactions did not take place in the gas phase to give significant conversion of C_2H_6 and production of C_2H_4. The only possible reaction of C_2H_5 radicals is their disproportion via reaction (6.22) or recombination via reaction (6.23). Although these reactions may results in the formation of other species (i.e. C_2H_4 and C_4H_{10}), the concentration of these species (as expected by the negligible C_2H_6 conversion) was too small to be detected by the GC.

$$C_2H_5\ (g) + C_2H_5\ (g) \longrightarrow C_2H_4\ (g) + C_2H_6\ (g) \quad (6.22)$$

$$C_2H_5\ (g) + C_2H_5\ (g) \longrightarrow C_4H_{10}\ (g) \quad (6.23)$$

The inset of Fig. 6.3 shows that there was an induction period before CO_2 appears in the non-oxidative reaction of ethane. This induction period suggests that the desorption of C_2H_5 radicals has prevented significant reduction of NiO from occurring. (This has been discussed in great details previously in Chapter 5). In the initial stage of reduction (induction), where small number of Ni^0 atoms existed on the surface of NiO particles, the rate of C_2H_6 was quite low. C_2H_5 radicals formed on the surface, meanwhile, would have higher chance to desorb than to re-form a bond with another Ni^0 atom. With the progress of reduction, more Ni^0 atoms would appear on the surface [36, 37]. The increased number of Ni^0 atoms brought two consequences: First, it will increase the rate of C_2H_6 dissociate on the surface [36, 37]. Second, there would be more venues for the re-formation of C_2H_5-Ni bond to occur and this would consequently encourage the continuous dehydrogenation of C_xH_y (6.24) to take place on the surface to result in the reduction of NiO via the formation of CO_2 (6.25 – 6.26) and H_2O (6.6 – 6.8).

The increased formation of CO_2 with time in the absence of O_2 (inset of Fig. 6.3) and the shift in product selectivity (after 50 minutes) in the oxidative reaction at 430 °C (Fig. 6.2b) were clearly the results of the increased number of Ni^0 atoms on the surface due to the reduction of NiO that promotes reactions (6.1) and [(6.24) – (6.26)]. To a certain point after the reduction, the concentration of oxygen of the NiO would become depleted. At this point, reactions [(6.6) – (6.8)] and (6.26) would be less favoured, thus, encouraging the appearance of CO and H_2 (6.27) as the products at later stage in the non-oxidative reaction of ethane (inset of Fig. 6.3).

$$C_2H_5\,(s) \longrightarrow C_2H_4\,(s) \longrightarrow C_2H_3\,(s) \text{ ..... } \longrightarrow 2C\,(s) \qquad (6.24)$$

$$C\,(s) + O\,(s) \longrightarrow CO\,(s) \qquad (6.25)$$

$$CO\,(s) + O\,(s) \longrightarrow CO_2\,(s) \qquad (6.26)$$

$$H(s) + H\,(s) \longrightarrow H_2\,(s) \qquad (6.27)$$

6.3.2 Comparison between the unsupported NiO nanoparticles and the silica-supported NiO as the catalysts in the oxidation of ethane in a fluidised-bed reactor

Figs. 6.5 and 6.6 show the effects of temperature on the catalytic oxidation of ethane in the fluidised-bed reactor. As can be seen, with the fluidised NiO nanoparticles as the catalyst, increasing temperature resulted in the decreased selectivity of C_2H_4 and the increased selectivity of CO_2 (Fig. 6.5). A very different selectivity trend as a function of temperature, however, was observed when the porous supported NiO/SiO_2 was employed as the catalyst for the same reaction inside the same reactor (Fig. 6.6). With NiO/SiO_2, product selectivity remained constant when the temperature was increased up to 380 °C and showed a slight decrease in CO_2 selectivity when the temperature was further increased up to 420°C. Our data also show that while C_2H_4 was the main product (based on C-selectivity) in the nanoparticle system, CO_2 turned out to have a higher selectivity than C_2H_4 in the supported catalyst system. Although the superficial gas velocity used in the two reactor systems was different (4.1 m min^{-1} for nanoparticle system and 6.2 m min^{-1} for NiO/SiO_2 system), we ascertained that the difference of 2.1 m min^{-1} in gas velocity was not the main reason for the differences in product selectivity trend explained above. This is based on our observation that the product selectivity did not change when the superficial velocity was varied from 4.1 to 6.5 m min^{-1} for the oxidation of ethane with fluidised NiO nanoparticles (Fig. 6.7).

We have also considered the possible effects of molecular mass transfer in causing the differences in product selectivity. For this purpose, we ground the NiO/SiO_2 particles and sieved them to different size fractions before they were used to catalyse the reactions of ethane-O_2 mixture at different temperatures. Data in Fig. 6.8 show no significant difference in product selectivity with the changes in the NiO/SiO_2 size, suggesting that the transport of molecular species inside the silica pores was not responsible for the difference in the product selectivity trend between the nanoparticle and supported NiO/SiO_2 catalytic systems used in this study.

A plausible explanation to the different selectivity trends of the two catalytic systems as detailed below, therefore, has to consider the mass transfer of reactive

radical species [4-10]. We explained in the Section 6.3.1.2 that upon their formation via reaction (6.1), C_2H_5 radicals could leave the NiO surface by desorbing into the gas phase. The simple physical structure of NiO nanoparticles, i.e. lack of rigid pore structure, allowed the desorbed C_2H_5 to immediately diffuse into the bulk gas phase to participate in the homogeneous gas-phase reactions [(6.11) – (6.21)]. Increasing temperature would certainly increase the rate of chemical reactions. In the nanoparticle system, where the supply of C_2H_5 radicals into the gas phase is rate-limiting, the promotion of reaction (6.11), due to the increased concentration of C_2H_5 (g) with increasing temperature, would consequently promote the formation of chain-propagating radicals, OH, via reactions (6.12) – (6.14). Since OH is very reactive, it will not only take part in the reaction with ethane (6.15) to produce more C_2H_4 (6.11) but would also be responsible for the further degradation of C_2H_4 to CO_2 [(6.16) – (6.20)].

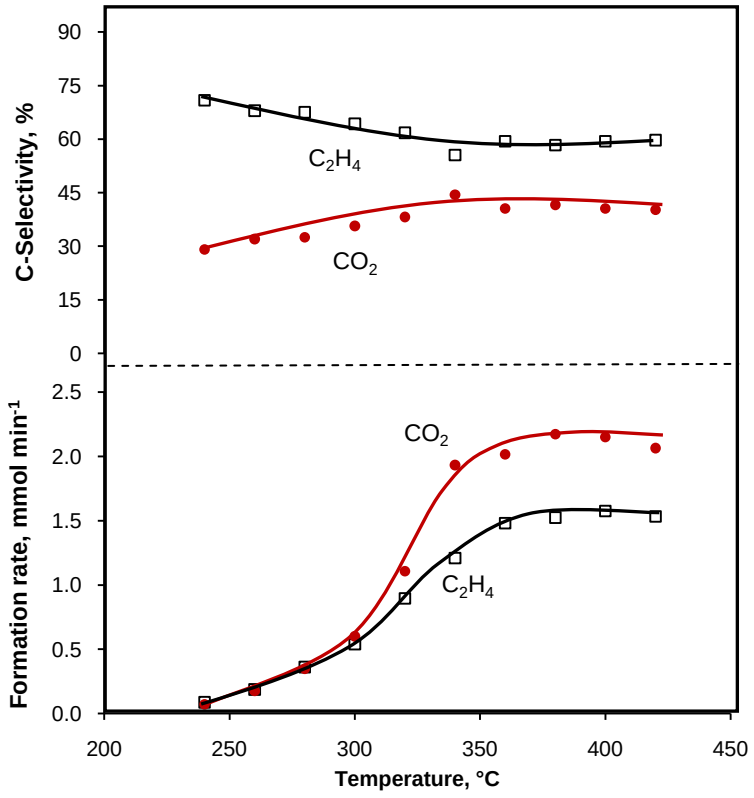

Fig. 6.5 Effects of temperature on the catalytic ethane-O_2 reaction with fluidised NiO nanoparticles. In all experiments, superficial velocity = 4.1 m min^{-1} and the amount of catalyst used = 5.5 g.

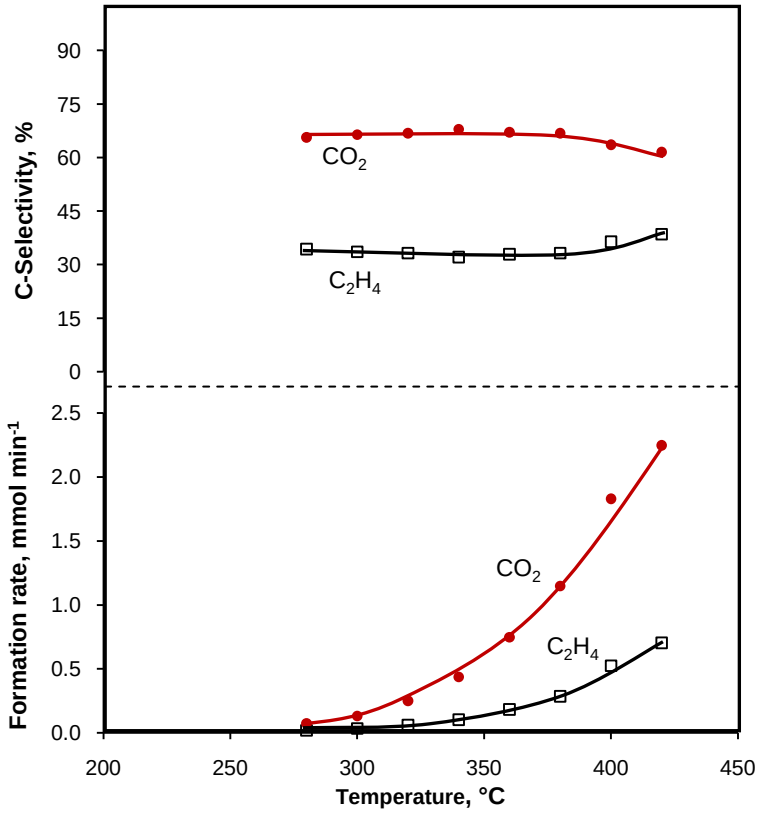

Fig. 6.6 Effects of temperature on the catalytic ethane-O_2 reaction with SiO_2-supported NiO. In all experiments, superficial velocity = 6.2 m min^{-1} and the amount of catalyst used = 9.2 g.

The increased rates of reactions (6.1) and (6.11) also mean the decrease in the concentration of C_2H_6 and the increased concentration of C_2H_4 in the gas phase. This in turn means the increase in the ratio of $k_{6.16}$ $[C_2H_4]/k_{6.15}$ $[C_2H_6]$, indicating the increased relative importance of the degradation of C_2H_4. In other words, the ultimate effect of temperature increase in the nanoparticle system is the increased selectivity of the degradation product (CO_2). Fig. 6.5 shows that the CO_2 selectivity continued to increase with the increase in temperature until about 380 °C when C_2H_6 conversion became constant due to the complete consumption of O_2 (Fig. 6.1). The dependence of CO_2 selectivity with C_2H_6 conversion emphasises the importance of surface-generated gas-phase reactions in the nanoparticle system as outlined above.

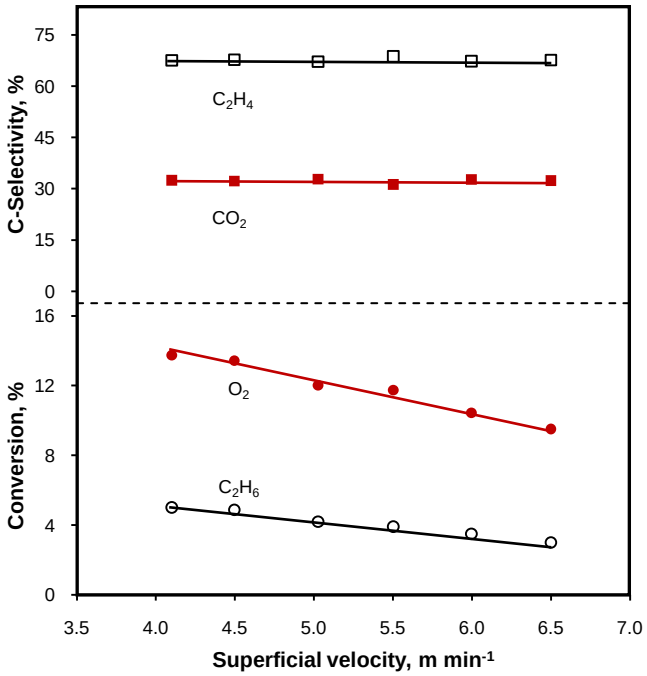

Fig. 6.7 Effects of gas superficial velocity (at reaction temperature) on the reactant conversion and product selectivity for the reaction of ethane and O_2 in the fluidised bed nanoparticle reactor at 280 °C.

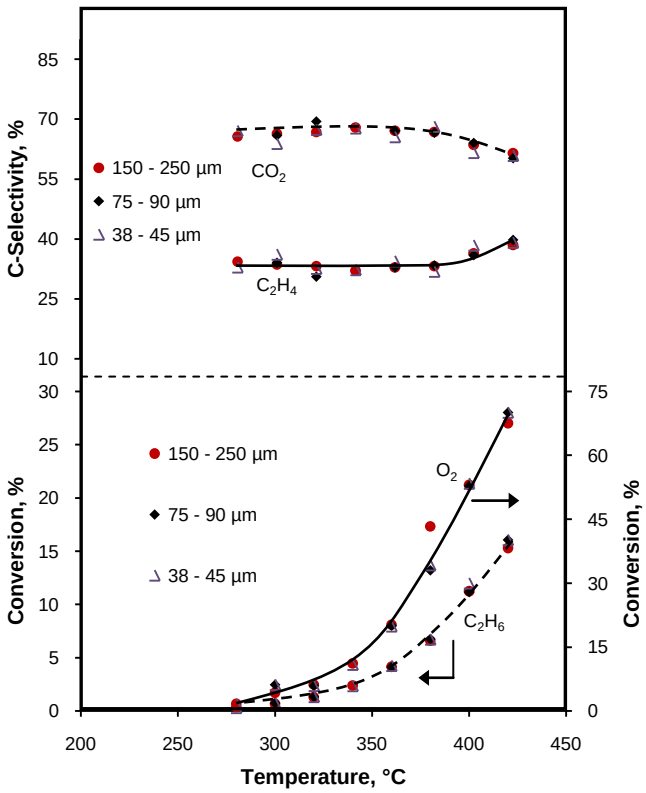

Fig. 6.8 Effects of support particle size and temperature on the catalytic ethane-O_2 reaction in a fluidised bed of NiO/SiO_2 catalysts.

When NiO/SiO_2 was used as a catalyst, the rigid porous structure of silica became a major barrier for the desorbed C_2H_5 radicals to diffuse into the bulk gas phase. The desorption/ diffusion of radicals have different scales from that of molecules [4-10]. The resistance of radical diffusion inside the pores can still be significant even under the conditions where the resistance for molecular diffusion is negligible [4-10]. The failure to immediately diffuse into the bulk gas phase created a chance for the C_2H_5 radicals to be re-adsorbed onto the catalyst surface to take part in the surface reactions (6.2 – 6.8). The re-adsorption of desorbed radicals together with the ability of catalyst surface to quench gas-phase radicals [5, 10, 38] would diminish the importance of localised "gas-phase" reactions inside the pores. Product selectivity would then show a different trend to the reaction in the nanoparticle fluidised-bed system.

With the overall reaction is dominated by surface reactions (in NiO/SiO_2 catalytic system), ethane activation via reaction (6.1) is rate-limiting. The increased rate of reaction (6.1) with increasing temperature would also mean the increased number C_2H_5 radicals on the surface. Initially, this increase would not affect the route of the subsequent reactions, i.e. reaction (6.2) versus reaction (6.3) or reaction (6.4) versus reaction (6.5), thus allowing product selectivity to remain constant when the temperature was increased up to 380 °C. However, it is suspected that further increase in temperature beyond 380 °C, which also means further increase in the supply of C_2H_5 (s), would start to reduce the relative proportion of O (s) to C_2H_5 (s) significantly. This would allow reaction (6.2) to take place more easily than reaction (6.3) to cause a slight increase in C_2H_4 selectivity in our study (Fig. 6.6).

6.3.3 Effects of oxygen partial pressure on the catalytic oxidation of ethane

The effects of oxygen partial pressure on the catalytic oxidation of ethane at 280 °C are shown in Figs. 6.9 and 6.10. In this series of experiments, C_2H_6 partial pressure was kept constant at 10.13 kPa. The O_2 partial pressure was varied while keeping the total gas flow rate constant by adjusting the amount of argon in the feed.

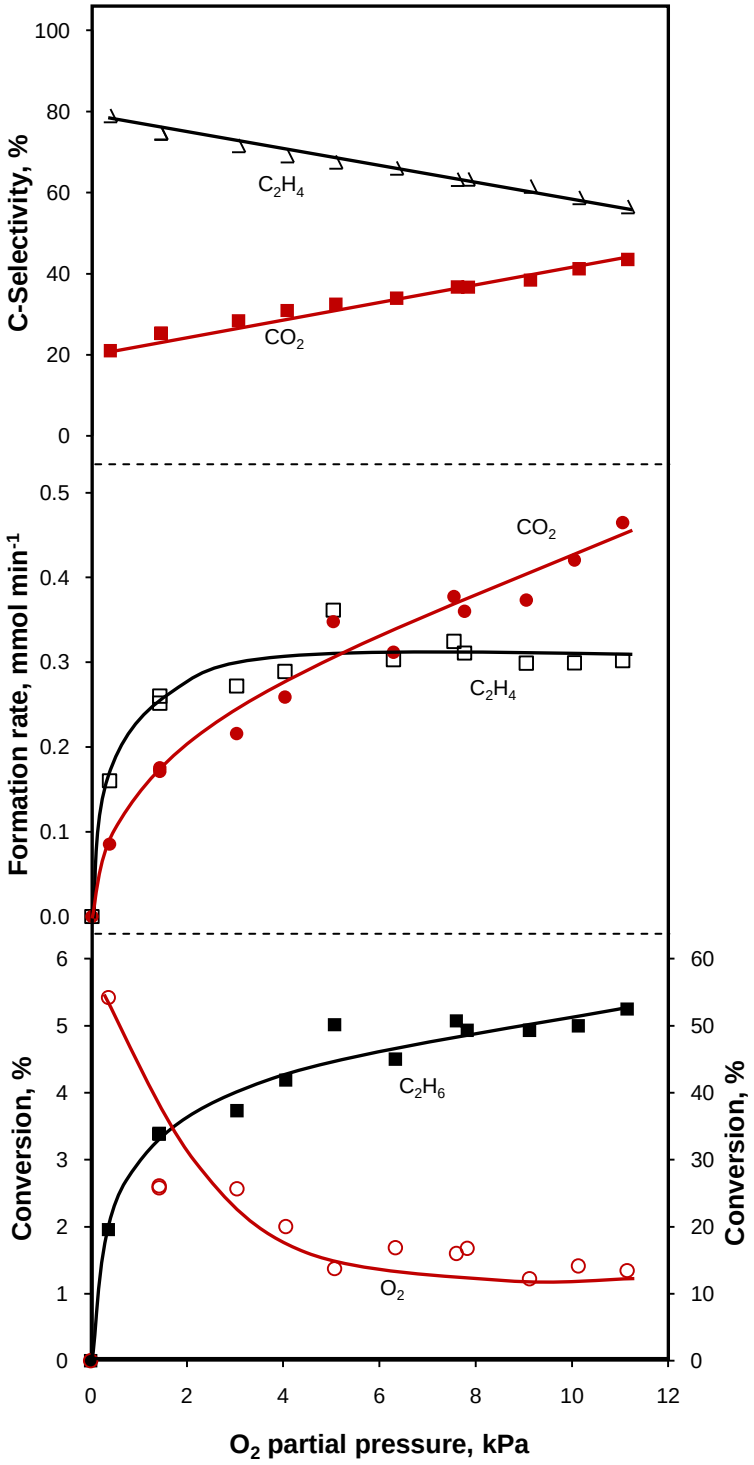

Fig. 6.9 Effects of O_2 partial pressure on the catalytic oxidation of ethane with fluidised NiO nanoparticles at 280 °C. In all experiments, C_2H_6 partial pressure = 10.13 kPa; catalyst amount = 5.5 g; superficial velocity = 4.1 m min^{-1}.

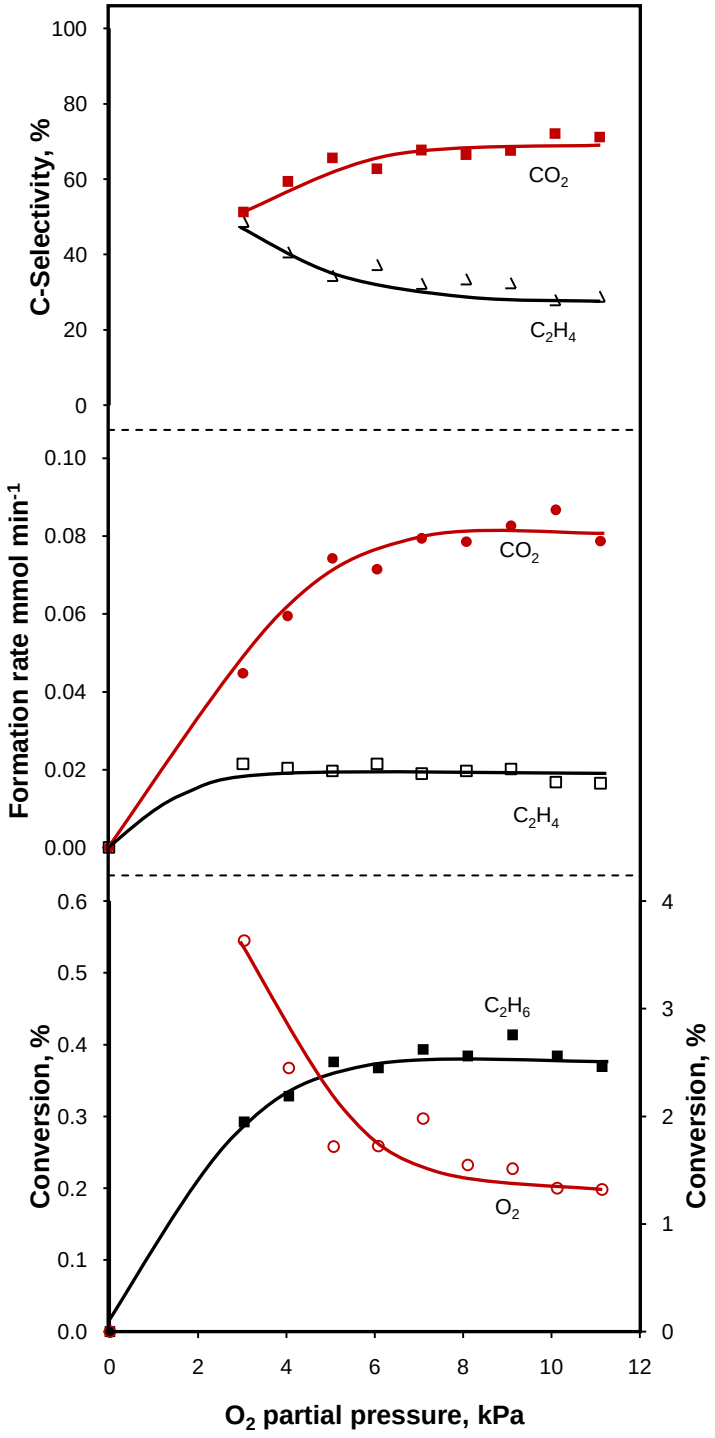

Fig. 6.10 Effects of O_2 partial pressure on the catalytic oxidation of ethane with SiO_2-supported NiO at 280 °C. In all experiments, C_2H_6 partial pressure = 10.13 kPa; catalyst amount = 9.2 g; superficial velocity = 6.2 m min^{-1}.

As one can see in Fig. 6.9, the consumption rates of C_2H_6 and O_2 in the fluidised bed nanoparticle reactor appears to be continuously dependent on the O_2 partial pressure, showing a typical behaviour of the gas-phase reactions rather than the surface reactions (see details below). The initial increase in oxygen supply (from 0 to about 2 kPa) caused a drastic increase in C_2H_6 conversion and product formation rates, reflecting the critical importance of gaseous O_2 in the reaction system. Interestingly, further increases in the O_2 partial pressure (within the range of our study) did not bring much change in the C_2H_4 formation rate but continuously increased the conversion of ethane and the formation rate of CO_2. A linear increase of CO_2 selectivity with respect to O_2 partial pressure and C_2H_6 conversion is so apparent for this catalytic system (Fig. 6.9).

With C_2H_6 partial pressure remained constant at a constant temperature, the rate of C_2H_5 formation on the surface (6.1) and its desorption (6.10) would be almost constant. However, with the lack of mass transfer resistance in the nanoparticle system, the desorbed C_2H_5 radicals could easily participate in the reactions inside the bulk gas phase. In this case, increasing O_2 partial pressure would promote reaction (6.11) and thus encourage the formation of the more reactive radical, OH, in the gas phase via reactions (6.12) to (6.14). The increased concentration of OH in the gas phase would then promote the conversion of ethane (6.15). The ultimate effects of the increase in O_2 partial pressure [promoting reaction (6.11) and (6.15)] would be the promotion of CO_2 formation more than that of C_2H_4 by increasing the ratio of $k_{6.16}[C_2H_4]/k_{6.15}[C_2H_6]$. The consideration of gas-phase reactions involving desorbed radicals, hence, explains the continuous increase of CO_2 selectivity and C_2H_6 conversion with the increase in O_2 partial pressure during the reaction of ethane-O_2 mixture in the nanoparticle fluidised-bed reactor (Fig. 6.9).

With NiO/SiO_2 as the catalyst (see Fig. 6.10), we observed that the C_2H_6 conversion and the CO_2 formation rate and selectivity increased when the O_2 partial pressure was increased up to 5 kPa. Further increase in the O_2 partial pressure, however, would only bring a constant reaction rate and selectivity, thus, suggesting that the reaction of ethane-O_2 mixture in the NiO/SiO_2 catalytic system shows the characteristics of the Langmuir-Hinshelwood surface-reaction-limited kinetics [39].

Clearly, the mass transfer resistance inside the silica pores was so strong not to allow the desorbed C_2H_5 radicals to diffuse into the bulk gas phase. The desorbed C_2H_5 radicals could easily be re-adsorbed onto the catalyst surface inside the pores.

When surface reactions are dominant, the increased population of surface oxygen with the increase in O_2 partial pressure could initially promote reaction (6.3) more than reaction (6.2) to results in the increased formation of CO_2 via reaction (6.4). Here, O (s) can also be of the intermediate oxygen species (6.9). As the catalyst surface coverage plateaus, further increase in the O_2 partial pressure would not bring any effect to the reactions on the catalyst surface, resulting in the constant product formation rates and selectivities (Fig. 6.10). The different effects of O_2 partial pressure on the fluidised nano NiO and the NiO/SiO_2 catalytic ethane-O_2 systems, therefore, further strengthen the theory regarding the presence and absence of mass transfer of the desorbed radicals presented earlier.

6.3.4 Effects of ethane partial pressure on the catalytic oxidation of ethane

The effects of ethane partial pressure on the catalytic oxidative reaction of ethane at a constant temperature (280 °C) and a constant O_2 partial pressure (5.07 kPa) are shown in Figs. 6.11 and 6.12.

For the nanoparticle system, the formation rate of C_2H_4 and CO_2 are shown (Fig. 6.11) to increase steadily with the increase in C_2H_6 partial pressure. The product selectivities, however, remain constant within the range of C_2H_6 partial pressure studied. The increase in C_2H_6 partial pressure would increase the rate of ethane activation by reaction (6.1). This in turn increases the concentration of C_2H_5 radicals in the gas phase to result in the increased consumption of oxygen in the gas phase via reaction (6.11). Increasing partial pressure of C_2H_6, therefore, is being well compensated by the increased formation of C_2H_4. This allows the ratio of $k_{6.16}[C_2H_4]/k_{6.15}[C_2H_6]$ (see the importance of this ratio in Section 6.3.2) to remain unchanged to result in the constant product selectivities with the change in C_2H_6 partial pressure.

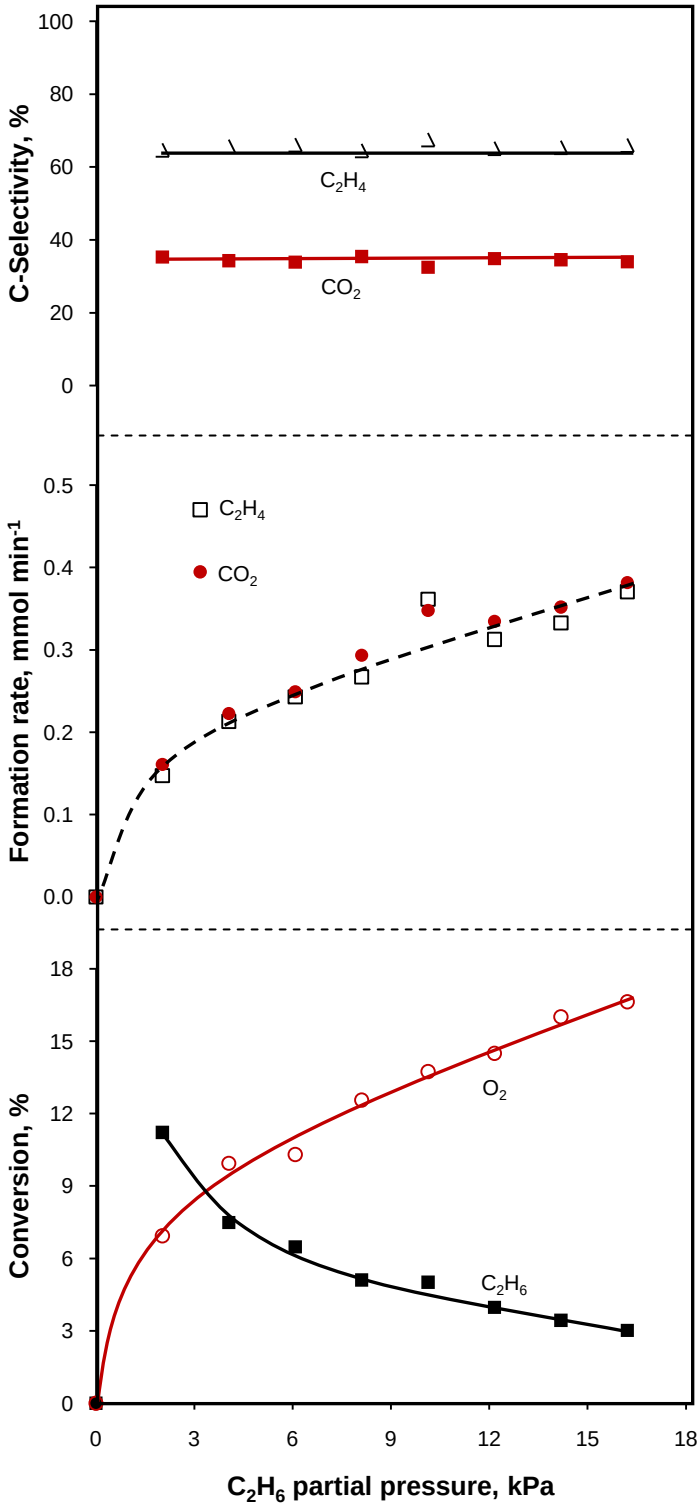

Fig. 6.11 Effects of C_2H_6 partial pressure on the catalytic ethane-O_2 reaction with fluidised NiO nanoparticles at 280 °C. In all experiments, C_2H_6 partial pressure = 5.07 kPa; catalyst amount = 5.5 g; superficial velocity = 4.1 m min^{-1}.

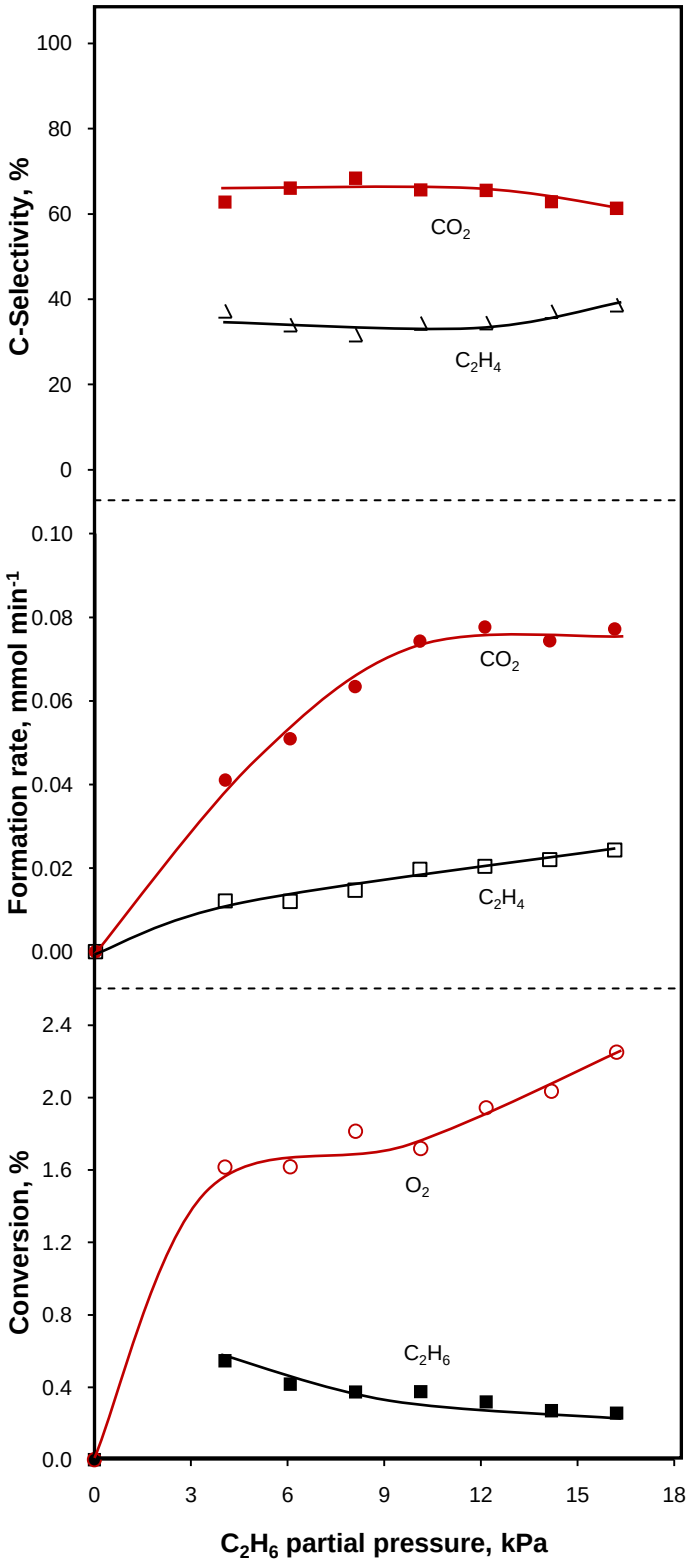

Fig. 6.12 Effects of C_2H_6 partial pressure on the catalytic ethane-O_2 reaction with SiO_2-supported NiO at 280 °C. In all experiments, C_2H_6 partial pressure = 5.07 kPa; catalyst amount = 9.2 g; superficial velocity = 6.2 m min^{-1}.

As for the porous-catalyst catalytic system (Fig. 6.12), the initial increases in C_2H_6 partial pressure up to about 10 kPa, have increased the rate of reaction (6.1). The formation rates of both C_2H_4 and CO_2 increased steadily within this range. Further increases in the C_2H_6 partial pressure, however, have caused the CO_2 selectivity to decline. It is believed that, as the reaction in the NiO/SiO_2 catalytic system predominantly takes place on the catalyst surface within the pores, the increased concentration of C_2H_5 (s) with the increase in C_2H_6 partial pressure caused an increase in the ratio of C_2H_5 (s) to O (s). This in turn would increase the chance of reaction (6.2) to take place more than reaction (6.3) to result in the slight increase in the selectivity of C_2H_4.

6.4 Conclusions

The nano-sized NiO particles and the traditional porous supported NiO/SiO_2 catalyst have been fluidised inside a quartz reactor to catalyse the reactions between ethane and oxygen. While the reactions in the fluidised bed of nanoparticles show behaviour similar to the gas phase reactions, the reactions of ethane-O_2 mixture in the porous-catalyst catalytic system, on the contrary, show the characteristics of a reaction system rate-limited by the surface reactions. Our experimental data can be explained by considering that the surface ethyl radicals formed by the interactions between ethane and NiO particles can desorb into the gas phase. When the fluidised NiO nanoparticles were employed as the catalyst, the lack of mass transfer barrier for radicals allowed the desorbed ethyl radicals to diffuse into the bulk gas stream to take place in the homogeneous radical reactions. However, when a porous-type NiO/SiO_2 was used as the catalyst, the diffusion of surface-generated ethyl radicals out of the catalyst pores was prohibited by the significant mass transfer resistance imposed by the rigid pore structure of silica. The desorbed radicals inside the silica pores can easily be re-adsorbed onto the catalyst to undergo reactions on the catalyst surface.

6.5 References

[1] D.J. Driscoll, J.H. Lunsford, Gas-phase radical formation during the reactions of methane, ethane, ethylene, and propylene over selected oxide catalysts, J. Phys. Chem. 89 (1985) 4415-4418.

[2] J.H. Lunsford, The role of surface-generated gas-phase radicals in catalysis, Langmuir 5 (1989) 12-16.

[3] K.T. Nguyen, H.H. Kung, Generation of gaseous radicals by a V-Mg-O catalyst during oxidative dehydrogenation of propane, J. Catal. 122 (1990) 415-428.

[4] E.B.H. Quah, C.-Z. Li, Effects of radical desorption on catalyst activity and coke formation during the catalytic pyrolysis and oxidation of light alkanes, Appl. Catal. A 250 (2003) 83-94.

[5] E.B.H. Quah, C.-Z. Li, Roles of desorbed radicals and reaction products during the oxidation of methane using a nickel mesh catalyst, Appl. Catal. A 258 (2004) 63-71.

[6] E.B.H. Quah, C.-Z. Li, Pyrolysis of liquefied petroleum gas assisted by radicals desorbed from mesh catalyst surface, Int. J. Chem. Kinet. 35 (2003) 637-646.

[7] E.B.H. Quah, J.F. Mathews, C.-Z. Li, Interinfluence between reactions on the catalyst surface and reactions in the gas phase during the catalytic oxidation of methane with air, J. Catal. 197 (2001) 315-323.

[8] W.J. Lee, C.-Z. Li, Coke formation and reaction pathways of catalyst-surface-generated radicals during the pyrolysis of ethane using Ni mesh catalyst, Appl. Catal. A 316 (2007) 90-99.

[9] W.J. Lee, C.-Z. Li, Opposite effects of gas flow rate on the rate of formation of carbon during the pyrolysis of ethane and acetylene on a nickel mesh catalyst, Carbon 46 (2008) 1208-1217.

[10] Chapter 3 of this thesis.

[11] W. Yao, G. Gu, W. Fei, W. Jun, Fluidization and agglomerate structure of SiO_2 nanoparticles, Powder Technol. 124 (2002) 152-159.

[12] J. Jung, D. Gidaspow, Fluidization of Nano-size Particles, J. Nanopart. Res. 4 (2002) 483-497.

[13] C. Zhu, Q. Yu, R.N. Dave, R. Pfeffer, Gas fluidization characteristics of nanoparticle agglomerates, AlChE J. 51 (2005) 426-439.

[14] L.F. Hakim, J.L. Portman, M.D. Casper, A.W. Weimer, Aggregation behavior of nanoparticles in fluidized beds, Powder Technol. 160 (2005) 149-160.

[15] J.R. Wank, S.M. George, A.W. Weimer, Nanocoating individual cohesive boron nitride particles in a fluidized bed by ALD, Powder Technol. 142 (2004) 59-69.

[16] L. Hakim, J. Blackson, S. George, A. Weimer, Nanocoating individual silica nanoparticles by atomic layer deposition in a fluidized bed reactor, Chem. Vap. Deposition 11 (2005) 420-425.

[17] S.A.R. Mulla, O.V. Buyevskaya, M. Baerns, A comparative study on non-catalytic and catalytic oxidative dehydrogenation of ethane to ethylene, Appl. Catal. A 226 (2002) 73-78.

[18] A.S. Bodke, D.A. Olschki, L.D. Schmidt, E. Ranzi, High selectivities to ethylene by partial oxidation of ethane, Science 285 (1995) 712-715.

[19] Y. Schuurman, V. Ducarme, T. Chen, W. Li, C. Mirodatos, G.A. Martin, Low temperature oxidative dehydrogenation of ethane over catalysts based on group VIII metals, Appl. Catal. A 163 (1997) 227-235.

[20] V. Ducarme, H.M. Swaan, A. Thaib, G.A. Martin, Oxidative dehydrogenation of ethane at low temperature over nickel catalysts: influence of morphology and chemical state of the solid during reaction, Stud. Surf. Sci. Catal. 107 (1997) 361-366.

[21] T. Chen, W. Li, C. Yu, R. Jin, H. Xu, The importance of nonstoichiometric oxygen in NiO for the catalytic oxidative dehydrogenation of ethane, Stud. Surf. Sci. Catal. 130 (2000) 1847-1852.

[22] Y. Liu, P. Cong, R.D. Doolen, S. Guan, V. Markov, L. Woo, S. Zeyß, U. Dingerdissen, Discovery from combinatorial heterogeneous catalysis: a new class of catalyst for ethane oxidative dehydrogenation at low temperatures, Appl. Catal. A 254 (2003) 59-66.

[23] X. Zhang, Y. Gong, G. Yu, Y. Xie, Oxygen species on NiO/Al_2O_3 and their reactivities, J. Mol. Catal. A: Chem. 180 (2002) 293-298.

[24] E. Heracleous, A.A. Lemonidou, Ni-Nb-O mixed oxides as highly active and selective catalysts for ethene production via ethane oxidative dehydrogenation. Part I: Characterization and catalytic performance, J. Catal. 237 (2006) 162-174.

[25] E. Heracleous, A.A. Lemonidou, Ni-Nb-O mixed oxides as highly active and selective catalysts for ethene production via ethane oxidative dehydrogenation. Part II: Mechanistic aspects and kinetic modeling, J. Catal. 237 (2006) 175-189.

[26] G. Grubert, E. Kondratenko, S. Kolf, M. Baerns, P. van Geem, R. Parton, Fundamental insights into the oxidative dehydrogenation of ethane to ethylene over catalytic materials discovered by an evolutionary approach, Catal. Today 81 (2003) 337-345.

[27] T.V.M. Rao, G. Deo, Ethane and propane oxidation over supported V_2O_5/TiO_2 catalysts: analysis of kinetic parameters, Ind. Eng. Chem. Res. 46 (2006) 70-79.

[28] X. Lin, C.A. Hoel, W.M.H. Sachtler, K.R. Poeppelmeier, E. Weitz, Oxidative dehydrogenation (ODH) of ethane with O_2 as oxidant on selected transition metal-loaded zeolites, J. Catal. 265 (2009) 54-62.

[29] H.H. Kung, Oxidative dehydrogenation of light (C_2 to C_4) alkanes, Adv. Catal. 40 (1994) 1-38.

[30] E. Morales, J.H. Lunsford, Oxidative dehydrogenation of ethane over a lithium-promoted magnesium-oxide catalyst, J. Catal. 118 (1989) 255-265.

[31] D.M. Kulich, J.E. Taylor, Mathematical simulation of oxygen-ethane reaction, Int. J. Chem. Kinet. 7 (1975) 895-905.

[32] J.E. Taylor, D.M. Kulich, Homogeneous gas-phase pyrolyses with a wall-less reactor. III. The oxygen-ethane reaction. A double reversal in oxygen and surface effects, Int. J. Chem. Kinet. 5 (1973) 455-468.

[33] P. Dagaut, M. Cathonnet, J.C. Boettner, Kinetics of ethane oxidation, Int. J. Chem. Kinet. 23 (1991) 437-455.

[34] Y. Hidaka, K. Sato, H. Hoshikawa, T. Nishimori, R. Takahashi, H. Tanaka, K. Inami, N. Ito, Shock-tube and modeling study of ethane pyrolysis and oxidation, Combust. Flame 120 (2000) 245-264.

[35] C.K. Westbrook, F.L. Dryer, Chemical kinetic modeling of hydrocarbon combustion, Prog. Energy Combust. Sci. 10 (1984) 1-57.

[36] Chapter 4 of this thesis.

[37] Chapter 5 of this thesis.

[38] Y.S. Su, J.Y. Ying, W.H. Green, Upper bound on the yield for oxidative coupling of methane, J. Catal. 218 (2003) 321-333.

[39] H.S. Fogler, Elements of chemical reaction engineering, 4th ed., Prentice Hall PTR, Upper Saddle River, NJ, 2006.

CHAPTER 7

Conclusions and recommendations

7.1 Conclusions

This study was carried out to gain fundamental insights into the significance of surface-generated radicals in the gas-solid catalytic reactions (with particular attention to the catalytic partial oxidation of light hydrocarbons). The key findings and the main conclusions drawn from this study are summarised and outlined below:

- The understanding of the fates of surface-generated radicals inside the traditional porous catalysts is largely hindered by the so called " irreducible mass transfer limitations". To avoid this complexity, in Chapter 3, a non-porous nickel mesh catalyst was used to study the catalytic ethane oxidation at 625 °C. From this study (Chapter 3), it is concluded that the surface-catalysed reactions and the gas-phase reactions may inter-influence each other. This inter-influence is resulted by the dual roles of catalyst surface as a radical supplier and a radical quencher. The radicals formed on the catalyst surface can desorb into the bulk gas phase if the mass transfer resistance caused by the gas film is minimised. The preferential desorption of OH radicals in this study (Chapter 3) has accelerated reactions in the gas phase, resulting in the preferential increases in the formation of terminal products (CO_2 and H_2) relative to the formation of other products. The study in Chapter 3 also indirectly shows that, inside the pores of a traditional supported catalyst, surface-generated radicals can migrate from catalyst surface to the gas phase and then back to catalyst surface within the same pores. Overall, this study (Chapter 3) highlights the importance of considering various radical fates (e.g. desorption and re-adsorption) in the catalyst pores in evaluating the intrinsic reaction mechanisms for the hydrocarbon-O_2 catalytic systems.

- In Chapter 4, a kinetic investigation on the reduction of nano-sized nickel oxide particles with hydrogen was carried out. The results of this study (Chapter 4) show that the reduction behaviour of NiO with crystallite size > about 20 nm is quite different from that of much smaller crystallite size particles. While the reduction of nano NiO particles of 3.3 nm average

crystallite size does not show the appearance of kinetic compensation effect, the reduction of NiO with > 20 nm crystallite size shows strong kinetic compensation effect with two different isokinetic temperatures at the low and high NiO conversion levels. For a small NiO crystal/particle, the dissociation of hydrogen is the key rate-determining step, and this remains unchanged almost throughout the reduction – the distance of H radical migration is too small to cause a significant effect on the kinetics of reduction. However, when NiO crystallite size is > 20 nm, the H radical migration/diffusion both on the surface and inside the NiO crystallite/particle become very important. With significant portion of atoms in the interior (for bigger NiO crystallites), the movement and re-arrangement of atoms in the interior can influence the activation energy of reduction very significantly. This study (chapter 4), thus, provides valuable insights into the effect of crystallite size (within nanometer scale) on the activities and kinetic influence of surface-generated radicals.

- Extending the study in Chapter 4, the study in Chapter 5 investigated the reduction of supported and unsupported NiO nanoparticles with different reducing gases (hydrogen, methane and ethane). It was found that the reduction kinetics cannot simply be explained by considering the reaction and mass transfer of molecular species. The fates and activities of surface-generated radicals can have significant influences in determining the rates of nickel oxide reduction and have to be taken into account in the kinetic considerations. When the resistance for the surface-generated radicals to desorb is negligible, the radicals can have a chance to escape away from the particle surface to result in the decrease of NiO reduction rate. The ease with which a radical desorb and migrate depend strongly on the strength of the bonding between the radicals and the Ni atoms.

- The use of fluidised-bed nanoparticles as catalysts for the conversion of light hydrocarbons, which has never been reported anywhere before, was explored in Chapter 6. In the study (Chapter 6), the unsupported NiO nanoparticles have been fluidised in a quartz-walled reactor to catalyse the reactions between ethane and oxygen. Comparisons between the fluidised nanoparticle

catalytic system and the traditional porous catalyst system were made. For this purpose, the NiO/SiO_2 catalysts have been employed to catalyse the same reaction inside the same reactor. The data show that, while the catalytic reaction between ethane and oxygen inside the fluidised-bed reactor follows similar behaviour to the gas-phase reaction, the same reaction, on the contrary, shows the characteristics of a reaction rate-limited by the surface reactions when the NiO/SiO_2 was used as a catalyst. This study (Chapter 6) further strengthens the view that the radicals formed on the catalyst surface can easily desorb to participate in the gas-phase reactions if the resistance for their desorption is negligible.

This thesis, therefore, provides enhanced understanding of the importance of surface-generated radicals in the gas-solid catalytic reactions. In short, this study shows that the surface-generated radicals can participate in the further reactions on the surface, migrate on the surface and into the catalyst matrix, and desorb to react in the gas phase. The fates of surface-generated radicals and the radical mass transfer which is significantly different from that for molecular species are very important aspects to be considered in evaluating and elucidating the intrinsic kinetics and mechanism of a gas-solid catalytic reaction.

7.2 Recommendations

- Chapter 3 showed the effects of radical desorption from the nickel mesh surface in the catalytic partial oxidation of ethane. It is very interesting if the study on the effect of flow rate on the catalytic reactions with Ni mesh catalyst is coupled with the sophisticated in-situ surface characterisation technique e.g. the X-ray photoelectron spectroscopy (XPS) and/or radical detection technique e.g. the laser-induced fluorescence spectroscopy.

- The effect of hydrodynamics on the radical desorption can be further studied. This can be done, for example, by using mesh catalyst of different wire diameters.

- The use of fluidised NiO nanoparticles as catalyst, although proved to be beneficial in understanding the effect of radical desorption, still have some limitations. The NiO nanoparticles can easily become defluidsed at high temperature due to the sintering effect when the NiO particles are partially reduced and when the oxygen is completely consumed. It is recommended that non-reducible metal oxide nanoparticles are used in the future study to avoid this problem.

- As have been explained earlier in this thesis, this is the first time that a fluidised-bed nanoparticle reactor is used for the conversion of light hydrocarbon. Many studies on the reactor system itself can be further studied. For example, it would be of interest to apply the external force fields such as sound waves and magnetic field in improving the fluidisation quality of nanoparticles and to see their effects on the catalytic reactions.

- Detailed chemical kinetic modelling would be a powerful accompaniment to the results of this study. As such, it is highly recommended that a kinetic computer model which couple the heterogeneous and the homogeneous reaction schemes to be developed based on the results presented in this thesis.

APPENDIX I

Publications and presentations

Journals

[1] **S.S.A. Syed-Hassan**, W.J. Lee, C.-Z. Li, Positive and negative catalytic effects of a nickel mesh catalyst for the partial oxidation of ethane, **Chemical Engineering Journal**, 2009, 147, 307-315.

[2] **S.S.A. Syed-Hassan**, C.-Z. Li, NiO reduction with hydrogen and light hydrocarbons: Contrast between SiO_2-supported and unsupported NiO nanoparticles, **Applied Catalysis A: General**, 2011, 398, 187-194.

[3] **S.S.A. Syed-Hassan**, C.-Z. Li, Effects of crystallite size on the kinetics and mechanism of NiO reduction with H_2, **International Journal of Chemical Kinetics** (submitted).

[4] **S.S.A. Syed-Hassan**, C.-Z. Li, Catalytic oxidation of ethane with oxygen using fluidised nanoparticle NiO catalyst, **Applied Catalysis A: General**, (submitted).

[5] W.J. Lee, **S.S.A. Syed-Hassan**, C.-Z. Li, Formation of carbon on non-porous Ni mesh during the catalytic pyrolysis of acetylene (in preparation).

Conferences

[1] **S.S.A. Syed-Hassan**, C.-Z. Li, A comparative kinetic study on the reduction of unsupported nano NiO particles and silica-supported NiO, **CHEMECA 2010**, Adelaide, Australia, September 26-29, 2010 (Oral presentation by C.-Z. Li; full refereed paper).

[2] **S.S.A. Syed-Hassan**, W.J. Lee, C.-Z. Li, How the fate of surface-generated radicals influences the rate of catalysed light hydrocarbon reactions and the formation of carbon on the catalyst surface, **5th International Symposium on**

Novel Carbon Resource Sciences, Perth, Australia, April 21-23, 2010 (Oral presentation by S.S.A. Syed-Hassan).

[3] **S.S.A. Syed-Hassan**, C.-Z. Li, Inter-influence of heterogeneous and homogeneous radical reactions during the catalytic reactions of ethane, **CHEMECA 2009**, Perth, Australia, September 27-30, 2009 (Oral presentation by S.S.A. Syed-Hassan; full refereed paper).

[4] **S.S.A. Syed-Hassan**, C.-Z. Li, Roles of catalyst surface in promoting and inhibiting the gas-phase reactions of ethane-O2 mixture, **13th Asian Chemical Congress**, Shanghai, China, September 13-16, 2009 (Oral presentation by S.S.A. Syed-Hassan).

APPENDIX II

Permission of reproduction from the copyright owner

PEARSON

Legal/Permissions
One Lake Street
Upper Saddle River, NJ 07458
Fax: 201-236-3290
Phone: 201-236-3564
Cheryl.Freeman@Pearson.com

Dec 6, 2010 PE Ref # 156599

SYED SHATIR ASGHRAR SYED HASSAN
Curtin Centre for Advanced Energy Science and Engineering
Curtin University of Technology
GPO Box U 1987
Perth WA, 6845 AUSTRALIA

Dear Mr. Syed Hassan:

You have our permission to include content from our text, ***ELEMENTS OF CHEMICAL REACTION ENGINEERING, 4th Ed. by FOGLER, H.,*** in your Ph.D. thesis for your studies
at Curtin University of Technology.

Content to be included is:
Page 656: Figure 10-6 Steps in a heterogeneous catalytic reaction

Dissertation available on one (1) hard-copy in the Curtin Library and in digital form on the Internet
via the Australasian Digital Thesis Program.

Please credit our material as follows:
FOGLER, H., ELEMENTS OF CHEMICAL REACTION ENGINEERING, 4th Ed., © 2006. Reprinted by permission of Pearson Education, Inc., Upper Saddle River, NJ

Sincerely,

Cheryl Freeman, Permissions Administrator